Manfred Gruber

# Simulation of the charge carrier transport in organic semiconductor devices

DOCTORAL THESIS

For obtaining the academic degree of
Doktor der technischen Wissenschaften

Doctoral Programme of Technical Sciences
Technical Physics


Graz University of Technology

Supervisor:

Ao.Univ.-Prof. DI Dr. Ferdinand Schürrer

Institute of Theoretical and Computational Physics

Graz, July 2012

Deutsche Fassung:
Beschluss der Curricula-Kommission für Bachelor-, Master- und Diplomstudien vom 10.11.2008
Genehmigung des Senates am 1.12.2008

## EIDESSTATTLICHE ERKLÄRUNG

Ich erkläre an Eides statt, dass ich die vorliegende Arbeit selbstständig verfasst, andere als die angegebenen Quellen/Hilfsmittel nicht benutzt, und die den benutzten Quellen wörtlich und inhaltlich entnommene Stellen als solche kenntlich gemacht habe.

Graz, am …….  ……..
(Unterschrift)

Englische Fassung:

## STATUTORY DECLARATION

I declare that I have authored this thesis independently, that I have not used other than the declared sources / resources, and that I have explicitly marked all material which has been quoted either literally or by content from the used sources.

…….  ……..
date  (signature)

*To Mom and Dad.*

*Holzhacken ist deswegen so beliebt, weil man bei dieser Tätigkeit den Erfolg sofort sieht.*

Albert Einstein

# Acknowledgments

I would like to express profound gratitude to my advisors Ao.Univ.-Prof.Dr. Ferdinand Schürrer and Dipl.-Phys. Dr. Karin Zojer for their invaluable support, encouragement, supervision and useful suggestions throughout this thesis. I attribute the level of my academic degree to their encouragement and effort and without them this thesis, too, would not have been completed or written. One simply could not wish for better or friendlier supervisors. The work concerning the simulations of organic field effect transistors has been supported by the Austrian Nanoinitiative (FFG) through the NILsimtos project as part of the NILaustria cluster. The simulations of the organic/inorganic hybrid solar cells has been done in collaboration with the "Christian Doppler Labor für Nanokomposit Solarzellen" and, therefore, I want to thank all members of the group, especially the leader Dipl.-Ing. Dr. Univ.-Doz. Gregor Trimmel, Dr. Thomas Rath and DI Mario Arar. Moreover, I want to thank my chief experimenter Dr. Simon Ausserlechner at the Solid State Physics Institute for supplying me with experimental data concerning organic field-effect transistors, for fruitful discussions and the nice time during the conferences.
I would also like to express thanks to my parents for their support during my study. However, a man is only as successful as the girl behind him and, therefore, I want to thank Julia for supporting me mentally, the nice time and for messing about with a crazy physicist like me. Finally, I want to express profound gratitude to all people who accompanied me during my study, especially the "4M$^s$ featuring Fredl the Φch" for being a member of them.

# Abstract

In this thesis, a drift-diffusion model is developed to simulate the charge carrier transport in organic/inorganic hybrid solar cells and organic thin film transistors. Non-ohmic boundary conditions at the electrodes, i.e., thermionic emission, tunneling and interface recombination currents are taken into account. The resulting system of equations, including the charge carrier transport and the Poisson equation, is solved iteratively using an implicit time integration.

As a result of the simulation of hybrid solar cells, it is possible to identify the morphology and the energy alignment of the transport levels of the organic and inorganic phase as efficiency limiting factors.

Concerning the simulations of organic field-effect transistors, the influence of the charge carrier injection barrier, the temperature and channel-length on the contact resistance and, therefore, on the device characteristics, is investigated. Furthermore, the influence of space charge layers and dipoles is studied. An excellent agreement between simulation and experiment is found.

# Kurzfassung

Ziel dieser Arbeit ist es, ein Modell zur Simulation des Ladungsträgertransportes in organisch/anorganischen Hybridsolarzellen und organischen Dünnfilmtranistoren zu entwickeln. Es werden nicht-ohmsche Randbedingungen an den Kontakten, zur Implementierung von thermionischer Emissions-, Tunnel- und Interfacerekombinationsströmen als Injektionsmechanismen eingeführt. Das resultierende System bestehend aus der Ladungsträgertransport- und Poissongleichung, wird iterativ mithilfe eines impliziten Zeitschrittverfahrens gelöst.

Die Simulation von Hybridsolarzellen ermöglicht, die Morphologie und die energetische Lage der Transportniveaus der organischen und anorganischen Phasen als effizienzlimitierende Faktoren zu bestimmen.

Bei der Simulation von organischen Dünnfilmtransistoren wird die Abhängigkeit des Kontaktwiderstandes und somit der Kennlinien von der Injektionsbarriere, Temperatur und Kanallänge untersucht. Weiters wird der Einfluss von Raumladungen und Dipolen erforscht und mit experimentellen Ergebnissen verglichen. Dabei wird sehr gute Übereinstimmung erzielt.

# Contents

# Introduction

One of the greatest inventions at the beginning of the $20^{th}$ century were electronic devices based on semiconducting materials. Since that time, highly sophisticated building blocks devices and production techniques concerning applicability, performance and integration density have been developed [1]. Some important devices are field-effect transistor, bipolar transistors, diodes, photodiodes, light-emitting diodes and solar cells [2]. The biggest disadvantage of using conventional inorganic semiconductors like silicon or gallium arsenide is the high energy consumption during production and processing [3]. And in a time where natural resources like coal, oil and gas become rare and, therefore, expensive, there is a need for alternative, economical production and processing techniques. Furthermore, carbon dioxide emission induced global warming leads to further big problems to society [4].

On way out of this problem is the usage of organic semiconducting materials, which have the advantage of low processing temperatures and, therefore, low energy consumption, and the possibility of large area fabrication in a cheap roll-to-roll process on a flexible substrate. But, state of the art organic electronic devices have the disadvantages of having low efficiencies, bad reproducibilities and high chemical degradation rates. Latter can be avoided or at least delayed by encapsulation of the active parts. Today's only electronic devices with marketability are organic light emitting diodes which are used in modern displays. But these organic light emitting diodes have the disadvantage of requiring process steps that make them extremely expensive.

It is part of this work to investigate the efficiency and performance limiting factors in organic solar cells and organic thin film transistors (OTFTs).

Therefore, a model based on a drift-diffusion approach has been developed to describe the physically relevant properties.

The **first part** of this thesis deals with the simulation of organic/inorganic hybrid solar cells which has been performed in collaboration with the "Christian Doppler Laboratory of Nanocomposite Solar Cells". Here, a work which is published in Organic Electronics in 2010 [5] is presented. In general, nanocomposite hybrid solar cells are produced by spin-coating, spray casting or doctor knife blading of a precursor solution on a substrate. The substrate consists of glass which is sputtered with indium tin oxide, which is a transparent and conductive material and serves as anode. The precursor solution consists of the dissolved organic (polymer) and inorganic phases. After a thermal conversion step, the inorganic components form nanoparticles which tend to agglomerate. The last step is to evaporate the low-workfunction top electrode (cathode) which is mostly aluminum. This sophisticated, very simple, production processes can easily be translated into an industrial roll-to-roll process, leading to low cost solar cells. But, unfortunately, at the moment with a low efficiency. To improve the efficiency it is, therefore, crucial to understand what limits the performance.

Apart from chemical aspects like the choice and purity and absorption properties of the materials used, it is shown in the presented work that the efficiency is also strongly affected by the morphology and the alignment of the transport levels of the organic and inorganic phase.

The **second part** is dedicated to OTFTs. Basically, state of the art OTFTs cannot compete with their inorganic counterparts in terms of switching speed or integration density but, in future, they could play a major role in smart cheap applications like chemical sensors, radio-frequency identification-chips (RFID) or to switch organic light emitting diodes in a display. Latter has the big advantage that the same production processes, e.g., ink-jet printing or stamping, can be applied to the whole active part of a display, which would lead to an enormous cost reduction.

There exists a huge variety of different device layouts of organic field-effect transistors but, here, we will concentrate on the top-contact bottom-gate type. This work has been supported by the Austrian Nanoinitiative (FFG)

through the NILsimtos project as part of the NILaustria cluster. In the program, non-ohmic boundary conditions are included with thermionic emission, tunneling and interface recombination as charge carrier injection mechanisms. Here, the charge carrier injection barrier, which is the difference between the workfunction of the electrode and the corresponding transport-level, is the parameter which describes the material dependent contact behaviour.

In the first chapter of the second part, a work which is published in Organic Electronics in 2012 [6] is presented. This work deals with the influence of the charge carrier injection barrier, temperature and channel-length on the contact resistance and, therefore, on the device characteristics. In terms of switching speed, the charge carrier mobility has to be high and the channel-length small. It is shown that contact resistance becomes dominant for high charge carrier injection barriers and/or small channel-lengths. A dominant contact resistance manifests in a reduction of the effective source-drain and source-gate voltages which gives a lower limit for the operating voltages of the device. This is a disadvantage for commercial use where operating voltages are kept small to reduce size and power consumption. Therefore, the charge carrier injection barrier has to be kept small in order to obtain a good performance at small channel-lengths. This could be obtained for example by adjusting the electrode material to the corresponding transport-level.

The last chapter deals with the influence of a certain self-assembled monolayer (SAM), which acts as acid between the active (pentacene) and dielectric ($SiO_2$) material on the device characteristics [7]. In the experiment, it was observed that the SAM leads to a shift of the threshold-voltage of the device. In the simulation, a space charge and/or interface dipole layer was placed between the active layer and dielectric material and, additionally, charge carrier trapping and detrapping was also included to describe the formation of a hysteresis in the experiment.

As a simulation result, a space charge layer leads to a shift of the threshold-voltage which is directly proportional to the thickness of the dielectric layer, while a shift stemming from a dipole layer is independent of the thickness. To explain the formation of a space charge, it is assumed that the SAM transfers protons to the pentacene molecules which leads to free holes. The remaining

negative charges at the SAM are forming the space charge. This so-called surface proton transfer doping mechanism has also been studied by quantum chemical calculations.

Therefore, transfer-characteristics of OTFTs with SAMs have been measured and simulated for several thicknesses of the dielectric. The simulation and experiment leads to an excellent agreement when assuming both, a space charge and dipole layer.

Furthermore, it is shown that the shift of the threshold-voltage can be reversed if the device is exposed to ammonia. This effect could be used commercially to built-up an ammonia sensor.

# Part I

# Organic Solar Cells

# Chapter 1

# Impact of energy alignment and morphology on the efficiency in inorganic-organic hybrid solar cells

## 1.1 Preamble

The following work is published in Organic Electronics in 2010 [5] by M. Gruber, B. A. Stickler, G. Trimmel, F. Schürrer and K. Zojer.

In this work, we calculated the efficiencies according to the solar spectrum used (AM 1.5, 1000 $Wm^{-2}$). We realized after publishing that the solar spectrum used is wrongly labeled and in fact it was an AM 1.5 with 500 $Wm^{-2}$. Therefore, the calculated efficiencies have to be multiplied by a factor of two. In this chapter this mistake is corrected.

## 1.2 Abstract

Carrier transport in hybrid inorganic-organic solar cells has been studied by means of a two-dimensional drift-diffusion-based model including the gener-

ation and motion of excitons. The devices consist of a polymer serving as donor material and a semiconducting small-band gap inorganic component as acceptor material. For the first time it is taken into account that, in strong contrast to purely organic or inorganic cells, charge carriers can be generated directly at the heterojunction (due to dissociation of the donor excitons) *and* in the bulk of the acceptor material (due to band to band generation in the inorganic material). The efficiencies of devices were investigated dependent on (i) the donor-acceptor interface geometry, (ii) the transport level offsets at the heterojunction, and (iii) the energy barriers formed at the contacts. For each case, a detailed analysis of behavior is given. We demonstrate that, depending on the particular scenario, each of these three factors can be responsible for profoundly reduced efficiencies and pronounced s-shaped sections in the I-V curves. Moreover, we show that each of the investigated factors may give rise to equally serious efficiency losses. However, it is not possible to identify a dominant effect. Depending on the particular combination, the efficiency can vary by two orders of magnitudes. In order to avoid such losses, our theoretical assessment reveals that suitable material combinations are required to form (i) ohmic contacts, (ii) preclude formation of isolated islands or nanoparticles during growth, and (iii) possess a hole-blocking offset in the transport levels at the heterojunction.

## 1.3 Introduction

Inorganic-organic hybrid solar cells (hsc) represent one of the currently persued routes to produce low-cost solar cells. The introduction of an inorganic component rather than an organic material promises a good control over the morphology to arrive at an interdigited heterointerface, e.g., by incorporating nanowires of ZnO or $TiO_2$ [8, 9, 10, 11, 12, 13, 14, 15] as acceptor materials. To combine these advantages with the desire to efficiently harvest sun light, the absorption spectra of the organic and inorganic phase are required to cover the solar spectrum in a preferably complementary fashion. One promising route to achieve this is to employ an organic material that covers

the high-irradiance portion of the solar spectrum, i.e., visible light between $1.7-3.0\,eV$, and an inorganic component that absorbs in the long-wavelength tail well below $1.7\,eV$. Suitable inorganic semiconductors are, e.g., CdSe , CdTe, and $S_2$ [16, 17, 18, 19, 20, 21, 22, 23, 24, 25, 26]. In hsc containing these materials, the organic and inorganic phase contribute differently to charge carrier generation. Upon light absorption, excitons are formed in the organic phase and need to diffuse to the heterojunction interface within their lifetime in order to dissociate into free charges. In the inorganic semiconductor, carriers are generated directly via band-to-band absorption throughout the bulk. Therefore, the question arises to which extent these two strongly differing generation mechanisms influence the efficiency of such cells. In particular, the impact on efficiency-related factors such as morphology, contact materials, and transport level alignment requires detailed investigation.

Hybrid inorganic-organic heterojunctions can be prepared in several distinct types of morphologies: Besides bilayer structures, (i) nanoporous inorganic templates infiltrated with polymers and (ii) blends of organic polymers co-deposited with inorganic (isotropic) nanoparticles or nanorods have been prepared. A comprehensive overview can be found, *e.g.*, in Refs. [9, 13]. Morphologies in which the photoactive materials are segregated perpendicular to the electrodes are particularly sought after, since this vertical alignment reduces shortenings and recombination [12, 8]; such structures were achieved by co-deposition [18, 19, 20, 21, 22] or a template approach [8, 23, 24]. Compared to hybrid bilayer structures, blend devices usually exhibit relatively low open-circuit voltages and fill factors, *cf., e.g.*, Ref. [8].

Devices made of blends containing nanorods of high aspect ratios systematically outperform nanoparticle blends in terms of short circuit currents, open circuit voltages, and higher efficiencies [8, 21, 22]. The performance of excitonic solar cells consisting either of hybrid blends/template structures containing wide bandgap ors such as ZnO or $TiO_2$ [8] or pure organic blends (containing $C_{60}$-derivatives or small molecules) [26] is strongly dependent on the morphology. Previous studies related this effect to (i) an effective generation efficiency [27, 28], (ii) the apparent length of the interface available for exciton cleavage [8, 29, 30], (iii) the connectivity of transport paths [31],

and (iv) a change in the effective mobility [32]. Moreover, the occurrence of an s-shaped I-V curve [8, 9, 33, 34, 35, 36, 37, 38, 39] has been linked to the selectivity of the contact materials [33, 37, 38, 39, 36], and the alignment of transport levels [36].

The optimization of the morphologies in purely excitonic solar cell targets structure sizes being comparable to typical exciton diffusion lengths of ca. 15 nm [9]. The use of low-band gap inorganic materials can presumably obliterate the need for such small inorganic domain sizes, since generation due exciton migration is replaced by carrier generation in the bulk. Then, large inorganic domains offer the advantages of (i) providing efficient carrier generation due to bulk generation, (ii) a more efficient carrier abstraction at the contacts and, thus, less efficient recombination due to higher intrinsic mobilities, (iii) ensuring a better connectivity [17], and, (iv) presumably leading to a higher average carrier mobility due to a significantly reduced number of interparticle hops [17].

The main aim of this work is to theoretically investigate the impact of (i) cell morphology, (ii) transport level alignment, and (iii) choice of contacts on the carrier transport and, consequently, the efficiency of such hybrid inorganic-organic solar cells. Under consideration of the two charge generation mechanisms, the abovementioned effects were cast into a two-dimensional drift-diffusion model for both charge carrier and exciton transport. Based on this model, current-density voltage (I-V) curves of the entire device were simulated. The devices studied below consist of $CuInS_2$ as prototypical acceptor and P3EBT (poly[3-(ethyl-4-butanoate)thiophene-2,5-diyl]) as donor material (Fig. 1.1(d)). From a theoretical point of view, the combination of P3EBT with $CuInS_2$ is particularly intriguing due to a vanishing offset between the hole transport levels. Such a level alignment cannot be encountered in hsc based on wide-band gap semiconductors, such as ZnO and $TiO_2$. P3EBT can be of potential practical relevance due to an improved processability in comparison to the archetypical P3HT (poly(3-hexylthiophene)).

After introducing the details of the model, we will investigate the impact of the interface morphology on the carrier transport for selected heterojunction geometries. In a next step, the degeneracy in the hole transport levels

is lifted to point out the impact of transport level alignment. In a last series of simulations, the dependence of the I-V curves and the power conversion efficiency on the nature of the imposed contacts is studied for the chosen representative morphologies. Based on these simulations we will derive criteria for material properties according to which major efficiency losses can be avoided.

## 1.4 The Model

To get a deeper understanding of the device behavior due to variations (i) of the transport level offsets between the donor and acceptor material and (ii) their interface morphology, as well as the role of bulk vs. interface carrier generation, a two-dimensional drift-diffusion model for the device simulation is proposed. Such a two-dimensional model offers the possibility to regard actual morphologies such as isolated particles or ideal, i.e., interdigitated structures. Note that the feature size of the assumed interface geometries must be sufficiently large (*ca.* 15-20 nm) in order to define valid material parameters for the photoactive components as model input. Typical structure sizes in nanocomposite hybrid inorganic-organic solar cells are 5-20 nm for particle diameters, domain sizes, and nanorod diameters; nanorods of high aspect ratio are *ca.* 50-100 nm long [9, 8]. Thus, it is possible to construct artifical interface geometries that represent limiting cases of real morphologies and feature structure sizes known from actual heterojunctions.

In contrast to drift-diffusion models, microscopic simulations are able to safely tackle morphologies with typical length scales below 15nm. However, due to the extensive computational costs, most of the publications focus on interface generation and recombination processes [27, 40, 41, 42]. Apart from the pioneering works of Marsh et al. [27] and Meng et al. [41], subsequent carrier transport is not evaluated at the same level of complexity. Rather, it is either described by means of equivalent circuit models [42] or by one-dimensional drift-diffusion models [32]. The former is not able to reflect a departure of the I-V curve from the ideal diode characteristic and the latter

cannot take into account the actual morphology. Given that the hybrid inorganic-organic systems exhibit generation not only at the interface but also throughout the bulk, models as proposed in Refs. [27, 41] are neither computationally feasible nor are they suited to immediately interpret the results in terms of relevant macroscopic transport parameters.

*Charge transport equations:* In a drift-diffusion model, the motion of the charge carriers is caused by the electric field and carrier density gradients. The resulting current density is carried by electrons and holes in their respective transport levels. According to [43], the current density reads

$$\mathbf{J}(x,y) = \mathbf{J}_p(x,y) + \mathbf{J}_n(x,y) \tag{1.1}$$

with

$$\mathbf{J}_{n(p)}(x,y) = qn[/p](x,y)\mu_{n(p)}(x,y)\mathbf{E}_{n(p)}(x,y) \pm D_{n(p)}(x,y)q\nabla n[/p](x,y). \tag{1.2}$$

Here, $\mu_{n(p)}(x,y)$ denotes the electron (hole) mobility, $k_B$ the Boltzmann constant, $T$ the temperature, and $q$ the elementary charge ($q > 0$). Moreover, $n(x,y)$ and $p(x,y)$ are the density distributions and $\mathbf{E}_{n(p)}(x,y)$ the generalized electric fields (for definition see below) for electrons and holes, respectively. The electron (hole) diffusion constant is defined by the Einstein relation:

$$D_{n(p)} = \mu_{n(p)}(x,y)k_BT/q. \tag{1.3}$$

The current densities are coupled with the continuity equation for electrons and holes

$$\frac{\partial n[/p](x,y)}{\partial t} \mp \frac{1}{q}\nabla \mathbf{J}_{n(p)}(x,y) = G(x,y) - R(x,y) \tag{1.4}$$

where $G(x,y)$ and $R(x,y)$ are the charge carrier generation and recombination terms.

*Generalized potentials:* By defining a generalized potential $\widehat{\Psi}_{n(p)}$, the actual electrostatic potential $\Psi$ and the "driving forces" excerted on the carrier at the heterojunction can be cast into one quantity [44, 45]:

$$\widehat{\Psi}_{n(p)}(x,y) = \Psi(x,y) - \Theta_{n(p)}(x,y)/q. \tag{1.5}$$

Herein, the potential $\Psi(x,y)$, resulting from the Poisson equation

$$\nabla[\epsilon_0\epsilon_r(x,y)\nabla\Psi(x,y)] = q[n(x,y) - p(x,y)], \tag{1.6}$$

is caused by the charges in the active layer and the effective applied voltage $V$; $\epsilon_0$ is the dielectric constant of vacuum and $\epsilon_r(x,y)$ the relative dielectric constant. $V$ is the difference of the external applied voltage and the built-in voltage and by the boundary conditions at the non-conducting surfaces. The additional terms $\Theta_{n(p)}(x,y)$ in Eq. (1.5) are the band parameters that are associated to the spatial energetic alignment of the transport levels [44, 45]. In disordered materials, $\Theta_{n(p)}(x,y)$ is directly given by the relative spatial alignment of the transport levels [44]. For convinience, we set the band parameters to zero in the organic donor ($\Theta_{n(p)} = 0$) and to the transport level offsets in the inorganic acceptor ($\Theta_n = E_\mathrm{C} - \mathrm{LUMO}$; $\Theta_p = E_\mathrm{V} - \mathrm{HOMO}$). Thus, the generalized potential multiplied by the charge of the carrier yields the actual potential energy landscape in which the carrier traverses the device. Carrying out the spatial derivative of the generalized potential yields a generalized electric field that was formally introduced in Eq. (1.2):

$$\mathbf{E}_{n(p)}(x,y) = -\nabla\widehat{\Psi}_{n(p)}(x,y). \tag{1.7}$$

It consists of the true electric field across the device superimposed with an additional term occurring solely at the interface. For abrupt heterojunctions, this generalized electric field has no physical meaning due to the singularity at the interface. However, once cast in the final form, the transport equations Eqs. (1.2,1.4) contain the generalized potential rather than its spatial derivative [45]. The associated terms account for the "driving force acting"on the carrier at the interface [44]; they penalize uphill and encourage downhill motion by means of an exponential factor containing the potential difference.

*Recombination rates:* The recombination term in Eq. (1.4) is assumed to be of Langevin type which reads

$$R(x,y) = \gamma n(x,y)p(x,y) \tag{1.8}$$

with $\gamma = q\mu/\epsilon_0\epsilon_r$ and $\mu = min[\mu_p, \mu_n]$ [46, 47]. Note that this rate expression does not allow to explicitely discriminate between geminate pair and nongeminate pair recombination.

*Generation rates and exciton motion:* Assuming a Lambert-Beer type absorption profile across the device, an absorption rate $A(x, y)$ accounting for the number of photons absorbed per second and volume can be introduced as

$$A(x,y) = \int_0^{\frac{hc}{E_{gap}}} \Phi_0(\lambda) \frac{\lambda \alpha(\lambda)}{hc} e^{-\alpha(\lambda)x} d\lambda. \tag{1.9}$$

where $\alpha(\lambda)$ denotes the absorption coefficient related to the organic and inorganic species, $c$ the speed of light, $h$ the Planck constant, $E_{gap}$ the optical bandgap, and $\Phi_0(\lambda)$ the solar spectrum used (AM 1.5 with 500 $\mathrm{Wm}^{-2}$). In this formulation, Eq. (1.9) yields the photon number as a function of the material-dependent absorption and, in reasonable first approximation, the morphology of the device. As we intend to focus on investigating the role of the morphology for *carrier transport*, we will exclude additional morphology-related effects that may originate from strongly spatially varying absorption profiles [48] by introducing the following simplifications: (i) $\alpha$ enters Eq. (1.9) as a wavelength- and material-independent parameter and (ii) the optical band gap $E_{gap}$ is treated as material-independent. This means that both materials are considered to be capable of absorbing the same number of photons per volume and time. Then, the actual number of photons absorbed anywhere in the device is only determined by Lambert Beer's law, i.e., is solely dependent on the position of the considered volume element with respect to the transparent electrode. The coefficient $\alpha$ is set to the representative value of $2 \times 10^7\ m^{-1}$. With the help of the simplifications made above, we are able to compare also materials whose the optical absorption is not known quantitatively.

In the inorganic phase, light absorption leads directly to free charges. The generation rate $G(x, y)$ associated to this process is, thus, directly given by $G(x, y) = A(x, y)$ [49]. Within the organic phase, the absorbed photons give rise to an exciton density distribution $ex(x, y)$. Since excitons have no charge, exciton migration, described by a flux density $\Phi_{ex}(x, y)$, is determined only by diffusion:

$$\mathbf{\Phi}_{ex}(x,y) = -k_B T \mu_{ex} \nabla ex(x,y) \tag{1.10}$$

with $\mu_{ex}$ being the exciton mobility. The continuity equation contains an

Table 1.1: Material parameters used in the device simulations

| | |
|---|---|
| Donor: P3EBT HOMO/LUMO: | -5.6 eV / -3.7 eV |
| Acceptor: $CuInS_2$ $E_C/E_V$: | -5.6 eV / -4.1 eV [51] |
| Relative dielectric constant: $\epsilon_r$ | 3.0 |
| Electron and hole mobility: $\mu_n = \mu_p$ | $10^{-8}$ $m^2/(Vs)$ |
| Exciton lifetime: $\tau_{ex}$ | 1 nm [52] |
| Exciton mobility: $\mu_{ex}$ | $3.86 \times 10^{-6}$ $m^2/(Vs)$ |
| Absorption coefficient: $\alpha$ | $2 \times 10^7$ $m^{-1}$ |
| Optical bandgap: $E_{gap}$ | 1.5 eV |
| Hole concentration at the anode: | $10^{22}$ $m^{-3}$ |
| Electron concentration at the cathode: | $10^{22}$ $m^{-3}$ |

exciton generation rate $G_{ex}(x,y) = A(x,y)$ and has the form [50]

$$\frac{\partial ex(x,y)}{\partial t} + \frac{1}{q}\nabla\left(\mathbf{\Phi}_{ex}(x,y)\right) = G_{ex}(x,y) + \frac{1}{4}R(x,y) - R_{ex}(x,y) - G(x,y). \tag{1.11}$$

Herein, an exciton recombination rate $R_{ex}$ is defined as

$$R_{ex}(x,y) = \frac{ex(x,y)}{\tau_{ex}} \tag{1.12}$$

where $\tau_{ex}$ is the exciton lifetime. Carrier recombination $R(x,y)$ (*cf.* Eq. (1.4)) can give rise to the formation of singlet excitons and, thus, increases the exciton density. Thus, the fraction of $R(x,y)$ yielding singlet states needs to be considered in Eq. (1.11) and is taken here as $1/4$. Excitons dissociate into free charge carriers if they reach the organic-inorganic interface within their lifetime, i.e., the charge carrier generation rate $G(x,y)$ reads

$$G(x,y) = \begin{cases} 0 & , \ x,y \ \text{within organic material} \\ \dfrac{1}{\tau_{diss}} ex(x,y), & x,y \ \text{at organic} - \text{inorganic interface.} \end{cases} \tag{1.13}$$

As a further simplification of Eqs. (1.10,1.12), the parameters $\mu_{ex}$ and $\tau_{ex}$ are set to fixed values. We chose the values to $3.86 \times 10^{-6} m^2 V^{-1} s^{-1}$ and 1 $ns$

[52], respectively, to arrive at a mean exciton diffusion length of 15 $nm$. The values of all constants used in our simulations to describe exciton formation and migration are summarized in Table 1.1.

The resulting coupled system of equations (Eqs. (1.2,1.4-1.6,1.10,1.11)) is solved self-consistently on a two-dimensional mesh with variable grid spacing by using the discretization of the current density equations according to Scharfetter and Gummel [53].

Important device parameters of solar cells are the fill factor (FF) and the power conversion efficiency (PCE) which are related to the open circuit voltage $V_{\mathrm{oc}}$, the short circuit current density $j_{\mathrm{sc}}$, the voltage $V_{\mathrm{mpp}}$, and the current density $j_{\mathrm{mpp}}$ at the maximum power point by

$$FF = \frac{V_{\mathrm{mpp}} j_{\mathrm{mpp}}}{V_{\mathrm{oc}} j_{\mathrm{sc}}}$$

and

$$PCE = \frac{V_{\mathrm{mpp}} j_{\mathrm{mpp}}}{P_{\mathrm{in}}}$$

with $P_{\mathrm{in}}$ being the incident light power (1000 W/m$^2$). All simulations were carried out for room temperature.

## 1.5 Results and discussions

At first, we define a model system that allows us to discriminate between the effects arising from (i) the cell morphology, (ii) the choice of contacts, and (iii) the transport level alignment. To prevent such effects to be obscured by a possible dependence on additional material parameters, we will use identical parameter values for the donor and acceptor phase whenever possible (see below).

In order to implement representative model morphologies, one needs to bear in mind that the shape of the interface between the organic donor and the inorganic acceptor material in nanocomposite solar cells depends strongly on the actual fabrication procedure, *cf., e.g.,* [17, 18, 19, 20]. Such procedures aiming at obtaining a continuous phase of the acceptor material [9, 17, 18, 19, 20]. However, there are often acceptor nanoparticles that are fully surrounded

by the organic material [17, 18, 19, 20]. Varying the processing conditions may give rise to many different degrees of conglomeration [17, 18, 19, 20]. To capture the influence of such different interface morphologies, the following interface geometries were assumed in the simulation.

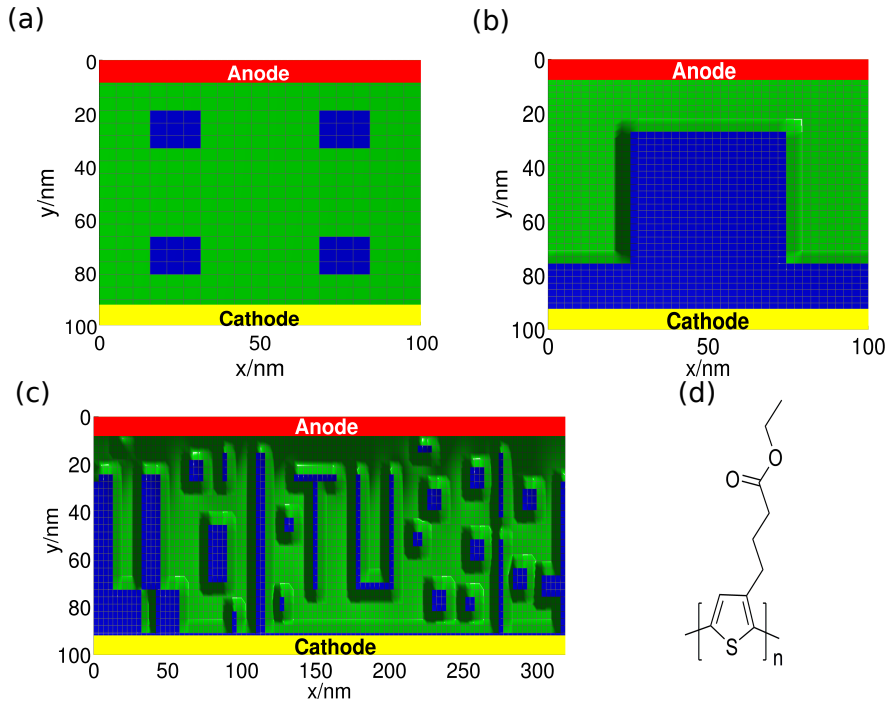


Figure 1.1: Interface morphologies: (a) comblike structure, (b) single nanoparticle structure, and (c) a superposition of (a) and (b). The area corresponding to the donor (P3EBT) is indicated in green, the one of the acceptor ($CuInS_2$) in blue. (d) Schematic structure of P3EBT.

As a first limiting case, an interdigitated array of donor and acceptor, a "comb-like"structure, was considered (*cf.* Fig. 1.1(a)). Such a geometry ensures (i) continuous pathways for the charge carriers to travel from the interface to the contacts and (ii) promises the highest sensitivity of the short circuit current with respect to a varying digit width [54]. Nanoparticles entirely embedded into the donor polymer matrix are investigated as second

limiting case (*cf.* Fig. 1.1(b)). Provided that the mobility of the phases can be assumed to be independent of the morphology, all other interface geometries can be considered as superpositions of interdigited phases and nanoparticles. A morphology as depicted in Fig. 1.1(c) is a mixture of a comblike and a single nanoparticle structure and may serve as a more realistic description of the donor-acceptor interface.

The material parameters assumed in the simulation are listed in Tab. 1.1. The position of the transport levels, i.e., the HOMO/LUMO levels of P3EBT, as determined from cyclovoltammetry, and $E_C/E_V$ of $CuInS_2$ [51] are depicted in Fig. 1.2(a). The remaining transport-related parameters, the carrier mobilities and the dielectric constants, are not varied throughout the simulations. The impact of these quantities and variations thereof are beyond the scope of this paper. The mobility is set to be the same for electrons and holes and independent of the donor and acceptor. Eventhough the mobilities of the materials most likely differ from each other and change when tuning the interface structure in an actual device, our choice has, nevertheless, two advantages for the theoretical assessment: (i) We can independently study effects arising from the interface morphology and effects related to different mobilities in the donor and acceptor phase. Moreover, it guarantees that all considered morphologies are studied using the same set of mobility values. (ii) As will be shown in detail elsewhere [55], the ratio between the mobilities of the two materials has, as can be expected, a significant impact on the I-V characteristic. In the hybrid solar cells considered here, however, mobility effects can be shown to (i) occur largely independent from morphology-related effects and (ii) be less pronounced than the latter [55]. Also the dielectric constant is assumed to be identical in both materials. This simple choice constitutes a valid starting point for our investigations, since, as shown in detail elsewhere [55], the effect of differing dielectric constants on the I-V curve is independent of and less marked than the three factors studied below.

Two types of contacts were investigated. In a first case, ohmic contacts for holes towards P3EBT and electrons towards $CuInS_2$, respectively, were chosen (Fig. 1.2a). [56] In a second scenario, ITO as cathode and Al as anode were chosen as actual contacts. These contact materials give rise to substan-

tial barriers for electrons and holes towards the contacts, *cf.* Fig. 1.2(a), i.e., form non-ohmic contacts.

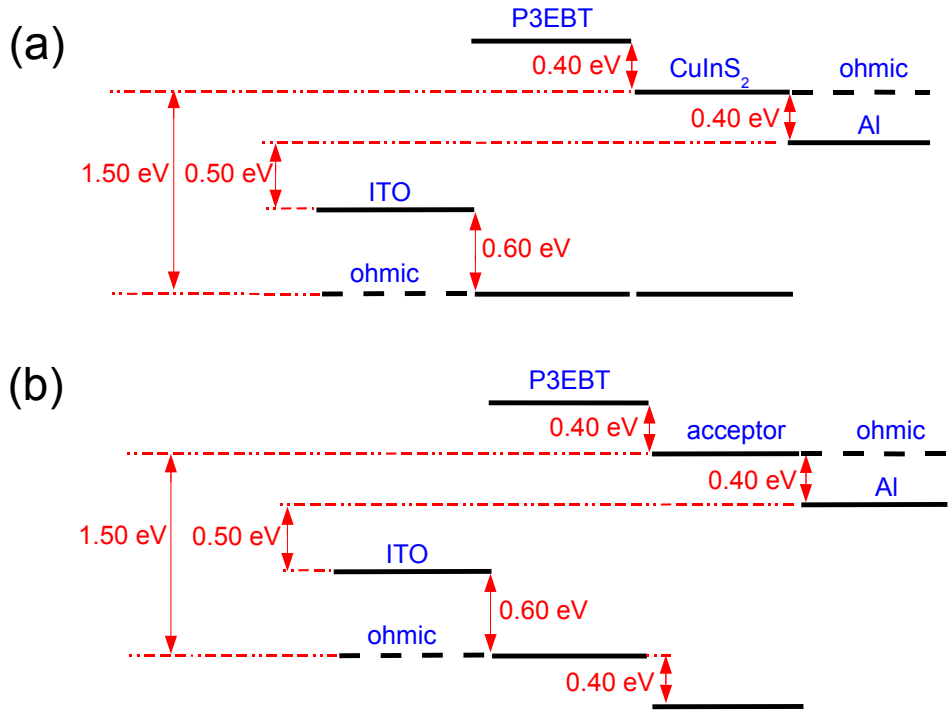


Figure 1.2: Position of HOMO and LUMO levels in P3EBT and $E_{\mathrm{C}}$, $E_{\mathrm{V}}$ for (a) $CuInS_2$ or (b) an idealized acceptor with equivalent transport level offsets with respect to P3EBT. Further shown is the alignment of the contact workfunctions corresponding to ohmic contacts for holes towards P3EBT and for electrons towards the acceptor, or to an ITO anode and Al cathode.

Throughout this work, we define the built-in voltage $V_{\mathrm{built-in}}$ as the difference between the work functions of the contacts, i.e., the bias necessary to compensate the potential difference across the device imposed by the contacts [57]. In case of ohmic contacts, we obtain a built-in voltage of $V_{\mathrm{built-in}} = 1.5$ V

for the interdigitated structure (*cf.* Fig. 1.2(a)). For the nanoparticle structure, however, $V_{\mathrm{built-in}}$ assumes the value of 1.9 V, since the cathode workfunction is aligned with the P3EBT donor LUMO level to ensure an ohmic contact. In case of the "real" structure, $V_{\mathrm{built-in}} = 1.5$ V coincides with the value of the interdigitated structure.

*Impact of interface geometry:* In the following, we will turn our attention to the relationship between the three aforementioned heterojunction morphologies and transport studied for a P3EBT/$CuInS_2$ device with ohmic contacts. Interdigitated structures whose combwidth $d$ is varied while keeping the area of the acceptor phase constant, give rise to I-V curves shown in Fig. 1.3(a). Table 1.2 lists the corresponding open circuit voltages $V_{\mathrm{oc}}$, short circuit currents $j_{\mathrm{sc}}$, fill factors (FF), and power conversion efficiencies (PCE). As can be seen from Fig. 1.3(a), the open circuit voltage $V_{\mathrm{oc}}$ remains constant at a value of 1.5 V independent of the combwidth $d$. This value coincides $V_{\mathrm{built-in}} = 1.5$ V of this system, as expected for ohmic contacts [58]. The short circuit current density $j_{\mathrm{sc}}$ increases with reducing the finger width $d$, since an increased number of donor excitons are able to reach the interface. This behavior has already been observed experimentally when changing (i) the combwidth of nanoimprinted organic solar cells [30] and (ii) the surface roughness of the donor-acceptor interface in a layered solar cell [59, 35].

Interestingly, as can be seen in Fig. 1.3(b), there is a pronounced dependence of $j_{\mathrm{sc}}$ on $d$. In the limit of small $d$, the $d$-dependent contribution to $j_{\mathrm{sc}}$ becomes nearly as large as the constant current contribution stemming from the acceptor phase due to bulk generation. A closer inspection of the evolution of $j_{\mathrm{sc}}(d)$ reveals two distinct regimes: (i) As long as the width exceeds *ca.* 100 $nm$, essentially those excitons migrating perpendicular to the contacts (y-direction in Fig. 1.1(a)) reach the interface and contribute to the current.

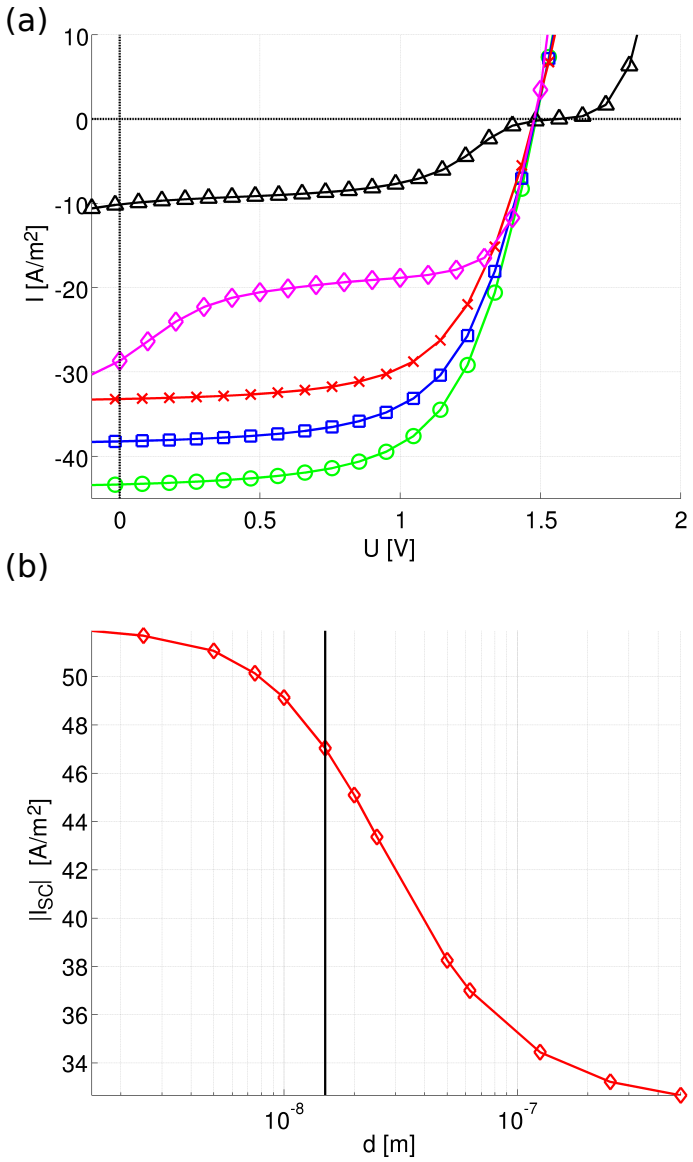


Figure 1.3: (a) I-V curves for the P3EBT/$CuInS_2$ interdigitated interface with finger width $d$= 250 nm (crosses,×), 50 nm (squares,□), and 25 nm (circles,○), nanoparticles (triangles,△), and real structure (diamonds,◇) in a device with ohmic contacts. (b) Dependence of the short circuit current density $j_{sc}$ on finger width $d$ for the interdigitated device with ohmic contacts. The exciton mean free path length of 15 $nm$ indicated by a vertical line.

Table 1.2: Open circuit voltage, short circuit current density, fill factor, and power conversion efficiency for devices varying in interface geometry and contact type.

| Assumed morphology | $V_{oc}$/V | $j_{sc}$/Am$^{-2}$ | FF / % | PCE /% |
|---|---|---|---|---|
| P3EBT/$CuInS_2$; ohmic | | | | |
| Comblike (combwidth 50 nm) | 1.48 | 38.3 | 61.3 | 6.50 |
| Nanoparticle structure | 1.57 | 10.2 | 44.0 | 1.38 |
| "Real" structure | 1.48 | 28.5 | 50.8 | 4.42 |
| P3EBT/$CuInS_2$; Al/ITO | | | | |
| Comblike (combwidth 50 nm) | 0.77 | 34.9 | 23.2 | 1.50 |
| Nanoparticle structure | 0.48 | 1.8 | 10.0 | 0.02 |
| "Real" structure | 0.77 | 18.4 | 36.6 | 1.10 |
| P3EBT/acceptor; ohmic | | | | |
| Comblike (combwidth 50 nm) | 1.88 | 39.1 | 58.6 | 8.62 |
| Nanoparticle structure | 1.80 | 30.8 | 35.7 | 3.96 |
| "Real" structure | 1.86 | 37.9 | 43.2 | 6.84 |
| P3EBT/acceptor; Al/ITO | | | | |
| Comblike (combwidth 50 nm) | 1.01 | 37.0 | 39.5 | 2.92 |
| Nanoparticle structure | 0.49 | 12.7 | 47.2 | 0.60 |
| "Real" structure | 0.99 | 25.4 | 38.8 | 1.94 |

As a consequence, only small changes in $j_{sc}(d)$ are observed. (ii) However, once the structure size drops below 100 $nm$, $j_{sc}(d)$ is quickly rising with decreasing $d$. For such $d$, there is a non-neglible fraction of excitons migrating parallel to the contacts (x-direction in Fig. 1.1(a)) that is able to reach heterojunction facets that are oriented perpendicular to the contacts. This result is in full agreement with previous theoretical studies on excitonic solar cells [33, 34, 50]. When further decreasing $d$, $j_{sc}(d)$ begins to saturate as soon as $d$ reaches the mean exciton diffusion length of 15 $nm$, as seen also in [33]. However, the maximum value of $j_{sc}(d)$ is reached at $d$ considerably smaller than 15 $nm$. Then, however, the actual values $j_{sc}$ have to be considered with care, as a macroscopic description is not necessarily valid at such

small structure sizes.

To gain insight into the role of the two different carrier generation mechanisms for the formation of I-V curves, we consult a representative spatial distribution of electron and hole concentration within the power quadrant. The steady state quantities associated to the maximum power point are illustrated in Fig. 1.4; the generalized potential for electrons (upper potential) and holes (lower potential), and charge carrier distributions of the interdigited structure are shown in the left column. Note here that the generalized potential incorporates the electrostatic potential superimposed with the transport level offsets. At $V_{\mathrm{mpp}}$, the potential across the interdigitated device (Fig. 1.4(a)) drops approximately linearly from the anode to the cathode. It resembles, as usually anticipated for this type of cells, the potential evolution predicted by the MIM model [60]. The resulting electric field, that is uniform in strength and position, ensures that electrons and holes being generated across the acceptor region can be spatially separated prior direct recombination. Driven by the field, the carriers accumulate at the contacts, i.e., the hole [electron] concentration (Fig. 1.4(c,e)) is highest at the anode [cathode].

However, a closer inspection of the two carrier distributions shown in Figs. 1.4(c, e) reveals profound differences: (i) The hole concentration drops continuously from anode to cathode, while there is a pronounced step in the electron distribution and (ii) the carrier concentrations at the heterojunction interface are enhanced with respect to the surrounding bulk. The first observation is a direct consequence of the level arrangement of the particular donor and acceptor materials investigated here. As a result of the vanishing barrier between donor and acceptor hole transport levels, holes lack a driving force enabling them to leave the acceptor region. Without being able to escape the acceptor, the holes are subject to significant recombination, since also electrons are confined to the acceptor region due to the barrier formed by the LUMO offset. The local enhancement of carrier density at the interfaces is due to the *donor* excitons (formed throughout the organic bulk) that dissociate at the heterojunction.

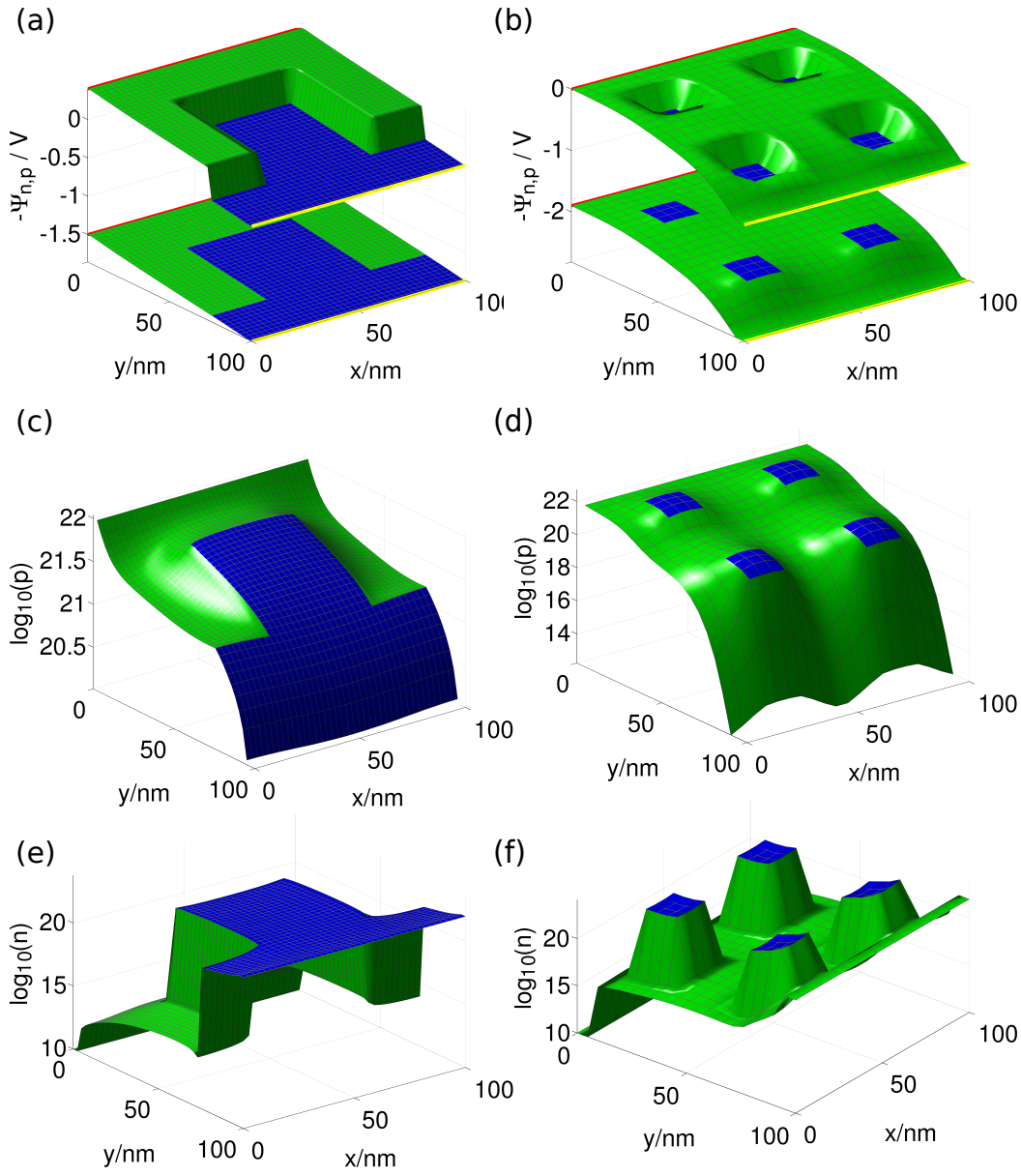


Figure 1.4: Steady state distribution of the potential (a,b), hole (c,d), and electron concentration (e,f) related to the comblike structure (left column) and isolated nanoparticle structure (right column). The area corresponding to the donor (P3EBT) is indicated in green, the one of the acceptor ($CuInS_2$) in blue.

As we assume bulk carrier generation throughout the inorganic acceptor rather than exciton transport with subsequent interface cleavage, the local gradient in hole concentration is much more pronounced in the donor phase (Fig. 1.4(c)). Moreover, the effect is less pronounced among the electrons (Fig. 1.4(e)).

When turning to isolated nanoparticles, a profoundly different I-V characteristic is observed (cf. Fig. 1.3(a)). To provide a quantitative comparison to the interdigited case, the interface length of the nanoparticles is chosen to coincide with the corresponding length of 50 nm wide fingers. I.e., in both cases the same area for exciton dissociation (i.e., interface carrier generation) is available. While $V_{\mathrm{oc}}$ is approximately the same, $j_{\mathrm{sc}}$ is reduced by a factor of almost four. Moreover, a pronounced plateau appears in the power quadrant that gives rise to an s-shaped curve. As a result of this shape, the fill factor of the cell is reduced (*cf.* Tab. 1.2). In combination with the low $j_{\mathrm{sc}}$, PCE is reduced by a factor of five with respect to the cell with comb-like interface. The strong reduction of the photocurrent compared to the comb geometry results from the combination of two factors: (i) As the LUMO level is lower in the acceptor than in the P3EBT donor, electrons are accumulated in the, at least in part, inorganic nanoparticles (*cf.* Fig. 1.4(b,f)). Thus, the number of carriers reaching the cathode is reduced. (ii) In addition to a lacking support for hole migration into the donor (*cf.* HOMO and $E_{\mathrm{V}}$ level in Fig. 1.2(a)), generated holes prefer to stay close to the acceptor due to the space charge caused by the high electron density in the acceptor material, as can be seen well when comparing the carrier distributions in Fig. 1.4(d,f). As a result, recombination processes are strongly reducing the hole concentration within the inorganic phase. Thus, the reduction in PCE is to a large extent, as will be shown below, a consequence of the particular combination of semiconductors considered here.

The I-V curve which corresponds to an "actual" structure (Fig. 1.3(a)) is located between the characteristics of the single nanoparticle structure and the comblike structures, but exhibits the same $V_{\mathrm{oc}}$. It possesses a pronounced plateau the onset of which is located at voltages lower than in the nanoparticle curve. In Fig. 1.5, the generalized potential and the current density

distribution in y-direction corresponding to the maximum power point, i.e., an external voltage of 1.3 V, are depicted. The distribution of potential and carrier concentrations are reminiscent to those seen in the individual cases. Since the net dark current is zero at this bias, the current close to cathode is a pure electron photocurrent and at the anode a pure hole photocurrent.

The pronounced negative maxima in the current density shown in Fig. 1.5(b) indicate that the main part of the electron current to the cathode is transported in the through-going acceptor paths. This adduces further evidence that comblike structures lead to best efficiencies. Moreover, it can be seen in regions close to the contacts depicted in Fig. 1.5(b) that the current is confined to the acceptor region, while the hole current appears to be spatially more uniform in the vicinity of the anode. This lack of confinement is related to the vanishing offset in the hole transport levels in donor and acceptor (Fig. 1.5(a)).

*Impact of the level offset*: To discriminate between the effect of morphology and the disadvantageous lack of an HOMO level offset, we replace $CuInS_2$ by a fictitious acceptor material whose HOMO and LUMO are equidistantly set off by 0.4 eV with respect to the P3EBT levels (Fig. 1.2 (b)). All other parameters including $V_{\mathrm{built-in}}$ were kept the same.

The corresponding I-V characteristics for the three model geometries assuming ohmic contacts are shown in Fig. 1.6(b,filled symbols). Compared to the curves obtained in the original P3EBT/$CuInS_2$ device Fig. 1.6(a), the following differences arise: Independent from the interface structure, $j_{\mathrm{sc}}$, $V_{\mathrm{oc}}$, and PCE are increased (*cf.* also Tab. 1.2) for idealized acceptor. However, the shape and, thus, FF are less ideal. While, e.g., the comb-like structure gives rise to an FF of 61.3 % in P3EBT/$CuInS_2$, FF drops to 58.6 % when changing the acceptor. At the same time, the enhanced values of $j_{\mathrm{sc}}$ and $V_{\mathrm{oc}}$ compensate for the loss in FF and effectively increase PCE from 3.25 % to 4.31 %. The origin of the decrease in FF and increase in $V_{\mathrm{oc}}$ is presumably discussed best for the case of the interdigitated interface. The apparent departure of the I-V curve from an ideal diode-like shape (Fig. 1.6(b)) turns out to be related to the bias-dependence of hole transport.

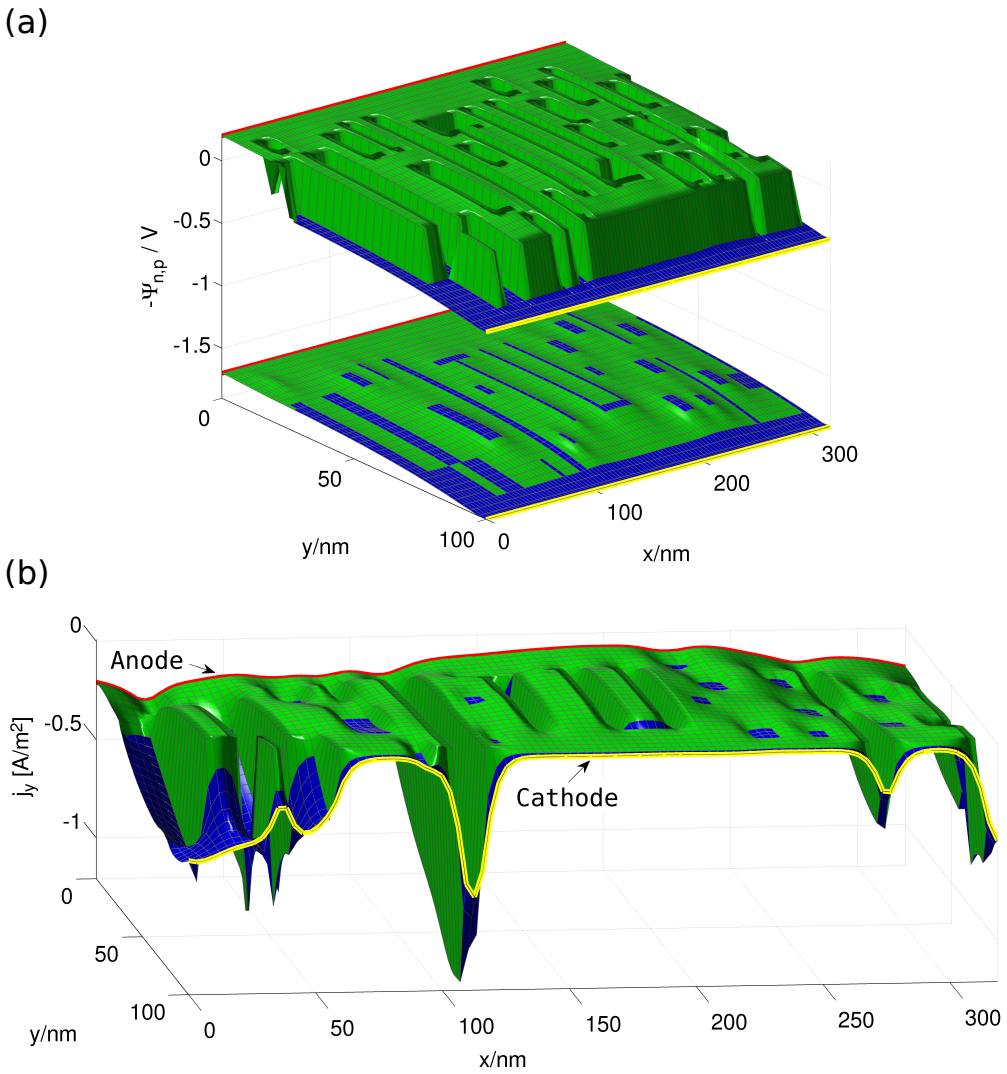


Figure 1.5: Generalized potential $\widehat{\Psi}_{n(p)}$ for electrons (holes) (a) and current density distribution in y-direction (b) of the intermediate structure at the maximum power point ($V_{\mathrm{mpp}} = 1.3$ V) of an illuminated cell. The area corresponding to the donor (P3EBT) is indicated in green, the one of the acceptor ($CuInS_2$) in blue. The vertical position of the yellow line in the lower panel indicates the electron current density at the cathode and the vertical position of the the red line the hole current density at the anode.

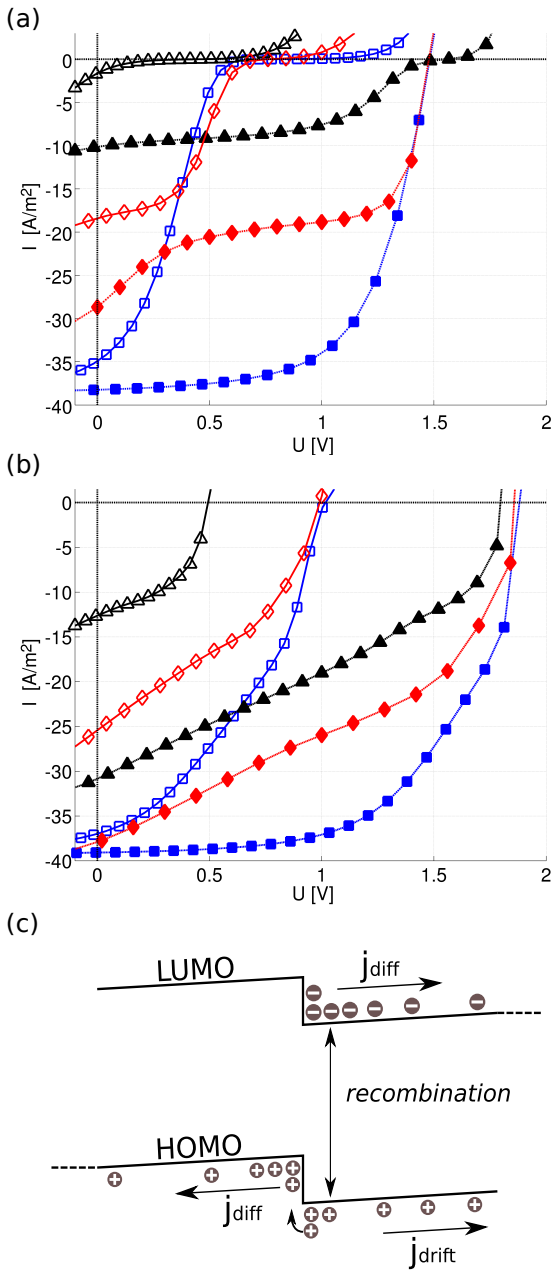


Figure 1.6: I-V curves for the interfaces of (a) P3EBT/$CuInS_2$ and (b) P3EBT/idealized acceptor in a device with Al and ITO contacts (open symbols) and ohmic contacts (filled symbols). Shown are the curves for the interdigitated interface (squares) with a finger width $d$= 50 nm, nanoparticles (triangles), and real structure (diamonds). (c) Sketch of the current contributions for a P3EBT/idealized acceptor device operating in the power quadrant.

Fig. 1.6(c) schematically depicts the general transport scenario valid for biases within the power quadrant. As discussed already in Figs. 1.4(a,e), the contribution from electrons to the overall current is not affected by the actual bias. For voltages not exceeding $V_{\mathrm{oc}}$, the corresponding electric field is not able to lift the electrons across the barrier at the interface. Therefore, all generated electrons diffuse towards the cathode (Fig. 1.6(c)). Holes that are generated throughout the acceptor and via exciton dissociation at the interface, give rise to a gradient in the concentration $p$ that induces a desired diffusion current through the donor towards the cathode (*cf.* Fig. 1.6(c)). However, due to the external bias there is a non-vanishing electric field that drives holes, in particular those generated close to the anode, towards the wrong contact. The higher $V$, the higher the loss in hole current due to such drift currents. With the introduction of an offset between the hole transport levels, holes regard the transfer from the interface into the donor region as energetically favorable (*cf.* Fig. 1.6(c)). I.e., there is an effective diffusion process that (i) diminishes $p$ within the acceptor and, thus, (ii) counteracts the disadvantegeous drift current. As a result, the photocurrent "decays" slowlier with $V$ than in a device without level offset. Thus, $V_{\mathrm{oc}}$ is increased beyond $V_{\mathrm{built-in}}$ and FF is reduced. Note that this effect is significantly less pronounced in purely exciton-based solar cells, since the predominant amount of holes contributing to the detrimental drift current, i.e., those generated in bulk, does not exist.

The most profound dependence of $j$ on the type of acceptor is observed for the nanoparticle geometry. Aided by a non-vanishing hole level offset, holes generated in the acceptor better escape into the donor and, thus, from the region of trapped electrons. Thus, recombination losses are strongly reduced.

*Impact of contacts:* To study the impact of actual contacts, aluminum with a workfunction of $\theta = -4.50$ eV (intrinsic electron concentration of $10^{29}$ m$^{-3}$) for the cathode and indium tin oxide (ITO) with a workfunction of $\theta = -5.0$ eV (intrinsic hole concentration of $10^{27}$ m$^{-3}$) have been considered. The position of the contact workfunctions with respect to the transport levels of P3EBT and $CuInS_2$ is depicted in Fig. 1.2(a). As the difference in the con-

tact workfunctions is exclusively dictating the built-in voltage, we arrive at $V_{\mathrm{built-in}} = 0.5$ V. The I-V curves considering Al/ITO contacts and interface geometries as introduced above are shown in Fig. 1.6(a) for P3EBT/$CuInS_2$ and in Fig. 1.6(b) for a P3EBT/idealized acceptor combination. In Tab. 1.2 the corresponding figures of merit can be compared between devices with ohmic and real contacts.

In comparison to the curves representing the ohmic case (indicated by closed symbols in Fig. 1.6), the I-V curves possess a lower $V_{\mathrm{oc}}$ (*cf.* also Tab. 1.2). This can be seen best for devices containing an idealized acceptor and through-going paths (Fig. 1.6(b), squares and diamonds): Actual contacts (open symbols) appear to shift the curves obtained for ohmic contacts (closed symbols) towards lower voltages by an amount of *ca.* 0.9 $V$. This value corresponds to $V_{\mathrm{built-in}}^{ohmic} - V_{\mathrm{built-in}}^{non-ohmic} = 1.0\ V$ corrected by small differences in diffusion contributions. As a result, PCE is reduced by at least a factor of 3, e.g., from 4.3 to 1.5 for the interdigitated interface. Note, that $V_{\mathrm{oc}}$ exceeds $V_{\mathrm{built-in}}$ by *ca.* 0.4 $V$ due to the aforementioned effective diffusion induced by the hole transport level offset. When turning to P3EBT/$CuInS_2$ devices, however, real contacts additionally induce strong changes in the shape with respect to their ohmic counterparts, as can be deduced from Fig. 1.6(a) and the FF values in Tab. 1.2. Correspondingly, both $j_{\mathrm{sc}}$ and PCE values are affected. Even for the most ideal heterojunction geometry, PCE drops by more than a factor of 4 from 3.25 to 0.75. For devices with through-going paths (Fig. 1.6(a), squares and diamonds), this change in shape is due to a photocurrent that (i) drops more rapidly with increasing $V$ and (ii) collapses into a pronounced plateau that is approximately centered at $V_{\mathrm{oc}}$. Already at biases beyond 0.6 V, the net *photocurrent* vanishes. Electron and hole photo currents *cancel* each other exactly. This can be readily understood from the corresponding generalized potential distribution, shown for a representative external bias $V_{\mathrm{ext}} = 0.83$ V near $V_{\mathrm{oc}}$ in Fig. 1.7(a): The electron current is essentially caused by diffusion, as discussed previously (*cf.* Fig. 1.6(c)). All holes are driven by the drift force towards the cathode as their motion is not hampered by a band offset, and are, thus, moving into the same direction as the electrons (Fig. 1.7(a)).

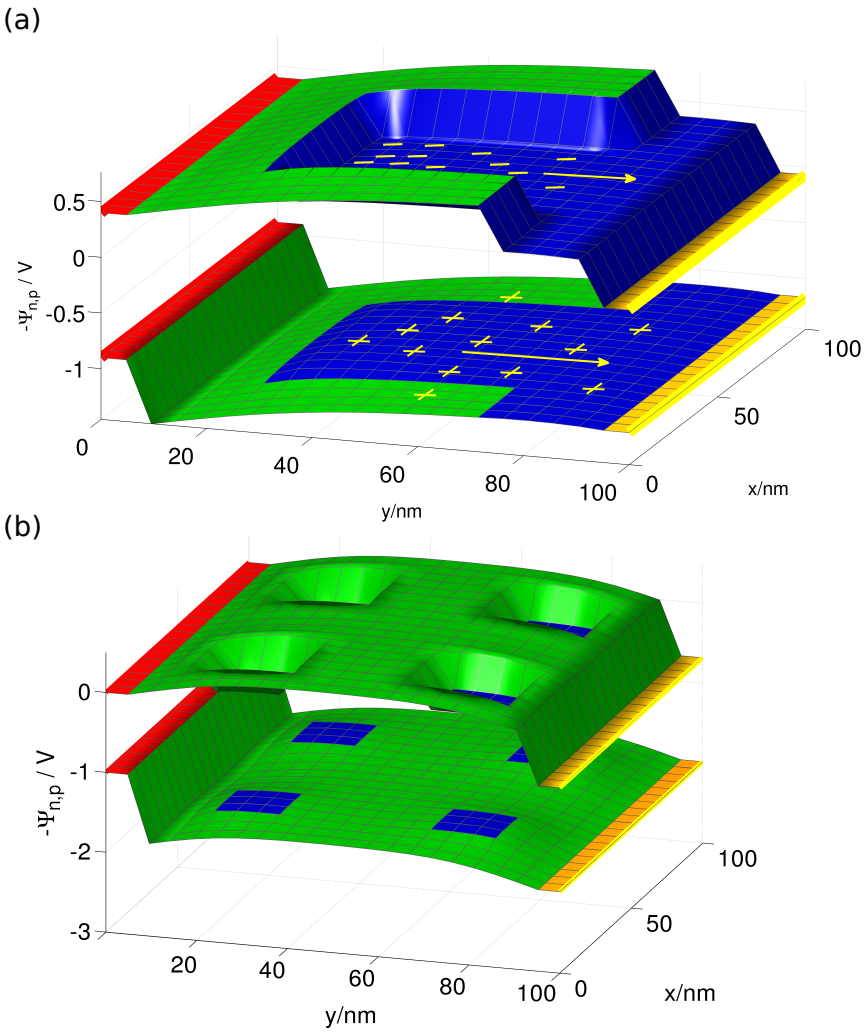


Figure 1.7: Generalized potential $\widehat{\Psi}_{n(p)}$ for electrons (holes) of a device with (a) a comb-like interface at $V_{\text{ext}} = 0.83$ V bias and (b) a nanoparticle interface and Al/ITO contacts at $V_{\text{ext}} = 0.32$ V bias. The area corresponding to the donor (P3EBT) is indicated in green, the one of the acceptor ($CuInS_2$) in blue. Electrons [/holes] in the $E_{\text{C}}$ [/$E_{\text{V}}$] level are schematically indicated by "-" [/"+"].

This condition, of course, promotes a further reduction of the carrier concentrations due to efficient recombination. A similar mechanism was revealed by C. Uhrich *et al.* [36] when changing the level offset between hole trans-

porting moities in a layered organic solar cell. In the vicinity of $V_{\mathrm{oc}}$, the I-V curves are already dominated by the dark characteristic. The onset of the dark electron current eventually occurs at a voltage of about 0.9 V, i.e., an appreciable amount of electrons can cross the non-illuminated device at biases exceeding the sum of $V_{\mathrm{built-in}} = 0.5$ V and the barrier posed by the LUMO/LUMO band offset of 0.4 V. Note that the corresponding hole dark current is very small, since (i) the hole concentration at the ITO contact is small and (ii) a large injection barrier from ITO into P3EBT is present. The degree to which the s-shape evolves can be further influenced by the height of the injection barrier present at the contacts. For a given built-in voltage, an increase of the injection barrier height associated to thermoionic injection was shown to induce a sigmoidal shape in the I-V curve while not affecting $V_{\mathrm{oc}}$ [33].

The most significant influence of the contacts is seen for the nanoparticle devices (Fig. 1.6, upper triangles). The open circuit voltage is with $V_{\mathrm{oc}} \approx V_{\mathrm{built-in}} = 0.5\ V$ independent from the acceptor material. A vanishing photocurrent at voltages beyond $V_{\mathrm{built-in}}$ is an indication for a loss in selectivity of the contacts. Indeed, when inspecting the generalized potential at a bias of 0.32 $V$ near $V_{\mathrm{built-in}}$ shown in Fig. 1.7(b), we recognize a strong deviation from a linear voltage drop from anode to cathode. Rather, the potential is almost flat and bends slightly downward from the device's center towards the contacts due to electron accumulation in the nanoparticle regions and close to the cathode. Therefore, electrons and holes experience on average similar driving forces towards each of the contacts; the *net* photo current vanishes.

For the P3EBT/$CuInS_2$ device, i.e., in the device lacking a hole transport level offset, $j_{\mathrm{sc}}$ vanishes almost to zero. Here, acceptor-generated holes do not leave the nanoparticles sufficiently fast and, thus, are subject to efficient recombination with electrons trapped in the acceptor. As a result, its I-V curve is characterized by a very small $j_{\mathrm{sc}}$ value of 2 $\mathrm{Am}^{-2}$, and a broad plateau centered around $V_{\mathrm{oc}}$, i.e., the fill factor is lowered from 0.23 to 0.10 (*cf.* Table 1.2). In comparison to the device with ideal contacts, the resulting PCE drops by an order of magnitude from 0.69 to 0.01.

## 1.6 Conclusion

The carrier transport in hybrid cells has been studied in the light of interplay between (i) energy barriers formed at the contacts, (ii) barriers at the donor-acceptor interface, and (iii) representative shapes of the heterojunction. Particular attention has been paid to the fact that carrier generation can occur at the heterojunction (due to dissociation of the donor excitons) *and* in the bulk of the acceptor material (due to band to band generation in the inorganic material).

Each of the three factors consitutes a major loss factor that profoundly determines the power conversion efficiency of hybrid organic-inorganic solar cells. As expected, the choice of the interface geometry has a crucial influence on the device efficiency even if perfect contacts are considered. In accord with previous investigations [27, 54, 61], interdigitated structures are found to yield the highest efficiencies. In such highly ordered systems, $j_{\mathrm{sc}}$ is limited by the digit width and, thus, by the exciton diffusion length [29, 62]. This is true independent from the nature of the contacts.

The presence of isolated islands in the device, be them formed by the donor and/or acceptor material, reduces the overall efficiency. The extent of this reduction strongly depends on the actual ratio between through-going pathways and isolated particles. The location of the maximum power point is determined by an interplay of two essential effects: The more through-going paths exist, (i) the more short circuit current can be obtained and (ii) the larger the area at which advantageous contact barriers can be offered, i.e., the more the plateau (s-shape) formation in the I-V curve can be suppressed.

As a second factor, it turns out that a vanishingly small or a negative hole transport level offset leads to an accumulation of holes in the nominally electron transporting acceptor zone. The resulting reduction of the photocurrent due to (i) direct hole and electron photocurrent compensation and (ii) recombination represents a major contribution to the overall efficiency loss. A straightforward way to avoid losses due to non-ideally shaped I-V curves is, therefore, to select the semiconducting materials so that the hole transport level offset at the heterojunction promotes hole diffusion into the

donor. Note, that this criteria for chosing transport levels has to be distinguished from other, already well employed rules: As a first requirement it is commonly accepted that a significant offset in the LUMO levels ensures efficient exciton dissociation [58]. Secondly, it is advantageous to block the charge carriers prior entering the opposing contact (see, e.g., in [63]); however, there are no restrictions in which part of the solar cell this blocking needs to occur. Despite the determining influence of the level offsets, the efficiency of the device is strongly influenced by the choice of contacts. As soon as non-ohmic contacts to the semiconductors are formed, the open circuit voltage is dictated by the contact workfunctions; $V_{oc}$ differs from $V_{built-in}$ only by a small possible amount corresponding to the smallest transport level offset arising from diffusion. For our choice of materials, $V_{oc}$ is halved when introducing Al/ITO contacts. Moreover and less expectedly, barriers at the semiconductor metal interfaces give rise to a substantial deviation from the ideal diode-shaped I-V curve and, thus, reduce the fill factor. As shown by Yip et al. [64] for ZnO-based bilayer hybrid solar cells, the systematic tuning of just the cathode workfunction via SAMs revealed fill factors varying by a factor of two. From the considerations above it is possible to conclude that the three investigated factors give rise to equally serious efficiency losses. As each of these factors directly relates to the properties and processing of the chosen materials, we can derive the following guidelines to select suitable material combinations: (i) The formation of ohmic contacts ensures contact-independent open circuit voltages *and* high fill factors. (ii) A successful suppression the formation of donor or acceptor islands is boosting the FF. And, (iii), holes need to be driven from the acceptor into the donor at the heterojunction by means of an effective diffusion induced by a transport level offset.

## Acknowledgment

This work has been supported by the Austrian Federal Ministry of Economy, Family, and Youth (bmwfj), ISOVOLTAIC GmbH, and the Austrian

Nanoinitiative (FFG) through the NILsimtos project as part of the NILaustria cluster.

# Part II

# Organic Field-Effect Transistors

# Chapter 2

# Relation between injection barrier and contact resistance in top-contact organic thin-film transistors

## 2.1 Preamble

The following work is published in Organic Electronics in 2012 [6] by M. Gruber, F. Schürrer and K. Zojer.

## 2.2 Abstract

We theoretically investigate the carrier injection into top-contact bottom-gate organic thin film transitors. By means of a two-dimensional drift-diffusion model, we explicitly consider thermionic and tunneling injection in combination with subsequent carrier transport into the device. Based on numerical simulations with this model, we determine the contact resistance as a function of the nominal hole injection barrier height and temperature. Depending on the barrier height or the operating temperature, we find three distinct injection regimes. Our work reveals that in all three regimes self-

regulating processes exist due to which the influx of current is adjusted according to the needs of the channel at the given point of operation.

We explain why the transmission/transfer line method (TLM) for the determination of the contact resistance, $R_c$, quantitatively fails for non-quasi-ohmic injection. Self-regulation links the contact resistance to the channel resistance and the contact resistance becomes dependent on the channel length. For larger channel lengths, $R_c$ is underestimated by TLM; the method yields overestimated values for small channel devices.

## 2.3 Introduction

Organic thin-film transistors represent an excellent example which illustrates that the operation of organic electronic devices is not straight-forwardly governed by the properties of the active materials alone. Rather, the geometry of the device, i.e., the channel length [65, 66, 67, 68], the layer thicknesses [69, 70], the position of interlayers [70, 71, 72], as well as the size and arrangement of the electrodes with respect to the semiconductor [73, 74] are vital to achieve the desired performance.

One of the largest conceptual challenges in the forth-coming optimization of organic thin-film transistors [72, 75, 76, 77] and circuits thereof [78, 79] in terms of switching speed is to produce small channel lengths[65, 66, 67, 68, 72], to suppress small channel effects, and to improve the injection of carriers into the semiconductor [72, 80, 81, 82, 83]. The contact resistance, a quantity that provides a measure for the injection efficiency into OTFTs, was shown to particularly depend on the device geometry. Staggered, i.e., top-contact-bottom-gate or bottom-contact top-gate OTFTs posses contact resistances $R_c$ that are orders of magnitude lower than their coplanar, i.e., bottom-contact bottom-gate counterparts for the same materials. It has been demonstrated that the contact resistance is not only determined by the height of the injection barrier between the electrode metal and the organic semiconductor [84, 85], but also depends on the position [69, 73, 84, 86, 87, 88, 89, 90] and extension [84] of the injecting contacts. However, the origin

of this profound discrepancy in $R_c$ is still subject to debate. With the help of simulations *Tessler et al.*,[84] *Hill*,[87] and *Wang et al.* [90] argue that staggered devices have intrinsically a smaller $R_c$ than the coplanar ones due to the *arrangement* of the electrodes. However, *Braga* and *Horowitz* argue in accord with *Frisbie et al.* that clusters of evaporated metal interpenetrating the semiconductor are lowering $R_c$ in staggered top-contact devices.[91, 92]

It is the aim of this work to gain an in-depth understanding of the nature of injection for a particular electrode arrangement, *i.e.*, for *top-contact bottom-gate* OTFTs to permit a discrimination between effects arising from the ideal geometry and effects due to imperfections, e.g., due to locally altered material compositions and morphologies. We employ theoretical modelling in order to clarify, how the injection and the associated contact resistance $R_c$ are related to two essential "tuning handles" that can be modified in experiment to "control" carrier injection: (i) the nominal injection barrier height $\Phi$ at the electrode-semiconductor junction and (ii) the temperature $T$. The reliable extraction of the contact resistance is crucial for the correct determination of the charge carrier mobility[92, 93, 94, 95], in particular with its temperature-dependence.[73, 74, 96]

## 2.4 Methodology

For the purpose of studying the impact of the injection barrier, we developed a simulation tool based on a two-dimensional drift-diffusion model, that is capable of (i) self-consistently describing the field- and temperature dependence of the injected current, (ii) incorporating thermionic and tunneling injection to study also possible scenarios at high barriers and low temperatures, and (iii) subsequent carrier transport in the device as a function of the electrode arrangement. With the help of a simple equivalent circuit model, the steady-state potentials and the device current can be further analyzed to determine the values of contact and channel resistances. Note that present analytical models for the determination of the contact resistance in OTFTs are not suited for this purpose, as such models only indirectly consider the

impact of injection barriers [69, 80, 90, 97] or need to impose assumptions such as the presence of thermionic emission [80, 90, 98] and bulk-limited current [80, 90]. Moreover, the analytical description of the crucial phenomenon of current crowding [69, 90] relies on the applicability of the transmission/-transfer line method (TLM).[99] However, this applicability of TLM is not, as will be shown below, uniquely justified for all relevant injection barriers.

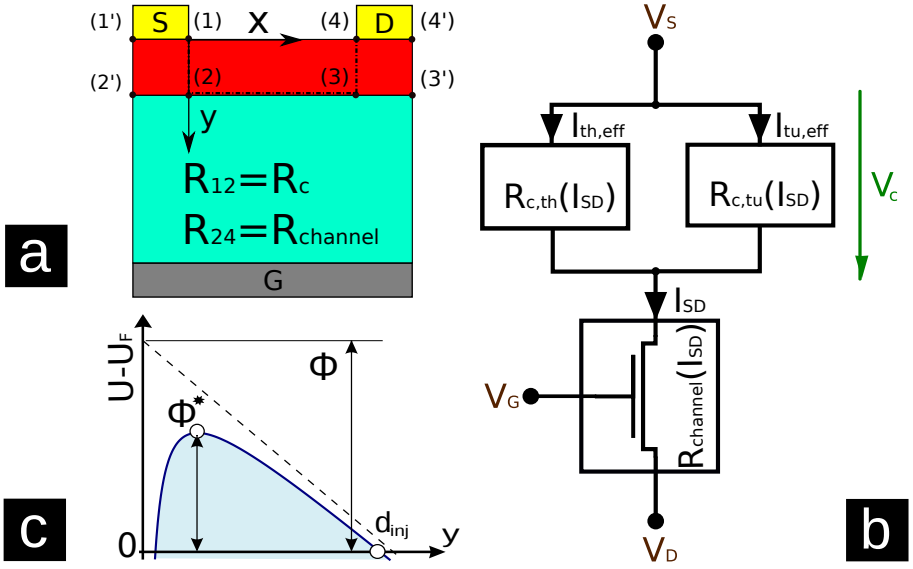


Figure 2.1: (a) Schematic cross-section of a top-contact bottom-gate organic thin-film transistor. The dashed line indicates the path along which current density and potential distributions are evaluated (see text). Particularly distinguished positions in the cross-section are labeled. (b) Equivalent circuit of (a) consisting of the thermionic emission and tunneling contact resistances $R_{\mathrm{c,th}}$, $R_{\mathrm{c,tu}}$ and an ideal transistor channel resistance $R_{\mathrm{channel}}$. (c) Shape of the injection barrier under the combined influence of an external electric field and the Coulombic attraction between the injected charge and its image in the electrode (solid line) and under the influence of an external field only (dashed line). The maximum of the solid curve defines the effective barrier height $\Phi^*$ (Eq. (2.2)). The nominal injection barrier height $\Phi$ is the difference between the energy of the hole transport level in the semiconductor and the workfunction of the contact metal. The parameter $d_{inj}$ marks the distance from the metal semiconductor interface at which the injection barrier is zero.

The cross-section of a top-contact bottom-gate thin-film transistor is schematically shown in Fig. 2.1(a). To ease the analysis of the simulations in terms of contact-related effects, the semiconducting layer is partitioned into the contact region (1)-(1')-(2')-(2), i.e., the region from which all injected carriers collected prior entering the channel at position (2), and the channel region (between positions (2)-(4)).

*Drift-diffusion simulations:* To predict the potential distribution across the device due to the net concentration of injected carriers, we use a two-dimensional drift-diffusion-based model. Charge carrier injection is considered via boundary conditions (BC) at the source and drain electrodes.

These boundary conditions contain the injected and outgoing current densities across the metal-semiconductor interface for the current density equations. For the sake of simplicity, we consider only hole injection. The nominal hole injection barrier $\Phi$ is the difference between the workfunction of the contact metal and the energy of the hole transport level in the semiconductor (*cf.* Fig. 2.1(c)). We start out from a Schottky barrier at the interface[100, 101, 102, 103]

$$U(x,y) = \Phi - \frac{q^2}{16\pi\epsilon_0\epsilon_r(x)y} - qE_\perp(x, y=0)y. \tag{2.1}$$

with $q$ denoting the elementary charge, $\epsilon_0$ the vacuum permittivity, and $\epsilon_r(x)$ the relative static permittivity of the semiconductor. The expression contains, as indicated in Fig. 2.1(c), the combined influence of (i) the nominal hole injection barrier $\Phi$ and (ii) an external electric field component $E_\perp(x, y = 0)$ normal to the contact interface, i.e., the y-component of the field in our setup, due to which a triangular-shaped barrier along the $y$-direction is formed (dashed line in Fig. 2.1(c)). The final shape of the barrier $U(x, y)$ results from a superposition of the triangular barrier with (iii) the Coulombic attraction between the injected charge and its image in the electrode (solid line in Fig. 2.1(c)). If the field $E_\perp(x, y = 0)$ is positive, $U(x, y)$ possesses a well-defined maximum $\Phi^*(x)$ with

$$\Phi^*(x) = \Phi - q\sqrt{qE_\perp(x, y=0)/4\pi\epsilon_0\epsilon_r(x, y=0)}. \tag{2.2}$$

$U(x,y)$ acts as barrier for injection when $\Phi^*$ is positive, i.e., $U(x,y)$ possesses additionally two roots. Then, the larger root represents the barrier extension $d_{\mathrm{inj}}$ from the interface into the semiconductor and $\Phi^*$ is the effective barrier height [100, 101, 102, 103]. If, on the other hand, $E_\perp(x, y=0) < 0$, $U(x,y)$ continues to rise beyond $\Phi$ in y-direction and, thus, prevents carrier injection. Carriers injected across the barrier due to *thermionic emission* give rise to a current density $J_{th}$ into the $y$-direction (Fig. 2.1(a)),

$$J_{th}(x) = AT^2 e^{-\frac{\Phi^*(x)}{k_B T}}, \tag{2.3}$$

in which $A$ is the Richardson constant and $T$ the temperature. Due to the finite extension $d_{\mathrm{inj}}$ of the barrier $U(x,y)$ in $y$-direction (*cf.* solid line in Fig. 2.1(c)), the following procedure is applied to map the entire injection process onto a current density-containing boundary condition located at $y = 0$: Rather than using the electric field $E_\perp(x,y)$ given by the electrostatic potential drop close to the electrode-semiconductor interface, we average $E_\perp(x,y)$ for all positions $y$ within the barrier $U(x,y)$, i.e., $0 \leq y \leq d_{inj}(x)$, to arrive at a mean electric field $E_{\perp,eff}(x) = \Phi/d_{inj}(x)$. If injection is permited by the sign of $E_{\perp,eff}$, this $E_{\perp,eff}$ enters $\Phi^\star$ in Eq. (2.2) as barrier-shaping field. Otherwise, i.e., if $E_{\perp,eff} < 0$, $E_{eff,\perp}$ is set to zero to prevent complex valued $\Phi^\star$. As due to this assigment $\Phi^\star$ becomes $\Phi$ in Eq. (2.2), injection could occur according to Eq. (2.3); this spurious injection is compensated by the back drift current density (*vide infra*) that occurs as soon as $E_{\perp,eff} < 0$. It should be noted that due to a possibly marked dependence of the electric field $E_{\perp,eff}$ on the position $x$ below the contact, the amount of injected carriers is determined by the distance of the injection position from the channel. This is the origin of current crowding, i.e., that the carriers are mainly injected from the contact edge closest to the channel entrance.[69, 90, 100]

The current density $J_{tu}$ due to *tunnelling* is nominally independent from temperature, but strongly dependent on the barrier shape $U(x, y=0)$ (Eq. (2.1)). In our model, $J_{tu}$ is directed along the $y$-direction and is considered at the interface $y = 0$. In general, $J_{tu}$ depends on the injection position $x$ at the source contact and can be expressed in WKB approximation as [100, 102]

$$J_{tu}(x) = J_t \left[\frac{E_{\perp,eff}(x)}{E_t t(h(x))}\right]^2 \exp\left(-\frac{E_t v(h(x))}{E_{\perp,eff}(x)}\right) \tag{2.4}$$

in which

$$J_t = \frac{q\Phi^2}{9\left(\pi a_0\right)^2 \hbar R} \qquad \text{and} \qquad E_t = \frac{4\Phi^{3/2}}{3qa_0\sqrt{R}},$$

$a_0$ is the Bohr radius and $R$ the Rydberg constant. Moreover,

$$v(h(x)) = (1+h(x))^{1/2}\left[\mathcal{E}\left(\sqrt{\frac{1-h(x)}{1+h(x)}}\right) - h(x)\,\mathcal{K}\left(\sqrt{\frac{1-h(x)}{1+h(x)}}\right)\right],$$

$$t(h(x)) = (1+h(x))^{-1/2}\left[(1+h(x))\,\mathcal{E}\left(\sqrt{\frac{1-h(x)}{1+h(x)}}\right) - h(x)\,\mathcal{K}\left(\sqrt{\frac{1-h(x)}{1+h(x)}}\right)\right],$$

$$h(x) = \Phi^{-1} q\sqrt{\frac{qE_{\perp,eff}(x)}{4\pi\epsilon_0\epsilon_r(x)}},$$

with $\mathcal{E}(\mathcal{Y})$ and $\mathcal{K}(\mathcal{Y})$ being the complete elliptic integrals of the first and second kind of the argument $\mathcal{Y}$, respectively.

The *backflowing current density* $J_{bf}(x)$, i.e., the current density flowing from the semiconductor to the electrode, is determined by the back-drift, $J_{bd}(x)$, and interface recombination current densities, $J_{ir}(x)$:

$$J_{bf}(x) = J_{bd}(x) + J_{ir}(x) \tag{2.5}$$

with

$$J_{bd}(x) = \begin{cases} \mu(x,y)p(x)qE_y(x) & E_\perp(x) < 0 \\ 0 & E_\perp(x) > 0. \end{cases} \tag{2.6}$$

$$J_{ir}(x) = \frac{AT^2}{n_0} p(x) \tag{2.7}$$

Therein, $p(x)$ is the hole density within the semiconductor next to the source electrode at position $x$, $n_0$ the density of occupiable states, and $\mu(x,y)$ the hole mobility. The field-dependence of $J_{bd}(x)$ ensures that carriers can leave the device.

The net injected current density due to injection is

$$J_{inj}(x) = J_{th}(x) + J_{tu}(x) - J_{bf}(x). \tag{2.8}$$

We impose a temperature activated hole mobility

$$\mu(x, y) = \mu_0 \exp\left(-E_A/(k_B T)\right), \tag{2.9}$$

where $E_A$ denotes the activation energy and $\mu_0$ represents the mobility at infinite temperature. It has been previously emphasized that bulk traps located in the semiconductor below the injecting electrodes markedly contribute to the perceived contact resistance. [69, 80, 97] We account for such traps, e.g., formed at grain boundaries, by adjusting the value of $E_A$. As we are considering a top-contact bottom-gate setup, i.e., the contacts are deposited on a non-structured semiconducting layer, we assume a spatially uniform mobility. The system of equations containing the Poisson, drift-diffusion current density, and continuity equation with the appropriate boundary conditions is solved self-consistently on a non-regular two-dimensional grid using a Scharfetter Gummel method [70] combined with an implicit time integration. The lateral extension of the source and drain contacts is 10 $\mu$m; a further enlargment of the contacts did not change steady state currents and potentials anymore. Furthermore, the contacts are assumed to have a certain thickness ($d_{\text{contact}}$ = 11 nm) . Thus, the Poisson equation is solved also in the 11 nm thick layer of air above the uncovered semiconductor (*cf.* Appendix). This ensures numerical stability when considering local electric fields at high barriers $\Phi$.

If not stated otherwise, all simulations were obtained by using representative values that correspond to a pentacene-$SiO_2$ OTFT: The dielectric constants are $\epsilon_{r,SiO_2}$ =3.9 and $\epsilon_{r,pentacene}$ = 3.4. The thickness of oxide $d_{ox}$=147 nm and that of the semiconductor to $d_{sc}$=30 nm. The width of the device being necessary to determine the current $I_{\text{SD}}$ is $W = 7\ mm$.

*Equivalent circuit model:* With the help of the equivalent circuit shown in Fig. 2.1(b), the contact resistance $R_{\text{c}}$ is readily determined from the steady-state current $I_{SD}$ and potential distribution below the contact. To obtain the total injected current $I_{SD}$ (i.e., the current present at position (2) in Fig.

2.1a)), the injected net current density $J_{inj}(x)$ needs to be integrated along the whole source electrode extension ($(1') - (1)$ in Fig. 2.1(a)) in x-direction and multiplied with the width W of the transistor, i.e.,

$$I_{SD} = W \int_{(1')}^{(1)} \mathrm{d}x \; J_{inj}(x).$$

In full analogy, also the individual contributions to the injection current $I_{th}(J_{th})$, $I_{tu}(J_{tu})$, and $I_{bf}(J_{bf})$ can be obtained. Then, the steady-state current $I_{SD}$ can be formally decomposed into

$$I_{SD} = I_{th} + I_{tu} - I_{bf}. \tag{2.10}$$

The total resistance of the device $R_{\mathrm{tot}}$ is given by $V_{\mathrm{DS}}/I_{\mathrm{SD}}$ with $V_{\mathrm{DS}}$ being the externally applied drain-source bias and can be split into contributions of a channel resistance, $R_{\mathrm{channel}}$, and a net contact resistance, $R_{\mathrm{c}}$,

$$R_{\mathrm{tot}} = R_{\mathrm{c}} + R_{\mathrm{channel}}.$$

To resolve the contributions from the two injection mechanisms to $R_{\mathrm{c}}$, it is convenient to partition the net current from Eq. (2.10)

$$I_{SD} = (I_{th} + I_{tu}) \left[ 1 - \frac{I_{bf}}{I_{th} + I_{tu}} \right] = I_{eff,th} + I_{eff,tu},$$

such that the *effective* injection currents $I_{eff,th} = I_{th} - I_{bf} I_{th}/(I_{th} + I_{tu})$ and $I_{eff,tu} = I_{tu} - I_{bf} I_{tu}/(I_{th} + I_{tu})$ contain an amount of back-flowing current proportional to the corresponding injected current. Then, we can introduce a thermionic resistance, $R_{\mathrm{c,th}}$, and a tunneling resistance, $R_{\mathrm{c,tu}}$ :

$$R_{\mathrm{c,th}} = V_c/I_{eff,th} \qquad \text{and} \qquad R_{\mathrm{c,tu}} = V_c/I_{eff,tu}.$$

The parallel connection of these determine the overall contact resistance:

$$R_{\mathrm{c}} = \frac{R_{\mathrm{c,th}} R_{\mathrm{c,tu}}}{R_{\mathrm{c,th}} + R_{\mathrm{c,tu}}}.$$

## 2.5 Results and discussions

The structure of the considered top-contact bottom-gate OTFT is schematically depicted in Fig. 2.1(a). The geometry and material parameters are chosen such that the channel resistance $R_{\text{channel}}$ is expected to be small in comparison to $R_{\text{c}}$, i.e., that contact-limited current can be anticipated. The channel resistance is kept small by construction due to (i) a rather short channel length, i.e., $L = 5$ $\mu$m, (ii) a high intrinsic carrier mobility $\mu$ within the semiconductor, and (iii) and an operating point in the linear regime. In particular, we assume a room temperature hole mobility $\mu = 1$ cm$^2$/Vs.

### 2.5.1 Dependence of the contact resistance on the injection barrier

Our investigation covers injection barriers between $\Phi = 0$ eV and 1 eV to ensure that (i) the reported values of the prominent material combination Au/pentacene ranging from $\Phi = 0.47$[104], 0.5[105, 106] to 0.8[107] eV and, e.g., of Au/poly(3-hexylthiophene) (P3HT) $\Phi \leq 0.1$ eV are considered.[108, 109] In the following, the transistor is operated at fixed external drain-source $V_{\text{DS}}$ and gate-source bias $V_{\text{GS}}$ in the linear regime, i.e., $|V_{\text{GS}} - V_{\text{th}}| > |V_{\text{DS}}|$; $V_{\text{th}}$ is the threshold voltage being defined in the spirit of *Meijer et al.* [110] as the gate voltage at which the transport band at the OSC/dielectric interface is completely flat. Due to the absence of interface charges in our model, $V_{\text{th}}$ is exactly zero.

Prior turning to a discussion of the contact resistance, it is instructive to examine the typical electrostatic potential distribution of the device that results from the build-up of a steady state concentration of carriers below the source contact for a given injection barrier $\Phi$. To ease the discussion of the potential distribution, we will refer below to designated positions in the device; these positions are labeled in accord with Fig. 2.1(b). In the course of injection, carriers accumulate at the organic-dielectic interface opposite of the contacts, i.e., at (2)-(2') and, in the linear regime, below (3)-(3') in Fig.

2.1(a). If the accumulated steady state carrier density is not able to fully flatten the potential in the contact region of the semiconductor, a barrier-shaping field $E_{\perp}(x)$ remains.[84]

Due to this evident interplay between the actually injected current and a remnant barrier-shaping field $E_{\perp}(x)$ below the source contact, we relate in the discussion below the nominal injection barrier $\Phi$ to (i) the corresponding steady-state potential distribution in the device, shown in Fig. 2.2, (ii) the resulting injected current, and (iii) the resistances, both depicted in Fig. 2.3. The steady-state potential distribution across the entire device is exemplarily shown for the frequently used value $\Phi = 0.47$ eV for an Au-pentacene contact in Fig. 2.2(a).

As will be discussed in detail below, the shape of the potential in the contact region determines (i) how many charge carriers are going to be injected from the electrode and (ii) how they are transfered to the channel region. We give a close-up view on the potential distribution in the semiconducting layer as a function of the injection barrier $\Phi$ in Fig. 2.2(b). Moreover, we monitor in Fig. 2.2(c) the drop of the drain-source voltage $V_{\mathrm{DS}}$ in the following segments: (i) between the edge of source contact and the opposite position at the semiconductor-dielectric interface (1)-(2), (ii) in the semiconductor between source and drain edges at the interface to the dielectric (2)-(3), and (iii) between the semiconductor-dielectric interface at position (3) and the edge of drain contact (4). Note that the sum of all potential differences across the segments must amount to $V_{\mathrm{DS}}$.

*The case of small barriers (SB):*

When the injection barrier $\Phi$ is small, the source contact is able to inject an amout of carriers that exceeds the carrier concentration required to obtain a drain-source current $I_{\mathrm{SD}}$ that matches the *bulk-limited current* $I^{\mu}_{\mathrm{SD}}$,[111], i.e., the current that is dictated by the mobility $\mu(T)$, the thickness $d_{sc}$ of the semiconductor and $d_{SiO_2}$ of the dielectric material, the channel length $L$, the dielectric constants, and by the applied voltages $V_{\mathrm{DS}}$ and $V_{\mathrm{GS}}$. The steady state potential corresponding to such an ideal contact is represented by the case of a vanishing injection barrier $\Phi = 0$ in Fig. 2.2(b).

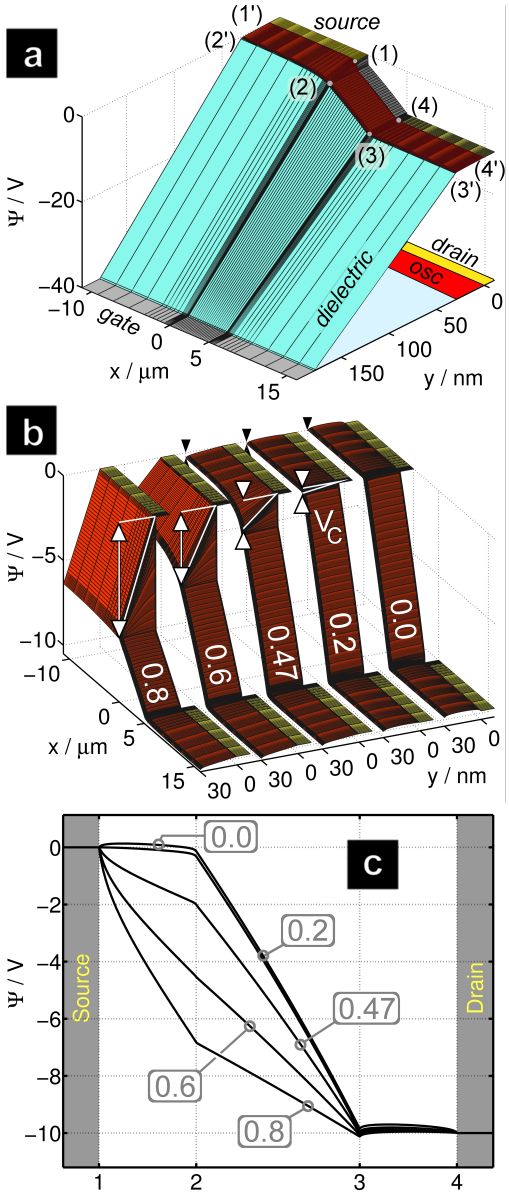


Figure 2.2: (a) Distribution of the steady state electrostatic potential for a hole injection barrier $\Phi$ = 0.47 eV with the labels of distinct positions as introduced in Fig. 2.1(b). (b) The electrostatic potential distribution in the semiconductor region for $\Phi$ = 0, 0.2, 0.47, 0.6, and 0.8 eV. White arrows indicate the potential difference $V_c$ between (1) and (2); black arrows correspond to the potential difference between (1′) and (2′). (c) Evolution of the potential along the current pathway (1)-(4) for $\Phi$ =0, 0.2, 0.47, 0.6, and 0.8 eV. In all cases, the transistor is operated at $V_{DS}$ = -10 V, $V_{GS}$ = -40 V, and at $T$ = 300 K.

It can be readily seen that the potential between the source electrode ((1) in Fig. 2.1(a)) and the semiconductor-dielectric interface ((2) in Fig. 2.1(a)) is almost constant across the entire length of the source contact. There is a small but non-zero difference, $V_c$, between the potentials at (1) and (2) due to the specific resistivity of the semiconductor $R_c = V_c/I_{SD}$.[80] As the value of this access resistance is very small, i.e., $R_c/R_{tot} \approx 10^{-2}$ in Fig. 2.3(c) (in particular due to the large carrier mobility chosen), the applied drain-source bias $V_{DS}$ drops essentially over the channel (2)-(3) (Fig. 2.2(c)) and $R_{channel} \approx V_{DS}/I_{SD}$. A further remarkable feature of the potential distribution within the semiconductor is found when closer inspecting the situation in Figs. 2.2(b,c) for $\Phi = 0$. Here, the potential between (1) and (2) slightly bulges upwards and induces a back-flow of injected carriers into the contact due to which the net injected current exactly matches $I_{SD}^{\mu}$. This net bulk-limited current is reminiscent of the space-charge limited current observed in organic diodes or OLEDs [111, 112].

We continue with resolving the total device current $I_{SD}$ with respect to the local *current density* contributions $J_{inj}(x)$ at the source-semiconductor interface (1')-(1) in Fig. 2.3(a) and the $I_{SD}$ contributions $I_{eff,th}$ and $I_{eff,tu}$ $I_{SD}$in Fig. 2.3(b).

In Fig. 2.3(a), the gray scale indicates the value of the logarithm of the current density at a given position $x$ of the contact-semiconductor interface between (1) and (1′) for different injection barriers $\Phi$. The additional contour lines mark the interval, beginning at $x = 0$, in which 50, 90, and 99 % of the current are injected. In the case of a vanishing barrier, $\Phi = 0$, the injected current crowds in an effective injection area [99] that comprises a region stretching out less than 0.5 $\mu$m away from the contact edge, i.e., from position (1) (located at $x$=0 in Fig. 2.3(a)) in the direction towards (1'). Due to the large amount of carriers that can be provided for $\Phi \approx 0$ eV, this small actively injecting stretch below the contact is sufficient to provide $I_{SD}^{\mu}$.

Upon increasing the barrier starting from $\Phi = 0$, $V_c$ only marginally increases, while the voltage drop across the channel between (2)-(3) slightly decreases (*cf.* curves $\Phi$= 0 and 0.2 eV in Fig. 2.2(c)).

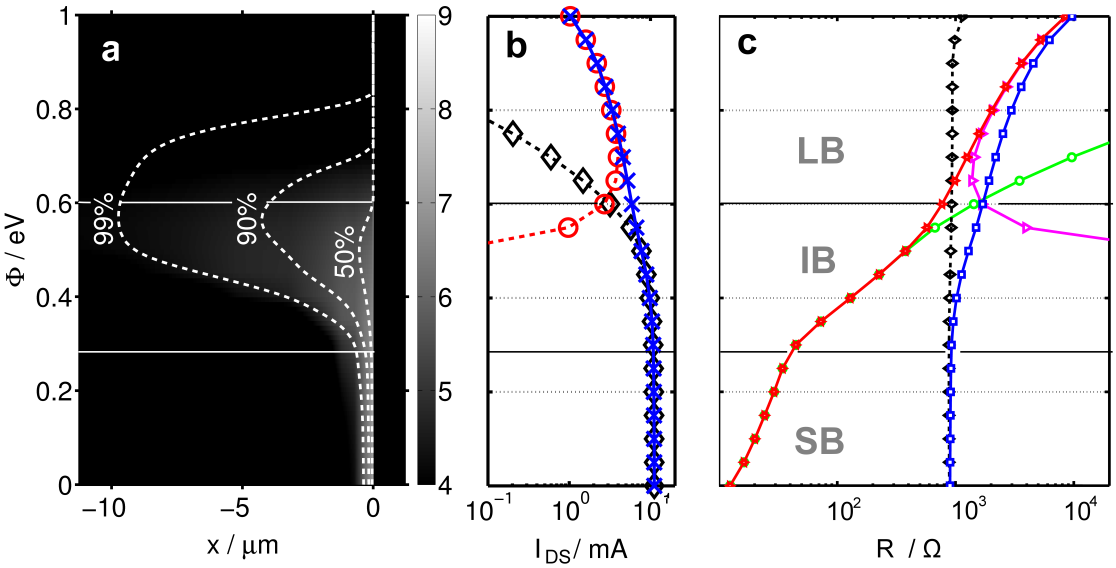


Figure 2.3: (a) Profile of the logarithm of the steady-state current density, lg $(J_{inj}(x)/\mathrm{Am}^{-2})$ in gray scale, below the source contact for a channel-length of $L = 5$ $\mu$m ($V_{\mathrm{DS}} =$ -10 V, $V_{\mathrm{GS}} =$ -40 V, $T = 300$ K) as a function of the position $x$ at the contact interface and the hole injection barrier $\Phi$. The contour lines mark the extension $x$ of the contact area, starting from x = 0 $\mu$m, in which 50, 90, and 99% of the current is injected. (b) Corresponding injected current $I_{\mathrm{SD}}$ (crosses), thermionic current $I_{th,eff}$ (diamonds), and effective tunnel current $I_{tu,eff}$ (circles) as function of $\Phi$. (c) Related total resistance $R_{\mathrm{tot}}$ (squares), contact resistance $R_{\mathrm{c}}$ (stars), $R_{\mathrm{c,th}}$ (circles), $R_{\mathrm{c,tu}}$ (triangles), and channel resistance $R_{\mathrm{channel}}$ (diamonds) as a function of the injection barrier height $\Phi$. The horizontal lines mark the transition between different injection regimes: (SB) Quasi-ohmic injection for small injection barriers; (IB) self-regulated thermionic injection for intermediate barriers; and (LB) tunnel-dominated injection for large barriers. The position of the (SB)-(IB) transition is determined by the pronounced kink in the $R_{\mathrm{c}}$ curve, while the (IB)-(LB) transition is determined by the intersection of the $R_{\mathrm{c,th}}$ and $R_{\mathrm{c,tu}}$ curves.

This can be ascribed to a self-regulated injection: While the thermionic

current overcoming the injection barrier somewhat decreases with increasing $\Phi$, the potential hump that is formed within the semiconducting layer between (1) and (2) (Fig. 2.2(c)) and, consequently, the back-flowing drift current becomes smaller; the hump eventually vanishes at $\Phi$ *ca.* 0.3 eV.

Due to an enlarged $V_c$, also $R_c$ steadily increases and almost triples its value between $\Phi = 0$ and 0.3 eV. However, as shown in Fig. 2.3(c), the influence of $R_c$ remains negligible with respect to $R_{channel}$ for injection barriers smaller than $\Phi = 0.3$ eV. Thus, following the definition for an ohmic contact by *Shen et al.* [111] and the terminology suggested by *Tessler* and *Roichman* [84], we identify the situation encountered for sufficiently small, but non-vanishing injection barriers as *quasi-ohmic injection*.

*The case of intermediate barriers (IB):*

The situation is more complex for barriers higher than $\Phi = 0.3$ eV. Fig. 2.3(c) reveals that the increase in $R_c$ is much more steep for barriers in the regions 0.3 - 0.6 eV than for barriers $\Phi < 0.3$ eV. The corresponding channel resistance $R_{channel}$ is, however, only marginally increasing with $\Phi$ (Fig. 2.3(c)). A first indication for a different injection scenario is that the potential distribution is now substantially different from the *SB*-case. As can be seen from the potential distribution associated to $\Phi = 0.47$ eV (Fig. 2.2(b)), the potential drop $V_c$ at $x = 0$ $\mu$m (white arrows), i.e., between (1) and (2) in Fig. 2.2(c), already amounts to 20% of the applied drain-source voltage $V_{DS}$. However, the potential is flat in the contact region far from the channel entrance, i.e., close to position (2') (black arrows in Fig. 2.2(b)). On approaching position (2) from (2'), there is an increasing *residual* voltage drop $V_c(x)$ between the source-semiconductor and semiconductor-dielectric interfaces. This voltage drop attains its maximum at (2) and ensures, that the carriers injected far from the channel are collected into the channel region. While still a significant portion of the current is injected into a small vicinity near (1), regions located at distances as remote as 8-9 $\mu m$ ($0.45 < \Phi < 0.7$ eV) from the channel region collectively contribute to the current (Fig. 2.3(a)).

The formerly encountered mechanism ensuring quasi-ohmic injection for small barriers is now replaced by an entirely different type of self-regulation.

For injection barriers $\Phi > 0.3$ eV, we encounter two processes [84]: (i) With increasing the injection barrier, the contact provides a smaller current density $J_{inj}$. Thus, the potential drop $V_c$ at the contact increases with $\Phi$. This larger drop $V_c$ is associated to an enhanced electric field at source-semiconductor interface that lowers the effective barrier height $\Phi^*$ (*cf.* Eq.(2.2)). (ii) The reduction of the effective barrier is accompanied by an expansion of the electrode area that participates in injection. The actively injecting area increases by one order of magnitude with respect to the $SB$-case. The size of the injection area is established such that sufficiently many carriers are collected to feed the bulk-limited current.[90] We will refer to this new type of self-regulation as *barrier-regulation* to distinguish this regime from the situation encountered for small barriers. Note that the drain contact is nevertheless always ohmic. The associated potential drop $\Psi(4) - \Psi(3)$ originates from the access resistance of the drain contact region. In accord with scanning potentiometry experiments [108, 113], this voltage is small due to the large semiconductor mobility.

It is important to realize at this point that the current $I_{SD}$ in the case of $\Phi$ = 0.47 eV is markedly, i.e., *ca.* 25 % lower than in the case of $\Phi$ =0.2 eV. As can be seen in Fig. 2.2(c), the value of $V_c$ at $\Phi = 0.47$ eV largely exceeds the minimal potential drop caused by the specific resistivity ($\Phi = 0$ eV). Thus, the presence of a marked $V_c$ translates into a significant reduction of the voltage available across the channel from $V_{DS}$ to $V_{channel} = V_{DS} - V_c$. Therefore, as illustrated in Fig. 2.3(c), the contact resistance $R_c$ increases with increasing barrier height due to an enlarged $V_c$ *and* due to a correspondingly reduced $I^{\mu}_{SD}$. As a consequence of the relationship $R_{channel} = (V_{DS} - V_c)/I_{SD}$, the negligible increase of $R_{channel}$ is determined by a decrease in the effective drain-source voltage $V_{DS} - V_c$ that is almost entirely compensated by a decrease in $I_{SD}$. Due to $V_c$, also the gate-source voltage being available to shape the carrier distribution in the channel region (2)-(3) is effectively lowered from $V_{GS}$ to $V_{GS} - V_c$ [84].

Due to self-regulation, contacts with injection barriers larger than $\approx$ 0.3 eV can provide bulk-limited current $I^{\mu}_{SD}$ via thermionic injection. This behavior recovers the definition of an ohmic contact as suggested by *Shen et al.*,

though they were having in mind organic diodes, i.e., laterally homogeneous injection.[111] Top contact OTFT relate to this concept of an "ohmic contact" quite differently than diodes. In OLEDs, an increase in the injection barrier would lead to a reduction of the injected current until an injection-limited current $< I^{\mu}_{\mathrm{SD}}$ is established; e.g., pentacene diodes formed with Pt contacts ($\Phi = 0.34$ eV) and Au contacts ($\Phi = 0.47$ eV) were shown to be profoundly contact-limited.[105] In contrast, OTFTs can sustain "ohmic contacts" for a wide range of barrier heights, because the required bulk-limited current $I^{\mu}_{\mathrm{SD}}$ is markedly *reduced* with *increasing* the injection barrier, as a considerable portion of $V_{\mathrm{DS}}$ is "lost" at the contact.

The comparison of the evolution of $R_{\mathrm{c}}$ and $R_{\mathrm{channel}}$ within this barrier-regulated injection regime Fig. 2.3(c) reveals that even for rather high barriers ($\Phi \approx 0.5$ eV) the total resistance $R_{\mathrm{tot}}$ is governed by $R_{\mathrm{channel}}$. Only at higher barriers the influence of $R_{\mathrm{c}}$ is no longer minor (around $\Phi \approx 0.6$ eV, $R_{\mathrm{c}} \approx R_{\mathrm{channel}}$). When assuming lower mobilities than in our present case, $R_{\mathrm{c}}$ remains of minor relevance even for higher barrier values.

The combination of the two injection mechanism discussed above suggests that self-regulation of $I^{\mu}_{\mathrm{SD}}$ is impeded, when the contact extension is significantly smaller than the above assumed 10 $\mu$m. However, the simulation of a device with a contact length of 400 nm reveals, that self-regulation is nevertheless present. In this case, the bulk-limited current $I^{\mu}_{\mathrm{SD}}$ is maintained solely by the adjustment of $\Phi^{*}$ through an increasing $V_{\mathrm{c}}$. Thus, within this barrier range $R_{\mathrm{c}}$ increases slightly steeper with barrier height as for 10 $\mu$m wide contacts. The corresponding curves $R_{\mathrm{c}}(\Phi)$ are shown in the Appendix. Thus, for narrow contacts, e.g., for structured Ag electrodes on pentacene [114], $R_{\mathrm{c}}$ may be become non-negligible with respect to $R_{\mathrm{channel}}$ at slightly lower barriers.

*The case of large barriers (LB):*

The evolution of the spatial spread of the injected current density $J_{inj}$ as a function of $\Phi$ as shown in Fig. 2.3(a) suggests that there is a third injection regime. The onset of this regime is characterized by the fact the contact area participating in injection starts shrinking again with increasing $\Phi$. This

reversal into a shrinking injection area marks the breakdown of self-regulated thermionic injection; in Fig. 2.3(a) it takes place at *ca.* 0.6 eV. This transition from the *intermediate* to the *large barrier* case is marked by the intersection of the curves for effective tunnel current and thermionic current (Fig. 2.3(b)). Accordingly, at this barrier also the relative contributions of the tunneling $R_{\mathrm{c,tu}}$ and the thermionic contribution $R_{\mathrm{c,th}}$ to the net $R_{\mathrm{c}}$ equal. The reason for tunneling becoming suddenly influential can be understood as follows: As demonstrated already in the *IB*-case, the potential drop $V_{\mathrm{c}}$ continues to rise with increasing $\Phi$ as a consequence of self-regulation. To locally supply as much injected current density as possible, the electric field associated to $V_{\mathrm{c}}$ counteracts the increase in $\Phi$ by reshaping the effective barrier $\Phi^{*}$. As illustrated in Fig. 2.2(b), potential difference across the contact region becomes substantial for a barrier as large as $\Phi = 0.8$ eV. Even though the electric field strength below the contact is considerably larger than in the *IB*-case, it is not sufficiently narrowing the barrier $\Phi^{*}$ to allow for tunneling injection along an extended area. It is the local field enhancement at the inner edge of the source contact, i.e., at position (1), due to which a further barrier lowering occurs at the corner. This lowering is sufficient to permit carriers to tunnel into the device. Therefore, the injection area is now strongly confined to the first few nm next to the contact edge (*cf.* Fig. 2.3(a)).

In this injection regime, the operation of the device is clearly contact-limited. In particular, the voltage loss at the contact exceeds the effective drain-source bias $V_{\mathrm{DS}} - V_{\mathrm{c}}$ (*cf.* Fig. 2.2(c)). If the source contact possessed a more "roundish" shape rather than being ideally planar with rectangular edges as assumed in our model, the local field-enhancements promoting tunneling would be absent and the critical barrier for the onset of the tunneling injection regime would be shifted to much larger values of $\Phi$.

Having established the distinct injection regimes exemplarily for a specific point of operation, we now turn to the entire output characteristics. In Fig. 2.4, simulated output characteristics $I_{\mathrm{SD}}(V_{\mathrm{DS}})$ are shown for the cases $\Phi = 0$, 0.2, 0.47, and 0.6 eV for various gate-voltages $V_{\mathrm{GS}}$. The corresponding evolution of the contact resistance $R_{\mathrm{c}}(V_{\mathrm{DS}})$ is shown in the Appendix.

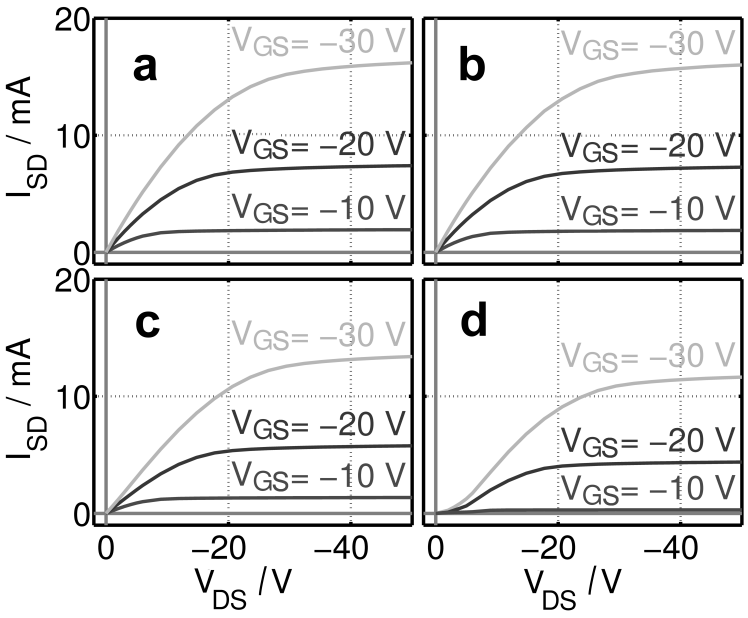


Figure 2.4: Simulated output characteristics $I_{\mathrm{SD}}(V_{\mathrm{DS}})$ for (a) $\Phi = 0$, (b) $\Phi = 0.2$ eV, (c) 0.47 eV, and (d) 0.6 eV at different gate-source voltages for a channel length $L_c = 5$ $\mu$m at $T = 300$ K.

For small injection barriers, i.e., for $\Phi = 0$ and 0.2 eV in Fig. 2.4(a,b), the corresponding output characteristics are indistinguishable. In the linear regime, $R_{\mathrm{c}}$ is small (*cf.* Fig. 2 in the Appendix) and negligible in comparison to the channel resistance $R_{\mathrm{channel}}$ when $|V_{\mathrm{DS}}|$ exceeds a few volts. Only for source-drain biases $|V_{\mathrm{DS}}|$ smaller than two volts, $R_{\mathrm{c}}$ is small but not necessarily negligible.[115] For higher barriers, *e.g.,* for $\Phi = 0.47$ and 0.6 eV in Fig. 2.4(c,d), the drain current $I_{\mathrm{SD}}$ lowers with increasing barrier in accord with the behavior depicted in Fig. 2.3(b). This reduction is also well seen in the saturation regime ($|V_{\mathrm{GS}}| << |V_{\mathrm{DS}}|$), e.g., when comparing the currents $I_{\mathrm{SD}}$ at $V_{\mathrm{DS}}$ = -50 V in Fig. 2.4. Note, that the current value $I_{\mathrm{SD}}$ at a given point of operation in the saturation regime is, of course, independent of the drain-source voltage $V_{\mathrm{DS}}$ and thus not susceptive to a bias reduction $V_{\mathrm{DS}} - V_{\mathrm{c}}$. However, $V_{\mathrm{c}}$ still plays a decisive role in determining the current $I_{\mathrm{SD}}$ passing the device. This can be understood as follows: As the gate potential is located between the source and the drain potential, [70] there exists a posi-

tion in the channel region between (2) and (3) in Fig. 2.1(a), at which the electrostatic potential $\Psi$ coincides with $V_{\mathrm{GS}}$ (*pinch-off*); the distribution of $\Psi$ across the device alongside with the indication of the *pinch-off* position are shown in the Appendix. At this *pinch-off* position, there is no electric field available to form a channel, i.e., a field that is able to strongly enhance the concentration of mobile carriers at the semiconductor-dielectric interface with respect to semiconductor bulk. Thus, the carrier concentration between (2) and the *pinch-off* position is much higher than that between the *pinch-off* point and (3). As a result, the channel is effectively reduced to the region between (2) and the *pinch-off* point. Moreover, the current flow through this reduced channel is associated to the external bias $V_{\mathrm{GS}}$ rather than $V_{\mathrm{DS}}$,[70] as expressed by the relationship $I_{\mathrm{SD}} \propto \mu/L(V_{\mathrm{GS}} - V_{\mathrm{th}})^2$.[116] This external bias must be split between the contact resistance and the channel resistance. Thus, the *effective* bias available for the reduced channel is $V_{\mathrm{GS}} - V_{\mathrm{c}}$ (as opposed to $V_{\mathrm{DS}} - V_{\mathrm{c}}$ in the linear regime). For illustrative purposes we show also the voltage drops along the current pathway (1)-(2)-(3)-(4) for the saturation regime in the Appendix.

A second manifestation of the contact resistance is the non-linear increase of $I_{\mathrm{SD}}(V_{\mathrm{DS}})$ at low drain-source voltages for $\Phi = 0.6$ eV (Fig. 2.4(d)). In this section of the curve, i.e., in the linear regime, the current is determined by the potential drop $V_{\mathrm{DS}}$ between source and drain electrode. For such large barrier heights, the contact resistance $R_{\mathrm{c}} \approx R_{\mathrm{channel}}$ (*vide infra*) reduces the effectively available $V_{\mathrm{DS,eff}}$ by almost a factor of two (Fig. 2.2(c)) and gives, thus, rise to a delayed onset of the current flow.[117] Such a delay is the fingerprint of contact-limited operation, and can be immediately identified in experiments, in particular, if the output characteristics could be compared to devices identical in geometry in which the injection barrier height was successfully decreased upon manipulating the contact interface.[72, 88, 114, 118]

### 2.5.2 Temperature dependence of the contact resistance

Our above findings indicate that there is a barrier-determined transition between three distinct injection regimes. Now we turn our discussion to the temperature dependence of the contact resistance. A routine to extract the charge carrier mobility in the semiconductor relies on temperature-dependent measurements of the transfer and output characteristics [73, 74, 96, 109, 119]. It is, thus, vital to be able to distinguish the temperature-dependence of the transport in the bulk semiconductor from temperature-dependent injection at the contact interface. [73, 74, 96, 109, 119] *Pesavento et al.* found in their experiments with pentacene OTFTs with Au contacts a marked dependence of the mobility $\mu$ and $R_\mathrm{c}$ on temperature.[73] The authors interpret the increase in $R_\mathrm{c}$ with inverse $T$ as temperature-activated behavior in analogy to the temperature activated mobility $\mu$. Upon analyzing the correlation between $\mu(T)$ and $R_\mathrm{c}(T)$, the authors argue that there is a transition between two different injection mechanisms near room temperature. To investigate such findings in more detail and to elucidate the influence of temperature on the injection mechanism, we proceed as follows: The injection barrier height is now fixed at $\Phi$=0.47 eV in correspondence to the published value of the Au-pentacene hole injection barrier [104]. Furthermore, we will consider two cases to discriminate between the temperature influence on the injection across a barrier and the influence on carrier transport. At first, the *artificial case* is considered in which the parameter temperature solely controls the injected current density via Eqs. (2.3) and (2.8), while the carrier mobility in the semiconducting layer is left unaffected. The mobility value as high as $\mu_0 = 1$ cm$^2$/Vs will ensure that the channel resistance is not masking possible effects in $R_\mathrm{c}$. In a second case, both temperature-dependent injection and activated transport is permitted. We first turn to the evolution of the total resistance $R_\mathrm{tot}$, the contact resistance $R_\mathrm{c}$, and its two contributions $R_\mathrm{c,th}$ and $R_\mathrm{c,tu}$ as a function of temperature for $E_A = 0$ meV, shown in Fig. 2.5(a). In the case of the contact resistance $R_\mathrm{c}$ (stars), there is a marked transition from a strong rise (denoted as region (I) in Fig. 2.5(a)) into a saturation to a constant value (region (II)) at *ca.* 230 K. In full analogy to

the barrier-dependence of $R_{\mathrm{c}}$, these temperature regions are associated to different injection regimes.

The spatial injection profile below the source electrode, being illustrated in Fig. 2.6(a), reveals the transition from a barrier-regulated thermionic (*IB*-case) to a tunneling injection (*LB*-case). Thus, the initial increase of $R_{\mathrm{c}}$ for temperatures $T$ lowered from 400 $K$ to 200 $K$ originates from the rapid increase of $R_{\mathrm{c,th}}$ (circles) that arises from an injected current density being reduced with decreasing temperature as less holes can overcome the barrier $\Phi^{\star}$ mainly due to a reduced width of the Fermi-Dirac distribution (*cf.* exponential factor in Eq. (2.3)). This decrease in $J_{inj}$ is only partially compensated by a rapidly enlarging injection area. In region (II), injection is limited to tunneling, since the thermionic injection current $I_{eff,th}$ rapidly decreases with further lowering $T$ (diamonds in Fig. 2.6(b)). Thus, $R_{\mathrm{c,tu}}$ (Fig. 2.5(a), triangles) fully determines the evolution of the net contact resistance $R_{\mathrm{c}}$. Since the tunnelling injection current cannot be explicitly controlled by temperature (*cf.* Eq. (2.4)), $V_{\mathrm{c}}$ is constant and, thus, $R_{\mathrm{channel}}$ and $R_{\mathrm{c}}$ become independent of temperature.

Now we turn to the discussion of the situation in which we consider temperature-activated hole transport in the channel region as well as in the contact region, i.e., $E_A > 0$ meV. Again, we plot the temperature-dependence of the total resistance $R_{\mathrm{tot}}$, the contact resistance $R_{\mathrm{c}}$, and its relative contributions $R_{\mathrm{c,th}}$ and $R_{\mathrm{c,tu}}$ in Fig. 2.5(b) for an activation energy of $E_A = 10$ meV. Moreover, we additionally show the spatially resolved injected current density in Fig. 2.6(c) and the integrated currents $I_{\mathrm{SD}}$, $I_{eff,th}$, and $I_{eff,tu}$ as a function of temperature in Fig. 2.6(d).

There are two main differences to the non-activated case: Firstly, $R_{\mathrm{c}}$ (Fig. 2.5(b)) is now increasing and $I_{\mathrm{SD}}$ is decreasing with inverse temperature in the low temperature region (Fig. 2.6(d)), while the injection profile is highly reminiscent of the $E_A = 0$ meV case (Fig. 2.6(a,c)). Secondly, allowing for $E_A > 0$ results in the shift of the transition between regions (I) and (II) towards a smaller temperature. The kink corresponding to this transition in the temperature-dependent $R_{\mathrm{c}}$ has been found also experimentally.[73]

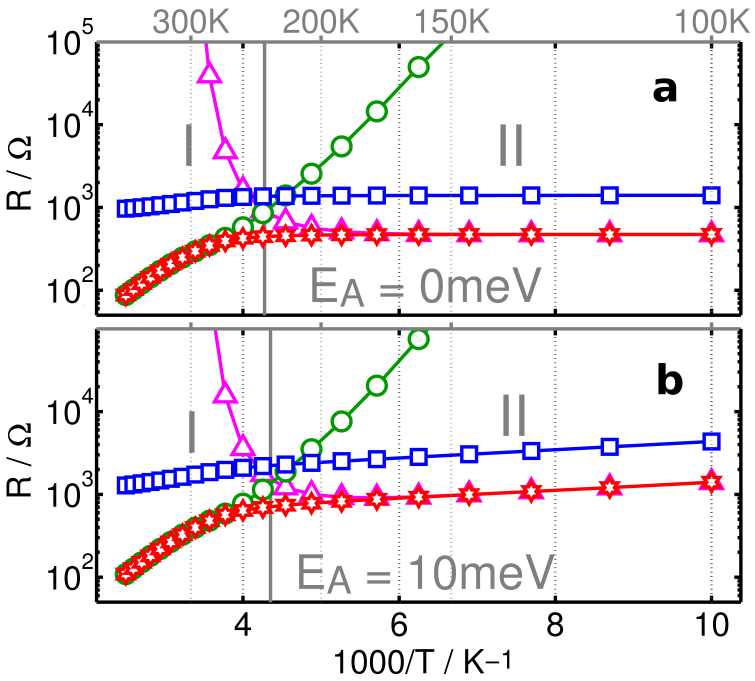


Figure 2.5: Simulated total resistance $R_{\mathrm{tot}}$ (squares) and contact resistances $R_{\mathrm{c}}$ (stars), $R_{\mathrm{c,th}}$ (circles), $R_{\mathrm{c,tu}}$ (triangles) as a function of temperature at $V_{\mathrm{DS}}$ = -10 V and $V_{\mathrm{GS}}$ = -40 V for a channel-length $L = 5\ \mu m$. Shown is the evolution (a) when artificially assuming a temperature independent mobility ($E_A = 0$ meV) and (b) with a temperature activated mobility ($E_A = 10$ meV). Regions I and II distinguish temperatures at which injection is either dominated by thermionic emission or tunneling injection; the transition temperature is marked by a gray vertical line and corresponds to the intersection position of the $R_{\mathrm{c,tu}}$ and $R_{\mathrm{c,th}}$ curves.

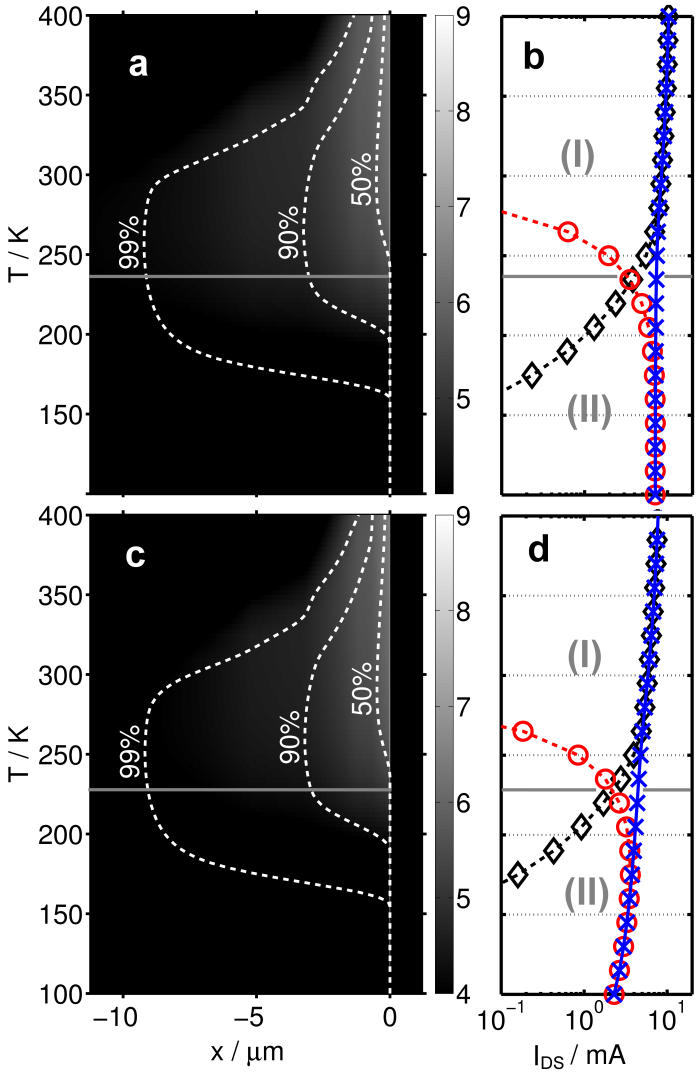


Figure 2.6: Steady-state current density profile, lg $(J_{inj}(x)/\mathrm{Am}^{-2})$, in gray scale, along the source contact (Fig. 2.1(a)) as a function of temperature for a channel-length of 5 $\mu\ m$ ($V_{\mathrm{DS}}$ = -10 V, $V_{\mathrm{GS}}$ = -40 V, $\Phi$ = 0.47 eV) (a) without activation energy ($E_A$ = 0 meV) and (c) with temperature activated transport ($E_A$ = 10 meV). (b,d) Integrated device current $I_{\mathrm{SD}}$ (crosses) and its contributions due to thermionic emission $I_{eff,th}$ (diamonds) and tunneling $I_{eff,tu}$ (circles) for $E_A$ = 0 and $E_A$ = 10 meV, respectively. The transition temperature between thermionic and tunneling injection is marked by a gray horizonal line whose position is determined by the intersection of the effective tunnel current $I_{eff,tu}$ and the thermionic current $I_{eff,th}$ curves.

The essential difference to the previous case $E_A = 0$ meV originates from the fact that the channel resistance $R_{\text{channel}}$ is now also temperature-dependent due to a carrier mobility $\mu(T)$ (Eq. 2.9). $R_{\text{c}}$ and $R_{\text{channel}}$ strongly depend on each other, since they are two resistances in series that share the same $I_{\text{SD}}$ and divide the external bias $V_{\text{DS}}$. For a fixed temperature, the net current $I_{\text{SD}}$ is markedly smaller than $I_{\text{SD}}(E_A = 0)$ due to a reduced carrier mobility (*cf.* Fig. 2.6(b,d)). Since the source electrode needs to provide less current due to a lowered $\mu(T)$, a larger effective injection barrier $\Phi^*$ is established (*cf.* Eq. (2.3)). Consequently, the barrier-shaping field $E_\perp \propto V_{\text{c}}$ and the potential drop $V_{\text{c}}$ at the electrode are lowered. In region (I), in which thermionic injection prevails, $I_{\text{SD}} = I_{eff,th}$ reduces more rapidly with decreasing $T$ than $V_{\text{c}}$ due to exponential factor $\exp(const. * V_{\text{c}}^{1/2}/T)$ in Eq. (2.3). Thus, $R_{\text{c}} = V_{\text{c}}/I_{\text{SD}}$ drops more steeply with $T$ than in the $E_A = 0$ case (Fig. 2.5(a,b)). In the tunneling-dominated injection region (II), Fig. 2.5(b) reveals a $R_{\text{c}}$ that markedly *increases* with decreasing $T$. This behavior is found also in experiments.[73, 82] The implicit relationship between $R_{\text{c}}$ and $T$ is a consequence of the reduction of the current $I_{\text{SD}}$; a rationale for the resulting exponential rise of $R_{\text{c,tu}}$ with inverse $T$ is given in the Appendix. Note that $R_{\text{c,tu}}$ has to rise with increasing inverse temperature in region (II) due to a hopping transport mobility $\mu$ that always decreases with increasing temperature.

### 2.5.3 Transmission/transfer line method revisited

To date, the transmission/transfer line method (TLM) is the most widespread method to determine $R_{\text{c}}$ experimentally. It relies on a series of OTFTs varying solely in their channel length $L$[120] and evaluates the output curves of this series of devices by essentially following the work of *Luan* and *Neudeck*[121]. The method exploits the fact that the total resistance $R_{\text{tot}}(L)$ varies linearly with the channel length $L$ provided that (i) ohmic contacts are present and (ii) $R_{\text{c}}$ is independent of $L$, i.e., that the variation in $R_{\text{tot}}(L)$ is solely caused by the channel resistance [69, 121, 122]. Then, the contact resistance $R_{\text{c}}$ can be ascribed to the linearly extrapolated value

$R_{\mathrm{tot}}(L = 0)$. For top-contact- and bottom-contact-bottom-gate OTFTs the underlying assumptions of the TLM method hold strictly only for injection barriers associated to quasi-ohmic injection.

However, often a linear relationship $R_{\mathrm{tot}}(L)$ alongside with output curves $I_{\mathrm{SD}}$ being strictly linear in $V_{\mathrm{DS}}$ for each $L$ are considered as sufficient conditions for the applicability of TLM, rather than carefully ensuring that the above-made preconditions are met. In the case of top-contact OTFTs one has to be careful, as different injection scenarios exist that provide bulk-limited current. For injection barriers that give rise to quasi-ohmic or barrier-regulated thermionic injection (i.e., the *SB*- and *IB*-case), injection can be classified as ohmic (*vide infra*), i.e., $I_{\mathrm{SD}}$ is found to rise linearly with $V_{\mathrm{DS}}$ in the far-linear regime. A handy experimental procedure to discriminate this ohmic from non-linear injection has been suggested by *Hamadani et al.*[109] However, as soon as barrier-regulated injection occurs, the value of $R_{\mathrm{c}}$ depends implicitly on the channel length $L$. This can be readily understood upon recalling that $R_{\mathrm{c}}$ and $R_{\mathrm{channel}}$ are two resistances in series that share a common current $I_{\mathrm{SD}}$ and divide the external bias $V_{\mathrm{DS}}$ (*cf.* Fig. 2.1(b)).

Both the contact voltage $V_{\mathrm{c}}$ as well as the device current $I_{\mathrm{SD}}$ depend on $L$: (i) For given fixed external bias $V_{\mathrm{DS}}$, an increase in $R_{\mathrm{channel}}$ due to an enlarged $L$ relates to a larger fraction $V_{\mathrm{DS}} - V_{\mathrm{c}}$ of $V_{\mathrm{DS}}$ dropping across the channel region. Thus, the fraction $V_{\mathrm{c}}$ dropping at the contact becomes smaller. (ii) At the same time, the source electrode provides less current $I_{\mathrm{SD}}$ due to a larger effective injection barrier $\Phi^*$ (*cf.* Eq. (2.3)). The channel resistance $R_{\mathrm{channel}}$ and, thus, the total resistance $R_{\mathrm{tot}}$ increase with $L$. When assuming a fixed drain-source bias $V_{\mathrm{DS}}$, the bulk-limited current $I^{\mu}_{\mathrm{SD}}$ decreases with increasing $L$; thus, the contact has to inject less current. As explained for the $IB$-case, a lessened current demand leads to a reduced voltage $V_{\mathrm{c}}$ droping at the contact and, consequently, to a dependence of $R_{\mathrm{c}}$ on $L$.

It is, thus, interesting to quantitatively access the impact of the violated assumption (i.e., $R_{\mathrm{c}} \neq R_{\mathrm{c}}(L)$) on the TLM-deduced value of $R_{\mathrm{c,TLM}}$ for staggered OTFTs. We compare in Fig. 2.7 the directly simulated $R_{\mathrm{c}}$ and the total resistance $R_{\mathrm{tot}}$ with $\mathrm{R_{c,TLM}}$ as a function of the channel length $L$ for the barrier $\Phi = 0.47$ eV.

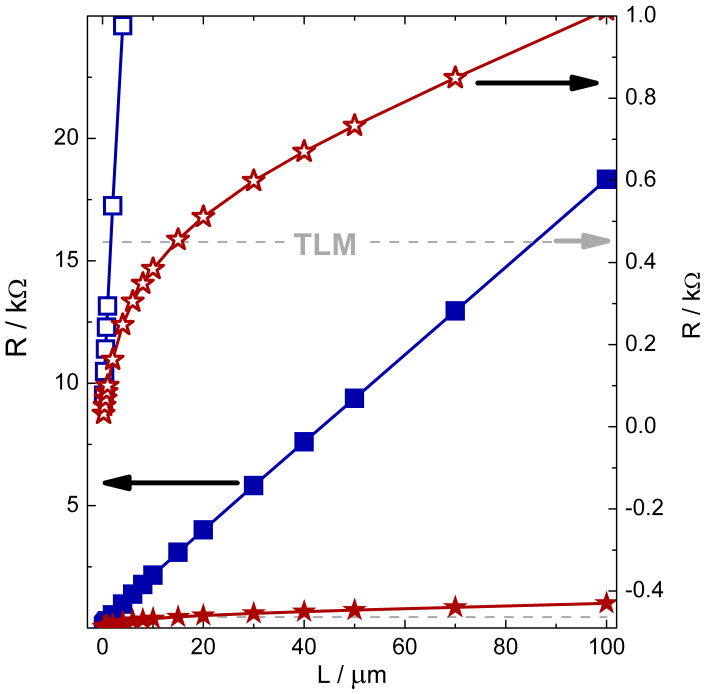


Figure 2.7: Dependence of the total $R_{\mathrm{tot}}$ (square) and contact $R_{\mathrm{c}}$ (star) resistance on the channel-length $L$ at $V_{\mathrm{DS}} = -10\ V$ and $V_{\mathrm{GS}} = -40\ V$, $\Phi = 0.47$ eV and T = 300 K. $R_{c,\mathrm{TLM}}$ (horizontal dashed line) is the resistance obtained by using the transfer-line method for channel-lengths $L \geq 30\ \mu m$. The curves with closed symbols relate to the entire data range indicated with the left axis, while curves related to the right axis (open symbols) correspond to a close-up view (stretching factor 20) to illustrate the nonlinear dependence $R_{\mathrm{c}}(L)$ for $L < 30\ \mu m$.

The contact resistance $R_{\mathrm{c}}$ (closed stars) obviously differs from the value of $\mathrm{R}_{\mathrm{c,TLM}}$. For small $L \leq 30 \mu m$, the non-linear increase of $R_{\mathrm{c}}$ in $L$ causes a marked non-linear dependence of $R_{\mathrm{tot}}$ on $L$. This is not surprising, as for such $L$ the value of $R_{\mathrm{c}}$ is in the same order of magnitude as the value of the channel resistance $R_{\mathrm{channel}}$ (*cf.* Fig. 2.3(c)). Even more remarkably, we observe a nearly linear rise of $\mathrm{R}_{\mathrm{tot}}(L)$ above channel-lengths of 30 $\mu m$. This is consistent with the perception from experiment [68, 80, 81, 86, 88, 90, 95, 114, 119]. However, the contact resistance $\mathrm{R}_{\mathrm{c}}$ grows linearly in $L$ rather than

being constant ; a rationale for this behaviour is given in the Appendix. It is, therefore, this fortuitous superposition of a linear $R_{\mathrm{c}}(L)$ and $R_{\mathrm{channel}}(L)$ that leads to the perception of an overall linearly dependent $R_{\mathrm{tot}}(L)$. The latter, in turn, may wrongly imply that $R_{\mathrm{c}}$ is $L$-independent. The neglect of this dependence misestimates the value of $R_{\mathrm{c}}$; for our chosen material and geometry parameters, the relative error amounts to 120% at $L = 100$ $\mu$m.

## 2.6 Conclusion

We examined the hole injection into top-contact bottom-gate organic thin-film transistors with respect to the relation between injection barrier and the contact resistance $R_{\mathrm{c}}$. To that aim, a simulation tool based on a two-dimensional drift-diffusion model was developed that is capable of (i) self-consistently describing field and temperature dependence of the injected current, (ii) incorporating thermionic and tunneling injection, and (iii) subsequent carrier transport in the device as a function of the electrode arrangement. To determine the values of contact and channel resistances, we analyzed the steady-state potentials and the device current with the help of a simple equivalent circuit model.

The staggered arrangement of the electrodes is shown to tremendeously influence the way injection occurs into the device. The influence of $R_{\mathrm{c}}$ remains minor with respect to the channel resistance for several tenth of meV even if conditions are assumed that are expected to promote contact limitations, i.e., small channel resistances due to high carrier mobilities and small channel lengths.

This lack of contact influence is observed for two distinct, barrier-dependent injection regimes that both rely on thermionic injection. For low barriers, quasi-ohmic injection is observed. In principle, the contact can provide more carriers than required to establish bulk-limited current $I^{\mu}_{\mathrm{SD}}$. Due to the establishment of a space charge region below the contact and a marked current crowding, injection of excess carriers is suppressed and $I^{\mu}_{\mathrm{SD}}$ is exactly matched. In this regime, the contact resistance is much smaller than the

channel resistance (*cf.* Fig. 2.3(c)). For barriers of intermediate height, the contact would provide an insufficient amount of *carriers per unit area* to match $I^{\mu}_{\mathrm{SD}}$. This is circumvented by (i) an effectively lowered barrier height due to an enlarged local field being associated to an enlarged potential drop $V_{\mathrm{c}}$ at the contact and (ii) an order of magnitude increase in the injection area. Due to the first factor contributing to regulation, $R_{\mathrm{c}}$ is strongly increasing with the injection barrier. Thus, there is a barrier above which the value of $R_{\mathrm{c}}$ approaches $R_{\mathrm{channel}}$ and the operation becomes contact limited. However, this barrier is larger than that corresponding to the onset of *barrier regulation*. For even larger barriers, thermionic emission is entirely replaced by tunneling injection. The transition to tunneling injection is expected to occur at earliest at the (sharp) edge of the source contact due to a local field enhancement.

In terms of temperature dependence of $R_{\mathrm{c}}$, the above-mentioned three major injection regimes can be recovered. However, the interdependence of $R_{\mathrm{c}}$ and $T$ is much more involved than $R_{\mathrm{c}}(\Phi)$, since also the channel resistance $R_{\mathrm{channel}}$ is strongly temperature-dependent. The latter is the origin of the marked $T$-dependence of $R_{\mathrm{c}}$ even if injection is limited to tunneling, i.e., the injected current is not explicitly $T$-dependent. For OTFTs with common material combinations, such a transition from barrier-regulated thermionic to tunneling injection might be easily encountered in $T$-dependent measurements if temperatures varying between 300 K and $\leq$ 250 K are probed. Then, the correct consideration of the interplay between $R_{\mathrm{c}}$ and $R_{\mathrm{channel}}$ is required to reliably extract the $\mu(T)$ relation.

We further highlight that the transmission line method fails to provide quantitative $R_{\mathrm{c}}$ values for barriers related to the barrier-regulated, i.e., *non-ohmic* injection regime. This failure is caused by the commonly implied assumption that $R_{\mathrm{c}}$ is independent of the channel length $L$. In reality, however, $R_{\mathrm{c}}$ exhibits a profound, nearly linear dependence on $L$. In combination with the anticipated linear relationship between $R_{\mathrm{channel}}$ and $L$, an overall linear increase in $R_{\mathrm{tot}}$ is established which is, in turn, wrongly interpreted to originate solely from $R_{\mathrm{channel}}$. Thus, TLM is, strictly speaking, not applicable to obtain $R_{\mathrm{c}}$ for such injection barriers. The value of the apparent $\mathrm{R_{c,TLM}}$ is

expected to be in the same order of magnitude as the true value, however, the deviation may exceed 200%. Gold on pentacene, being currently a fruit-fly contact interface for OTFTs, forms a hole injection barrier which is due to the large hole mobility in pentacene a likely candidate for the failure of TLM.

## Acknowledgment

The authors gratefully acknowledge T. Obermüller and S. Ausserlechner for fruitful and in-depth discussions. This work has been supported by the Austrian Nanoinitiative (FFG) through the NILsimtos project as part of the NILaustria cluster.

## 2.7 Appendix

### 2.7.1 Confined Contacts in Top-Contact OTFTs

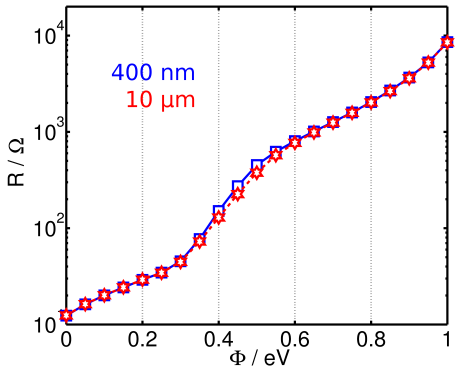


Figure 2.8: Barrier dependence of the contact resistance $R_c$ for a contact width of 10 $\mu m$ and 400 nm. A strongly decreased contact extension leads only to a slightly increased $R_c$. Apparently, the lack of the possibility to increase the injection area is compensated by further enhancing the voltage drop $V_c$ at the contact.

### 2.7.2 Contact resistance for different points of operation

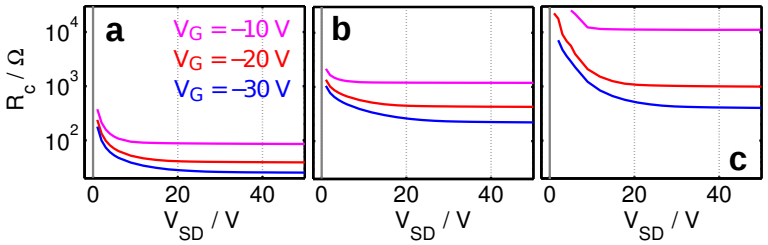


Figure 2.9: Simulated contact resistances $R_c(V_{DS})$ for (a) $\Phi = 0.2$ eV, (b) 0.47 eV, and (c) 0.6 eV at different gate-source voltages $V_G$ for a channel length $L_c = 5$ $\mu$m at $T = 300$ K.

### 2.7.3 Steady-state potential distribution in the saturation regime

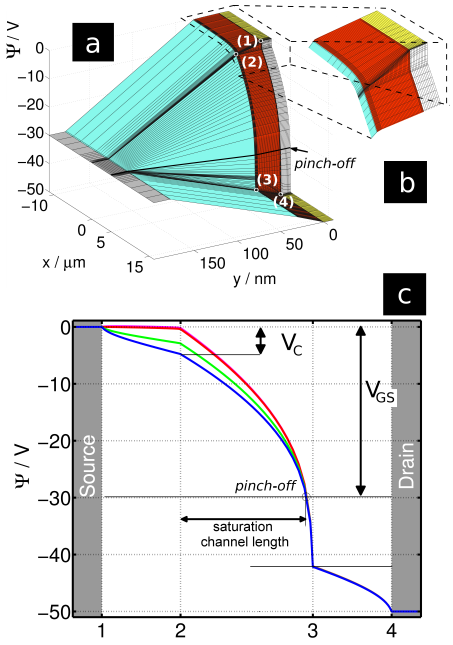


Figure 2.10: (a) Steady state potential distribution $\Psi$ of a top-contact bottom-gate organic thin film transistor in the saturation regime at $V_{\mathrm{DS}} = -50\ V$ and $V_{\mathrm{GS}} = -30\ V$ for a channel length $L_c = 5\ \mu$m at $T = 300$ K. The arrow marks the pinch-off point, i.e., the position within the channel region at which $\Psi = V_{\mathrm{GS}}$. (b) Close up view of the steady state potential in the region of the injecting contact. The determination of the potential in the vicinity of the contacts including the layer of air between the contacts is vital to reliably predict the barrier-shaping electric field. (c) Potential along the current pathway (1)-(2)-(3)-(4) at this point of operation for injection barrier heights $\Phi = 0$, 0.2, 0.47, and 0.6 eV.

### 2.7.4 Interdependence of $R_{\mathrm{c}}$ and $R_{\mathrm{channel}}$

In the linear regime, it is possible to extract an analytical relationship between $R_{\mathrm{c}}$ and $R_{\mathrm{channel}}$ starting from the dependence of $I_{\mathrm{SD}}$ on the external

biases: [116]

$$I_{\mathrm{SD}} = \frac{\mu C W}{L}\left[(V_{\mathrm{DS}} - V_{\mathrm{c}})(V_{\mathrm{GS}} - V_{\mathrm{c}}) - \frac{1}{2}(V_{\mathrm{DS}} - V_{\mathrm{c}})^2\right].$$

Therein, $C$ denotes the capacitance of the dielectric layer. By introducing the channel resistance $R_{\mathrm{channel}} = (V_{\mathrm{DS}} - V_{\mathrm{c}})/I_{\mathrm{SD}}$, $V_{\mathrm{c}}$ can be expressed as:

$$V_{\mathrm{c}} = -2\left(\frac{L}{\mu C W R_{\mathrm{channel}}} + \frac{V_{\mathrm{DS}}}{2} - V_{\mathrm{GS}}\right).$$

Assuming that the contact resistance $R_{\mathrm{c}}$ is much smaller than the channel resistance $R_{\mathrm{channel}}$, the identity

$$I_{\mathrm{SD}} = \frac{V_{\mathrm{DS}} - R_{\mathrm{c}} I_{\mathrm{SD}}}{R_{\mathrm{channel}}}$$

reduces to $I_{\mathrm{SD}} \approx V_{\mathrm{DS}}/R_{\mathrm{channel}}$. Then, $R_{\mathrm{c}} = V_{\mathrm{c}}/I_{\mathrm{SD}}$ becomes

$$R_{\mathrm{c}} = \left[\frac{2V_{\mathrm{GS}}}{V_{\mathrm{DS}}} - 1\right] R_{\mathrm{channel}} - \frac{2L}{\mu C W V_{\mathrm{DS}}} \quad . \tag{A.1}$$

Relationship (A.1) is strictly valid only (i) if quasi-ohmic injection is present or (ii) $R_{\mathrm{channel}}$ is sufficiently large due to a low mobility $\mu$ or due to a large channel length $L$.

Whenever the relation between $R_{\mathrm{channel}}$ and an external parameter is known, be that with respect to the temperature $T$ or to the channel length $L$, the above expression yields the corresponding dependence of $R_{\mathrm{c}}$:

($T$) At low $T$, $R_{\mathrm{channel}}$ can be expected to be much larger than $R_{\mathrm{c}}$ due to the markedly reduced $\mu$. $R_{\mathrm{channel}}$ is proportional to $\exp(D/T)$ due to the temperature-activated mobility $\mu(T) \propto \exp(-D/T)$ and $I_{\mathrm{SD}} \propto \mu(T)$. Thus, $lgR_{\mathrm{c}}$ depends linearly on the inverse $T$ temperature, *i.e.* $lgR_{\mathrm{c}}$ has the form $lgR_{\mathrm{c}} = A/T + B$; therein, $A, B$ and $D$ are temperature-independent constants.

($L$) If $R_{\mathrm{channel}}$ is linearly dependent on the channel length $L$, i.e., $R_{\mathrm{channel}} = AL + B$, also $R_{\mathrm{c}}$ adopts a linear relationship $R_{\mathrm{channel}} = DL + B$ ($A, B$ and $D$ are $L$-independent constants). Hence, a linear relationship of $R_{\mathrm{channel}}(L)$ gives rise to a linear dependence of $R_{\mathrm{c}}$ *and* of $R_{\mathrm{tot}}$ if $R_{\mathrm{c}} \ll R_{\mathrm{channel}}$ due to large $L$.

# Chapter 3

# Surface Proton Transfer Doping

## 3.1 Preamble

This chapter is published in Physica Status Solidi (a) [7] by S. J. Ausserlechner, M. Gruber, R. Hetzel, H. G. Flesch, L. Ladinig, L. Hauser, A. Haase, M. Buchner, R. Resel, F. Schürrer, B. Stadlober, G. Trimmel, K. Zojer and E. Zojer.

In this work, I performed the drift-diffusion based simulations to describe the threshold-voltage shift and the formation of a hysteris depending on the thickness of the dielectric layer.

## 3.2 Abstract

A number of studies show that chemical modification of the semiconductor-dielectric interface can be used to control the threshold voltage ($V_{th}$) of organic thin film transistors (OTFTs). A promising chemical functionality to achieve that are acidic groups, which - at the semiconductor-dielectric interface - have been used to realize chemically responsive OTFTs and easy to fabricate inverter structures. Especially for pentacene-based OTFTs, the underlying chemical and physical mechanisms behind the acid-induced $V_{th}$ shifts are not yet fully understood. Their clarification is the topic of the present paper.

To distinguish between space-charge and dipole-induced effects, we study the impact of the thickness of the gate oxide on the device characteristics achieving maximum $V_{th}$ shifts around 100 V. To elucidate the role of the acid, we compare the doping of pentacene by acidic interfacial layers with the impact of hydrochloric acid vapour and investigate the consequences of exposing devices to ammonia. Complementary experiments using 6,13-bis(triisopropylsilylethynyl)pentacene as active layer hint towards the central (6 and 13) carbon atoms being subject to the electrophilic attack by the acidic protons. They also prove that the observed $V_{th}$ shifts in pentacene devices are indeed a consequence of the interaction between the acidic groups and the active material. The experimental device characterization is supported by drift-diffusion based device modelling, by quantum chemically simulations, as well as by contact angle, atomic force microscopy and x-ray reflectivity. The combination of the obtained results leads us to suggest proton transfer doping at the semiconductor-dielectric interface as the process responsible for the observed shift of $V_{th}$.

## 3.3 Introduction

The crucial role played by the semiconductor-dielectric interface has been demonstrated by a number of studies during the past few years [123, 124]. It, for example, influences charge-carrier trapping [125] and thin film growth [126]. This, in turn, determines device parameters like the carrier mobility ($\mu$) [127, 128, 129] and the threshold voltage ($V_{th}$). From an application-oriented point of view, the control of $V_{th}$ is necessary to realize low voltage operation organic electronics [130, 131], or to fabricate depletion-load inverters using only a single-type of semiconductor material [132, 133]. Beyond that, understanding processes affecting $V_{th}$ is also of fundamental interest for understanding the operation mechanism of OTFTs.

The methods developed over the years to tune $V_{th}$ via interface modifications include: UV [132], UV-ozone [134, 135], or oxygen plasma [135] treatment of the surface of the dielectric, changing the dielectric capacitance

[136], inserting dipole-polarized [137] or polarizable layers [138, 139], or storing charges at the dielectric-semiconductor interface [140]. Of particular relevance for the present study is the use of functional self-assembled monolayers (SAMs) [141, 142, 143, 144, 145]. Their insertion between the gate dielectric and the organic semiconductor layer has been shown to give rise to $V_{th}$ shifts of several ten volts. A number of underlying mechanisms for the shifts have been suggested. One is the formation of dipole layers when using polar SAMs that shift the potential of the semiconductor-dielectric interface [141, 142, 143, 145], where the charge carrier transport takes place [146]. The experimentally observed $V_{th}$ shifts did, however, not necessarily match the expectations based on the 'dipole' model [141, 144]. Moreover, it was argued on the basis of a comparison between device characteristics and secondary electron emission spectroscopy experimentscite[129] that realistic molecular dipole moments would lead to $V_{th}$ shifts of only a few volts. This notion has been supported by drift-diffusion based simulations [147].

Thus, a charge transfer between the organic semiconductor and the SAM has been suggested as an alternative explanation [141, 144]. This process is reminiscent of 'electronic' surface transfer doping [148, 149, 150, 151, 152], where the underlying chemical process is a redox reaction between the semiconductor and the SAM [148]. The model is based on the assumption that semiconductor-dielectric interfacial space charges can shift the flat band voltage ($V_{fb}$) and, therefore, $V_{th}$. This can be derived analytically [153, 154] or by numerical, drift-diffusion based simulations [147, 155, 156, 157] and has also been measured in OTFTs [140].

An analogous model has been proposed for OTFTs containing acidic SAMs using regioregular poly(3-hexyl-thiophene) (rr-P3HT) as the active layer. In such devices, the 'normally on' (depletion mode) operation of the devices has been explained by proton transfer from the acid to the polythiophene [158]. Such acid-base reactions are well-known in polymers [159] or oligomers [160]. Their impact on the device characteristics can be understood in the following way (for the sake of simplicity assuming a negligibly small voltage drop between source and drain in the explanation): When applying no voltage between gate and source ($V_{GS}$), the proton transfer induces mobile

(vide infra) holes in the channel in analogy to the doping of the chemically related poly(3,4-ethylenedioxythiophene) (PEDOT) by protons of the acidic poly(styrenesulfonate) (PSS) [161]. The charge of these holes exactly compensates the (immobile) negative space charge layer originating from the acid residues. Applying a negative $V_{GS}$ then results in the accumulation of more holes, while a positive $V_{GS}$ is needed to deplete the channel. One can view the situation also purely 'electrostatically': If the space-charge layer due to the acid residues was not compensated by holes, it would induce opposite charges in the gate electrode. This would result in a potential drop over the dielectric in analogy to the situation in a plate capacitor putting the channel at a significantly different potential than the gate. This gives rise to carrier accumulation in the channel [147] equivalent to what would happen, if a voltage equal to the potential drop over the gate dielectric had been applied to the gate in the absence of any space charges.

Such acidic interfacial layers hold high promise for tuning the functionality of organic electronic devices. They allow the fabrication of chemoresponsive OTFTs detecting the presence of bases like ammonia that compensate the acid doping [158, 162]. They can also be used for a controlled chemical tuning of $V_{th}$ over more than 80 V in rr-P3HT based OTFTs containing acidic SAM [163]. Beyond that, some of us have recently used photo-acid polymers as interface modification layers to control the growth of organic layers [126] and to photo chemically tune $V_{th}$ [133]. The latter paves the way for the straightforward photolithographic production of inverters and potentially also more complex electronic circuits. Beyond that, protons at the semiconductor-dielectric interface have been found to play a decisive role for the bias-stress in OTFTs [164, 165] and it has been suggested that their production upon bonding of silanes to $SiO_x$ also impacts the device characteristics [166].

In several of the above examples, pentacene has been used as the active material. In contrast to the situation for P3HT, where the interaction with the acid can be viewed in analogy to doping in PEDOT/PSS (vide supra), for pentacene it is much less clear, what the actual processes are that result in threshold voltage shifts due to the presence of an acid at the interface

between the dielectric and the semiconductor. Clarifying that is of distinct relevance and, therefore, the topic of the present paper. In particular, we will provide evidence (i) that the main origin of the acid-induced $V_{th}$ shift is the formation of a space-charge layer at the interface, (ii) that the $V_{th}$ shift is the result of an acid base reaction, (iii) that the pentacene molecules are involved in that reaction, (iv) that it is the central carbon atoms of the pentacene molecules (i.e., those at the 6 and 13 positions) that are subject to protonation and (v) that the protonation results in the formation of free holes. This is achieved by combining a number of experimental investigations on different types of OTFTs with drift-diffusion based device modelling and quantum-mechanical simulations.

## 3.4 Results and discussion

The schematic structure of the investigated devices is shown in Fig. 3.1. We used pentacene and 6,13-bis(triisopropylsilylethynyl)pentacene (TIPS-pentacene) as the active layer. The OTFTs were fabricated on doped silicon substrates with a $SiO_x$ dielectric that has been modified using a blend of two functionalized trichlorosilanes namely 4-(2-(trichlorosilyl)ethyl)benzene-1-sulfonyl chloride (T-SC) and its sulfonic acid derivate 4-(2-(trichlorosilyl)-ethyl)benzenesulfonic acid (T-SA).

### 3.4.1 Varying the thickness of the oxide layer

To separate the effects of dipole and space-charge layers, we followed a suggestion from Ref. [147], where it has been shown that, when dipolar layers are responsible for the $V_{th}$ shift, it should be independent of the capacitance per unit area ($c_{ox}$) of the gate dielectric. When caused by a space charge layer, $V_{th}$ should, however, scale linearly with the inverse of $c_{ox}$. This can be simply understood when viewing gate electrode, dielectric, and channel as a plate capacitor (vide supra).

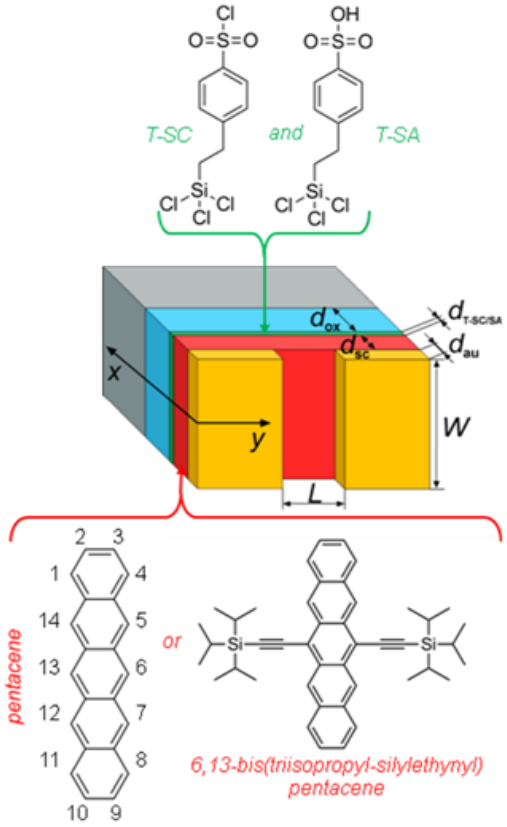


Figure 3.1: Schematic structure of the investigated top-contact bottom-gate device structure, with channel lengths of $L = 50\,\mu m$ or $L = 25\,\mu m$ and a channel width of $W = 7\,\text{mm}$. The orientation of the axes is such that a direct comparison with Fig. 3.5 showing the potential landscape is possible. The source and drain contacts are made of gold (Au) with a thickness of $d_{au} = 50\,\text{nm}$. The active layer material is either pentacene or 6,13-bis(triisopropylsilylethynyl)pentacene (TIPS-pentacene) with a layer thickness of $d_{sc} = 35\,\text{nm}$ or $d_{sc} = 56\,\text{nm}$, respectively. The positions at which pentacene can be protonated are numbered to ease discussions later in the manuscript. The semiconductor-dielectric interface layer is a blend of the two functional trichlorosilanes, T-SC and T-SA, and its thickness is in the range of 1 nm ($d_{T-SC/SA}$). Thermally grown silicon oxides with thicknesses of $d_{\text{ox}} = 102.2\,\text{nm}$, $d_{\text{ox}} = 147.5\,\text{nm}$, $d_{\text{ox}} = 152.0\,\text{nm}$ and $d_{\text{ox}} = 245.0\,\text{nm}$ are used as the dielectric.

For a given space charge, the potential drop in that capacitor and, thus (for a given gate potential) the potential of the channel is linearly proportional to the oxide thickness, $d_{ox}$. Therefore, we fabricated transistors with gate oxides of varying thickness. Exemplary transfer characteristics of (Si|$SiO_x$|T-SC/SA|pentacene|Au) OTFTs on oxides with nominal thicknesses $d_{ox-n}$ of 100 nm, 150 nm, and 250 nm are shown as solid squares in the three panels of Fig. 3.2.

In all devices, high, positive $V_{th}$ are observed, which increase with $d_{ox}$. Prior to further analysing these data, the layer structures of the device shall be characterized in more detail. As a first step, the relevant layer thicknesses, $d_{ox}$ and $d_{T-SC/SA}$ are determined by x-ray reflectivity (XRR) measurements. To obtain satisfactory agreement between measurements and fits (see Supporting Information 3.7), the T-SC/SA layers had to be modelled as a double layer structure, i.e. as consisting of two layers with different electron density. The obtained layer thicknesses ($d$), the surface root mean square (rms) roughness values ($\sigma$), and the refractive index decrements ($\delta$) are summarized in Tab. 3.1.

The measured $d_{ox}$ values deviate only slightly from the numbers provided by the wafer suppliers (i.e. $d_{ox-n}$). The $d_{T-SC/SA}$ values on the three substrates are virtually identical and in the range of what is expected for a monolayer, whose thickness has been calculated to be 0.96 nm [162]. This is insofar important as the wafers have been obtained from two different sources. We attribute the similar SAM growth to the substrate pretreatment (cf. Experimental section 3.6) and the carefully controlled growth conditions.

Also the contact angles of diodomethane ($\Theta_d$) and deionized water ($\Theta_w$) as well as the derived surface free energies per unit area ($E_s$) of the T-SC/SA layers are in the same range for the three samples (see Tab. 3.1). Es is apparently largest for $d_{ox} = 102.2$ nm, but the variations between the two measurement series (cf. Supporting Information) are in the same range as the differences between the substrates. As far as pentacene growth on the T-SC/SA layers is concerned, we find similar 'over-all' morphologies on all substrates with the typical dentritic pentacene grain shape.

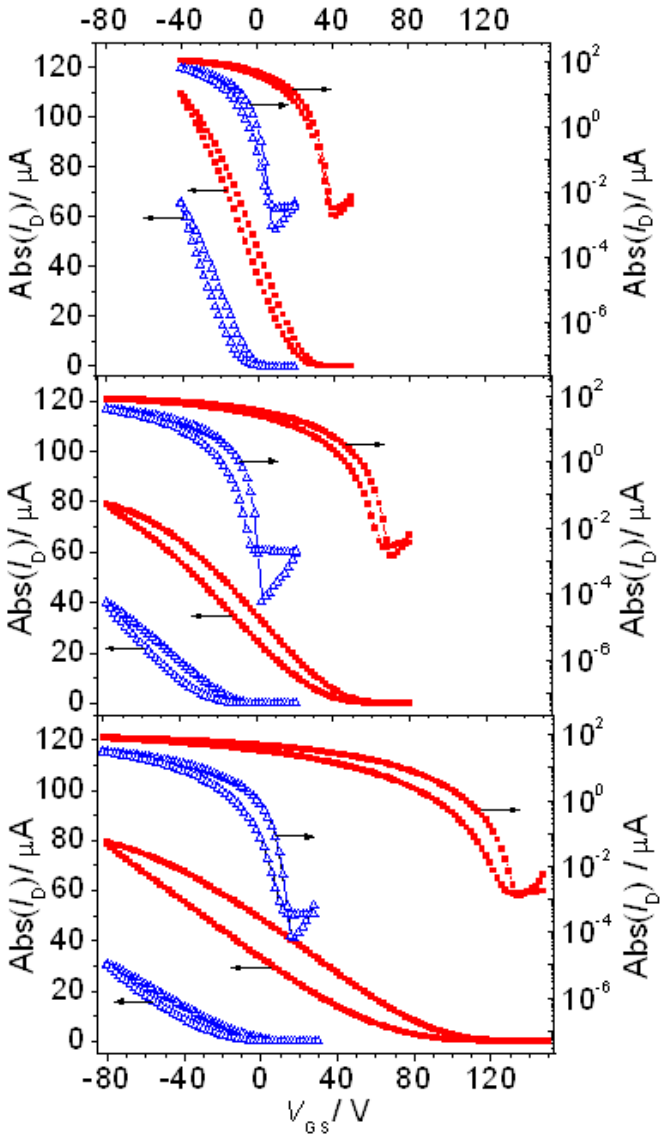


Figure 3.2: Exemplary transfer characteristics of pentacene based devices including a T-SC/SA semiconductor-dielectric interface layer with nominal (actual) oxide thicknesses of $d_{ox-n}$ = 100 nm ($d_{ox}$ = 102.2 nm), $d_{ox-n}$ = 150 nm ($d_{ox}$ = 147.5 nm), and $d_{ox-n}$ = 250 nm ($d_{ox}$ = 245.0 nm). Solid squares correspond to devices before and open triangles to devices after exposure to a flow of pure $NH_3$ gas. The source-drain voltage ($V_{DS}$) was set to -2 V. The increased hysteresis in the bottom plot is primarily a consequence of the extended measurement range. Further data are found in the Supporting Information 3.7.

Table 3.1: left: Thickness ($d$), root mean square roughness ($\sigma$) and refractive index decrement ($\delta$) of the fitted 3-layer structure for the three different oxide thicknesses ($d_{ox}$); The net-thickness of the T-SC/SA layer, $d_{T-SC/SA}$, is given by the sum of $d_{T-SC/SA-1}$ and $d_{T-SC/SA-2}$. right: average water contact angles $\Theta_w$, diiodomethane contact angles $\Theta_d$, and surface free energies per unit area $E_s$ . Average values obtained for two measurement series on separately prepared layers are reported (the full data set is contained in the Supporting Information 3.7).

| $d_{ox}$ | $\sigma_{ox}$ | $\delta_{ox}$ | $d_{T-SC/SA-1}$<br>$d_{T-SC/SA-2}$ | $\sigma_{T-SC/SA-1}$<br>$\sigma_{T-SC/SA-2}$ | $\delta_{T-SC/SA-1}$<br>$\delta_{T-SC/SA-2}$ | $d_{T-SC/SA}$ | $\Theta_d$ | $\Theta_w$ | $E_s$ |
|---|---|---|---|---|---|---|---|---|---|
| $[nm]$ | $[nm]$ | $[10^{-6}]$ | $[nm]$ | $[nm]$ | $[10^{-6}]$ | $[nm]$ | $[\frac{1}{2}]$ | $[\frac{1}{2}]$ | $[\frac{mJ}{m^2}]$ |
| 102.2 | 0.46 | 73.0 | 0.7<br>0.3 | 0.10<br>0.24 | 36<br>46 | 1.0 | 35.5 | 62.0 | 52.6 |
| 147.5 | 0.43 | 73.0 | 0.7<br>0.3 | 0.10<br>0.24 | 36<br>46 | 1.0 | 36.4 | 65.9 | 50.3 |
| 245.0 | 0.48 | 73.0 | 0.7<br>0.4 | 0.10<br>0.25 | 36<br>46 | 1.1 | 37.3 | 66.2 | 49.9 |

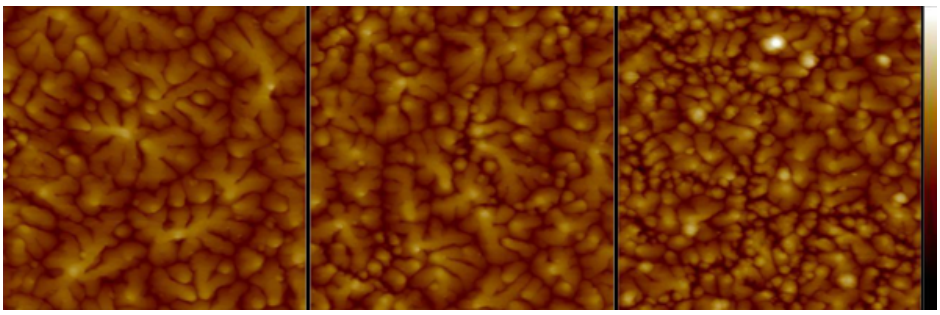

Figure 3.3: AFM images showing $5\,\mu m$ x $5\,\mu m$ sections of 35 nm thick pentacene layers grown on T-SC/SA covered $SiO_x$ dielectrics with $d_{ox} = 102.2$ nm (left), 147.5 nm (center) and 245.0 nm (right).

The average grain size of the pentacene crystallites are, however, largest

on the $d_{ox} = 102.2\,\text{nm}$ substrate, which has the largest $E_s$, as can be seen in the exemplary pictures in Fig. 3.3 (*cf.* Ref. [167, 168, 169]). Having characterized the layers, we now turn to a more detailed evaluation of the transfer characteristics shown in Fig. 3.2. The obtained average values for the turn-on ($V_{on}$) and the threshold voltages, the calculated mobilities ($\mu$), and the on-to-off ratios ($I_{on}/I_{off}$) are summarized in the top part of Tab. 3.2. These values have been extracted from the off-to-on sweeps at a drain-source voltage ($V_{DS}$) of $-2\,\text{V}$. A certain complication arises from the fact that there are a number of methods for determining $V_{th}$ that do not necessarily yield equivalent values [170]. Therefore, we included the results obtained using the extrapolation in the linear region (ELR) [170], the second derivative method (SD) [170], and the logarithmic second derivative method (SDL) [170]. The corresponding threshold voltages are denoted as $V_{ELR}$ and $V_{SD}$ while $V_{SDL}$ is associated with the turn-on voltage, as it corresponds to the point of highest curvature in the logarithmic plots of the transfer characteristics.

In Ref. [170] the SD method, where $V_{th}$ is associated with the maximum of the second derivative of $I_D$ with respect to $V_G$, has been suggested for extracting $V_{th}$. In a few of our devices, we, however, observe a relatively constant curvature of the transfer characteristics over a relatively wide voltage range in spite of the only very small applied $V_{DS}$ of $-2\,\text{V}$. We also often suffer from a relatively poor signal to noise ratio when calculating the numerical second derivative. In contrast, the ELR method can be readily applied and appears reasonable considering the relatively wide voltage range over which $I_D$ depends linearly on $V_{GS}$ (see Fig. 3.2). Also the reported $\mu$ values have been calculated for that region.

The devices with $d_{ox} = 147.5$ and $d_{ox} = 245.0\,\text{nm}$ show similar $\mu$. The latter nearly doubles for $d_{ox} = 102.2\,\text{nm}$ consistent with the large size of the pentacene crystals (see Fig. 3.3) [126, 168, 171, 172]. As shown in Fig. 3.4, all extracted voltages increase close to linearly with $d_{ox}$ and thus also with $1/c_{ox}$ [173]. From what has been discussed above, this indicates that the formation of a space-charge layer is the primary cause for the $V_{th}$ shift. Interestingly, however, for all fitted lines we obtain an intercept with the $V_{th}$-axis at negative voltages of -32 V (ELR), -30 V (SD) and -35 V (SDL). The magnitude of

this 'voltage offset' is clearly larger than the estimated standard deviation for the intercept of about 5 V extracted for the three fit functions. The fit to the $V_{on}$ (equalling $V_{SDL}$) is, naturally, 'compromised' by the sub-threshold swing and the values of $V_{ELR}$ and $V_{SD}$ suffer from the ambiguity of the threshold-voltage determination. Nevertheless, this non-zero axis intercept suggests that part of the $d_{ox}$-dependent $V_{th}$ shift arising from the space-charge layer is, as a secondary effect, compensated by a dipole layer.

Table 3.2: Device parameters of (Si|$SiO_x$|T-SC/SA|pentacene|Au) transistors as function of different oxide thicknesses ($d_{ox}$) before (top part) and after $NH_3$ exposure (bottom part, *cf*, discussion in section 2.3). Threshold/onset voltages derived with different methods, $V_{ELR}$, $V_{SD}$, and $V_{SDL}$ (details see main text), mobilities ($\mu$) , and on-to-off ratios ($I_{on}/I_{off}$) are reported. $I_{off}$ is defined as the drain current when the gate voltage equals $V_{on}$ and $I_{on}$ is the current for $V_{GS}$ equaling $V_{on} - 40$ V. All values are average values over three different devices. A more detailed compilation of the measurement results can be found in the Supporting Information 3.7.

| $d_{ox}$ $[nm]$ | $c_{ox}$ $[\frac{nF}{cm^2}]$ | $V_{ELR}$ $[V]$ | $V_{SD}$ $[V]$ | $V_{SDL}$ $[V]$ | $\mu$ $[\frac{cm^2}{Vs}]$ | $I_{on}/I_{off}$ $[10^3]$ |
|---|---|---|---|---|---|---|
| 102.2 | 34.8 | 20 | 25 | 38 | 0.24 | 30 |
| 147.5 | 23.0 | 39 | 44 | 65 | 0.12 | 20 |
| 245.0 | 14.1 | 90 | 98 | 136 | 0.13 | 2 |
| $d_{ox}$ $[nm]$ | $c_{ox}$ $[\frac{nF}{cm^2}]$ | $V_{ELR-NH3}$ $[V]$ | $V_{SD-NH3}$ $[V]$ | $V_{SDL-NH3}$ $[V]$ | $\mu_{NH3}$ $[\frac{cm^2}{Vs}]$ | $(I_{on}/I_{off})_{NH3}$ $[10^3]$ |
| 102.2 | 34.8 | $-5$ | 1 | 8 | 0.22 | 60 |
| 147.5 | 23.0 | $-16$ | $-9$ | 3 | 0.11 | 90 |
| 245.0 | 14.1 | $-9$ | $-3$ | 20 | 0.12 | 40 |

This offset is significantly larger than what one would expect from the difference in work functions of the gate electrode and the semiconductor material. A certain contribution also comes from the intrinsic molecular dipoles

of the T-SC/SA molecules that have been calculated to be a few Debye resulting in potential shifts of a few volts [158]. The bond-dipole due to the binding of the silanes to the dielectric surface should additionally somewhat influence the situation. All these effects can, however, not fully explain the magnitude of the dipole-induced shift. Possible origins of the necessary 'extra' dipole could be trapped protons that did not react with the pentacene (vide infra), or also trapped holes. Note that it follows from basic electrostatics that positive charges trapped above the negatively charged acid residues should not be considered as a space charge layer with a $d_{ox}$-dependent impact.

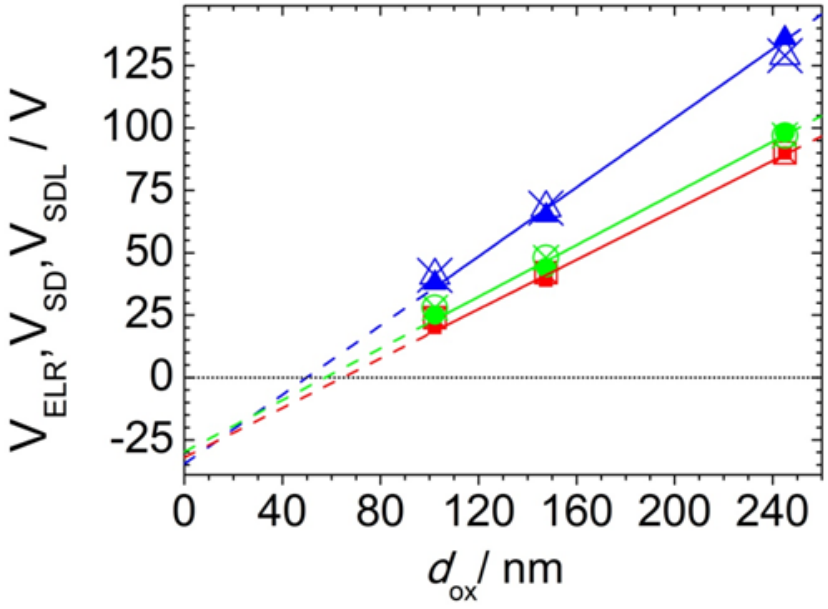


Figure 3.4: Dependence of $V_{ELR}$ (solid squares), $V_{SD}$ (solid circles) and $V_{SDL}$ (solid triangles) on $d_{ox}$ for devices with three different $d_{ox}$. The plotted solid symbols correspond to the average experimental values, the solid lines are linear fits and the open symbols have been extracted from the results of drift-diffusion based modelling. They have been obtained by applying the same procedures used for analysing the experimental data (see main text) also to the simulated transfer characteristics.

As long as their density is smaller than that of the negatively charged acid residues they rather form a charged double layer (i.e. a dipole layer)

with part of the negative charges from the acid residues. This makes their impact independent of $d_{ox}$.

### 3.4.2 Results of drift-diffusion based device simulations

The above described situation is fully consistent with the results of drift-diffusion based simulations. Assuming an uncompensated negatively charged interfacial space charge layer with an areal space-charge density of $-1.5$ x $10^{17}\,\mathrm{em}^{-2}$ and a dipole layer with a dipole density corresponding to a potential jump of $-31\,\mathrm{V}$, the experimental trend for $V_{th}$ can be fully reproduced (see open symbols in Fig. 3.4). The above space charge density corresponds to about 12 % of the acid groups being deprotonated assuming a molecular density at the interface of 1.3 * $10^{18}\,\mathrm{m}^{-2}$ (i.e., 1/3 of the molecular packing density of the SAM obtained when assuming a $25\,\mathrm{Å}^2$ footprint in this way accounting for the T-SC/T-SA ratio in the used sample)

To fully reproduce the measured transfer characteristics, a relatively complex model including different types of traps (to reproduce the sub-threshold swing and the hysteresis) as well as a mobility depending on $d_{ox}$ to account for the different experimentally observed film morphologies needs to be employed. The results from these simulations have been used for the data in Fig. 3.4 and are contained in the Supporting Information 3.7. To understand the fundamental processes responsible for the $V_{th}$ shifts, it is, however, advisable to discuss the situation within a simplified model, disregarding traps and assuming a constant mobility in all devices. The resulting potential distributions in the device at $V_{DS} = -2\,\mathrm{V}$ for the three $d_{ox}$ values are shown in Fig. 3.5 (a). The left panels depict the situation immediately after applying the voltages, while the right panels show the steady-state situation. The gate bias $V_{GS}$ is chosen such (i) that all devices operate in the linear regime and (ii) that the same total steady-state current (here arbitrarily set to $I_{DS} = 81\,\mu\mathrm{A}$) is achieved for all oxide thicknesses. This corresponds to $V_{GS} = -12.5\,\mathrm{V}$, $-3.3\,\mathrm{V}$, and $15.3\,\mathrm{V}$, for $d_{ox} = 100\,\mathrm{nm}$, $150\,\mathrm{nm}$, and $250\,\mathrm{nm}$, respectively. Discussing a situation with $I_{DS} = \mathrm{const}$ represents a more general situation than merely discussing the onset regimes.

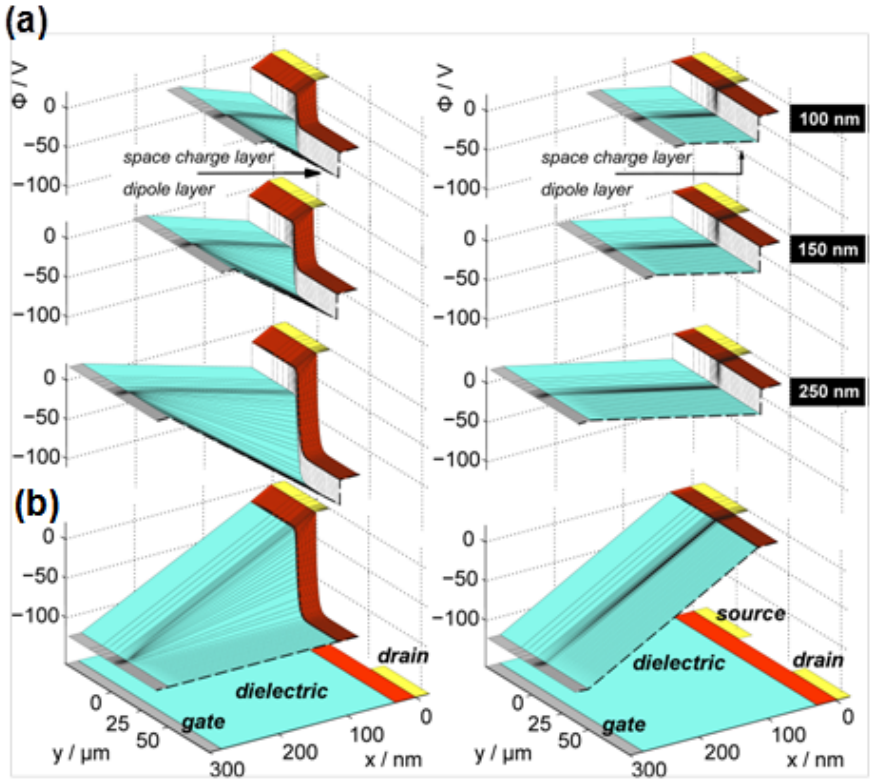


Figure 3.5: (a) Simulated potential distributions for devices with a fixed negative space charge layer and a fixed dipole layer at the semiconductor-dielectric interface for oxide layer thicknesses $d_{ox} = 100\,\text{nm}$, 150 nm, 250 nm. Shown is the situation in the absence of mobile charges (left column) and for the steady state (right column) in the linear regime ($V_{DS} = -2\,\text{V}$). The gate biases $V_{GS}$ are chosen to induce the same total amount of accumulated charges in the steady state ($I_{DS} = 81\ \mu\text{A}$) for all oxide thicknesses, ($V_{GS} = -12.5\,\text{V}$, $-3.3\,\text{V}$, and $15.3\,\text{V}$). To prevent obscuring important details, we omit showing the potential in the ï¿½drain-regionï¿½ of the device; the position of the corresponding cut in the profiles is indicated by a broken line.

The latter, however, can be easily recovered by setting $I_{DS} = 0\,\text{A}$. Note that for $I_{DS} \neq 0$, the differences in the associated $V_{GS}$ do not directly correspond to the offsets in $V_{th}$, as in the transfer characteristics also the slope of the $I_{DS}(V_{GS})$ curves is proportional to the capacitance of the dielectric (i.e.,

inversely proportional to $d_{ox}$).

To illustrate the impact of the space charge and dipole layers on the potential distribution, we first discuss the situation for the instant the external voltage is applied (i.e., before mobile charges are injected). In that case, gate, drain, and source electrodes are set to a fixed potential and no mobile charges are in the device. Without space charges or dipoles at the interface (see Fig. 3.5 (b)), the potential in the pentacene volume that is not covered by source or drain electrodes ($0 < y < 50$ $\mu$m) assumes the value of the gate potential. This is a consequence of the huge aspect ratio of the considered transistors (channel length of 50 $\mu$m vs. an overall thickness of the active region and dielectric between 135 nm and 285 nm).[147] Further, the potential drops linearly from the source/drain electrodes to the gate electrode ($y \leq 0, 50\,\mu\text{m} \leq y$) with different slopes in the semiconductor and the dielectric as dictated by their dielectric constants.

The situation in the channel region not covered by the source- and drain electrodes is significantly modified in the presence of the interfacial space charges and dipole layers. Due to the space charge layer, there is an additional voltage drop across the dielectric layer (Fig. 3.5 (a), left panels). The corresponding electric field in the oxide layer is the same for all oxide thicknesses as a consequence of comparing situations with equivalent drain currents in the steady-state (vide supra). The extent of the potential drop increases linearly with $d_{ox}$, reminiscent of the situation in a plate capacitor. The potential step at the interface due to presence of the dipole layer partly counteracts the potential drop over the oxide. Since the height of this step is, however, solely determined by the dipole density, it is independent of $d_{ox}$.

Underneath the source and drain electrodes, a different situation is encountered: Here, the total potential difference is given by $V_{GS}$ and VGD, respectively. As a consequence, there is a potential drop over the pentacene layer (unlike in the channel region far from source and drain described in the previous paragraph). For the three situations depicted in Fig. 3.5 (a), this potential drop is independent of $d_{ox}$. This follows from the requirement that for the steady state all drain currents are identical. The same requirement explains why also the field in the oxide does not depend on $d_{ox}$. This then

results in the observed $d_{ox}$ dependent potential drop over the oxide that is offset by the potential discontinuity due to the dipole layer.

For reaching the steady state (Fig. 3.5 (a), right panels), charges are injected from the source electrode and accumulate in the channel region. As a consequence, in the regions underneath the contacts the potential in the pentacene layer is fixed to the source and drain potentials. I.e., there is neither a field in the x- nor in the y-directions. Also in the part of the device not covered by the electrodes, the field in the x-direction vanishes, but there is a steady potential drop in the y-direction as a consequence of the applied $V_{DS}$ (as the latter is chosen to be only $-2\,\mathrm{V}$ here, this potential drop is, however, not well resolved in Fig. 3.5). Because we compare the situation of identical $I_{DS}$, the accumulated hole density at the semiconductor/dielectric interface is the same for all $d_{ox}$, which also renders the field in the oxide identical.

### 3.4.3 Dedoping by ammonia and bulk doping using hydrochloric acid

To determine, whether the $V_{th}$ shift is a consequence of an acid-base reaction, we performed two test experiments: First, we exposed the devices containing the T-SC/SA layers to a base as the latter should neutralize the acid; for that purpose we chose $NH_3$ gas and exposed the devices for 30 min to ensure that an equilibrium situation is established (details see Experimental section 3.6 and Supporting Information 3.7). This exposure results in a substantial shift of $V_{th}$ to less positive values with the total shift being essentially proportional to $d_{ox}$ (see Fig. 3.2). As a result, the $V_{th}$ values of all devices after $NH_3$ exposure become similar. In analogy to what has been described in [158, 162] for P3HT based devices, this shift can be explained by a neutralization of the acidic groups of the T-SA molecules by $NH_3$ resulting in the formation of the electronically inactive ammonium 4-(2-(trichlorosilyl)ethyl)benzenesulfonate as shown for pristine T-SC/SA layers by various spectroscopic techniques [162]. Interestingly, the $I_{off}$ are in the same range before and after $NH_3$ exposure [174].

In a second test experiment, we exposed (Si|$SiO_x$|pentacene|Au) devices,

i.e., devices not containing a T-SC/SA interfacial layer, to HCl gas. The resulting device characteristics are shown in Fig. 3.6.

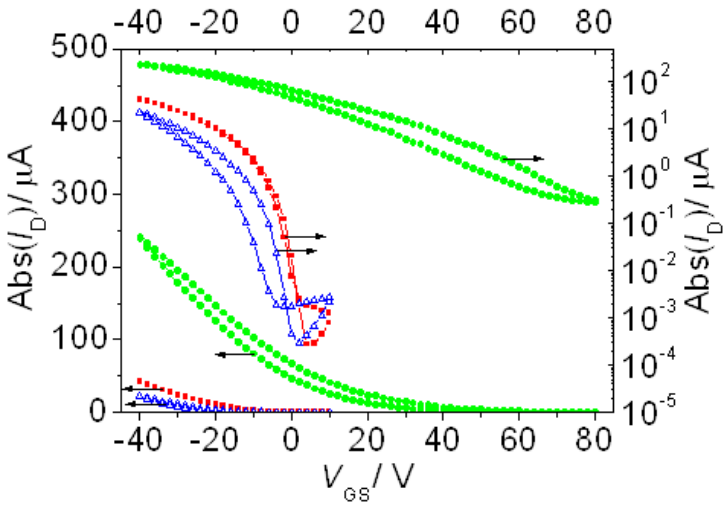


Figure 3.6: Transfer characteristics of an exemplary (Si|$SiO_x$|pentacene|Au) device with $d_{ox}$ = 152.0 nm (solid squares), after exposure to HCl vapour (solid circles) and after subsequent exposure to $NH_3$ (open triangles). $V_{DS}$ is set to −2 V. Further data are found in the Supporting Information 3.7.

Very much like in the devices containing an acidic interfacial layer, exposure of 'conventional' (Si|SiOx|pentacene|Au) transistors to HCl vapor results in highly positive $V_{th}$ and $V_{on}$. This shift to positive $V_{th}$ is stable over days when keeping the devices in an Ar-glove box, which indicates a strong chemical interaction between pentacene and the HCl molecules, because otherwise HCl would gradually diffuse out of the device. The fact that again $V_{on}$ can be shifted back to around zero upon exposure of the device to $NH_3$ gas (see open triangles in Fig. 3.6) shows that also here we are dealing with acid-base reactions. This is consistent with the notion that bulk doping of the active layer material shifts $V_{th}$ as derived on the basis of analytic equations [153, 154, 155] and by drift-diffusion based simulations [147, 156, 157].

Thus, we propose a protonation of some of the pentacene molecules in the active layer upon interaction with a strong enough acid (HCl vapour or the T-SC/SA interface layer). Protonation of pentacene molecules in

the gas phase has, indeed, been suggested by quantum chemical simulations [175, 176] and by several different experimentally measurements, namely by Fourier transform ion cyclotron resonance mass spectrometry [175], IR and IR multiple-photon dissociation spectroscopy [177]. The experiments presented here are a strong indication that analogous reactions occur also in the solid state.

Interestingly, the exposure to HCl vapour in several of the investigated devices resulted in a deterioration of the $I_{on}/I_{off}$ ratio as a consequence of a significant increase of $I_{off}$. This is in clear contrast to the insertion of the T-SC/SA layer as shown in Fig. 3.2. It should, however, be mentioned that the measured values of $I_{off}$ upon exposure to HCl display a significant device-to-device variation as shown in the Supporting Information 3.7.

A possible explanation for the increased $I_{off}$ in Fig. 3.6 is that exposure to HCl vapor induces proton-transfer doping throughout the whole film, while it is reasonable to assume that the use of an interfacial layer (like T-SC/SA) primarily affects the region close to the semiconductor-dielectric interface. In literature [178] it has indeed been suggested that bulk doping results in an increased off current. This, is, however, cast into doubt by Refs. [156, 157], where it is argued that such an increase of $I_{off}$ is a consequence of traps, while bulk doping without trap creation (albeit at a much lower concentration than in [172]) only results in a shift of $V_{th}$.

### 3.4.4 Acid-base reactions in TIPS-pentacene based devices

To clarify, which part of the pentacene molecule is actually affected by the protons of the acid, it is useful to consider the proton affinity (PA) of the various carbon positions. Calculations in Ref. [175, 176] indicate that the two carbon atoms of the central ring in pentacene have the highest PA. Our quantum-chemical simulations at the B3LYP/6-31G(d,p) level indeed confirm that the protonation of pentacene at the central 6 position is energetically favoured by 0.87 eV (resp. 0.74 eV and 0.15 eV) over a protonation at the 3 (resp. 4 and 5) positions (the numbering of the carbon atoms in the

pentacene backbone is included in Fig. 3.1).

To test experimentally, whether this is the case also in the solid state, we performed comparative studies using a suitably modified pentacene derivative as the active semiconductor material: In TIPS-pentacene (chemical structure see Fig. 3.1), the central two carbon atoms of pentacene are substituted by triisopropyl(prop-1-yn-1-yl)silane, which can be expected to very significantly modify their proton affinity. Indeed, already when fully optimizing the structure of a protonated TIPS-pentacene molecule (corresponding to the gas phase), the energetic 'advantage' of the 6 over the 3 position is reduced to 0.48 eV (0.37 eV for the 4 position; protonation at the 5 position is, in fact, energetically favoured here by 0.25 eV). Moreover, primarily due to a change in hybridisation of the protonated carbon atom, the structure of the molecule is heavily distorted as shown in the Supporting Information 3.7. Such a distortion will not happen in the solid state, especially in a highly crystalline [179], densely packed layer. Thus, we also calculated the total energy of a protonated TIPS-pentacene molecule, in which the central part of the backbone was forced to remain planar. In this case, protonation at the central carbon atom becomes energetically more costly by 0.37 eV (resp., 0.48 eV and 1.10 eV) than protonation at the 3 (resp. 4 and 5) positions. These data shows that due to the substitution protonation at the central carbon atoms can be excluded in a TIPS-pentacene film.

Thus, if the above described high positive $V_{th}$ upon insertion of a T-SC/SA layer or exposure to HCl vapor were, indeed, the consequence of a protonation of the central pentacene carbon atoms, they should not occur when using TIPS-pentacene as the active material. This is exactly what we observe in the corresponding test experiments, where neither the inclusion of a T-SC/SA layer nor the exposure to HCl vapor gives rise to any shift in $V_{th}$ (for transfer characteristics see the Supporting Information 3.7). This can be considered as convincing evidence that (i) the acid-induced $V_{th}$ shifts in pentacene-based devices are a consequence of a chemical reaction between the acid and the active material and not, e.g., due to an interaction with silanole surface groups or related species; and that (ii) the position of protonation in pentacene is at the central carbon atom.

### 3.4.5 The suggested mechanism for surface proton transfer doping in pentacene based OTFTs

The above results lead us to suggest the mechanism depicted in Fig. 3.7 for surface proton transfer doping in pentacene based OTFTs: A fraction of the pentacene molecules close to the interface with the T-SC/SA layer are protonated. This fraction remains relatively small, as can be inferred from the drift-diffusion based modelling (vide supra). Such a situation is consistent with the protonation being an endothermal process rendering the reaction entropy-driven. The positive charge on the pentacene molecule originating from the proton transfer is then transferred to a neighbouring molecule. This is necessary to explain the experiments, as otherwise one would be dealing with trapped rather than mobile holes as a result of the proton-transfer doping process.

It is also consistent with our quantum-chemical simulations, as the charge transfer to a non-protonated pentacene results in an energy gain of 0.60 eV. This value is obtained from the comparison of the B3LYP/6-31G(d,p) calculated ionization potentials of pentacene and the pentacene-6-ylium with an additional proton at the central position (for chemically structure see Fig. 3.7) and assumes equivalent screening in both systems. The reason for the increased ionization potential of the molecule bearing the extra proton is the disrupted conjugation by the central $sp^3$ hybridized carbon atom. As a consequence, pentacene-6-ylium molecules will no longer participate in the hole transport at the interface, but they will also not act as traps. Thus, the carrier mobility should not be reduced by the protonation of a small fraction of the pentacene molecules, which is again consistent with the experiments. Considering the increased reactivity of pentacene-6-ylium molecules in situation (c) of Fig. 3.7 due to their radical character, it cannot be excluded that these molecules are actually subject to a second protonation process, but we have no clear evidence for this to actually happen.

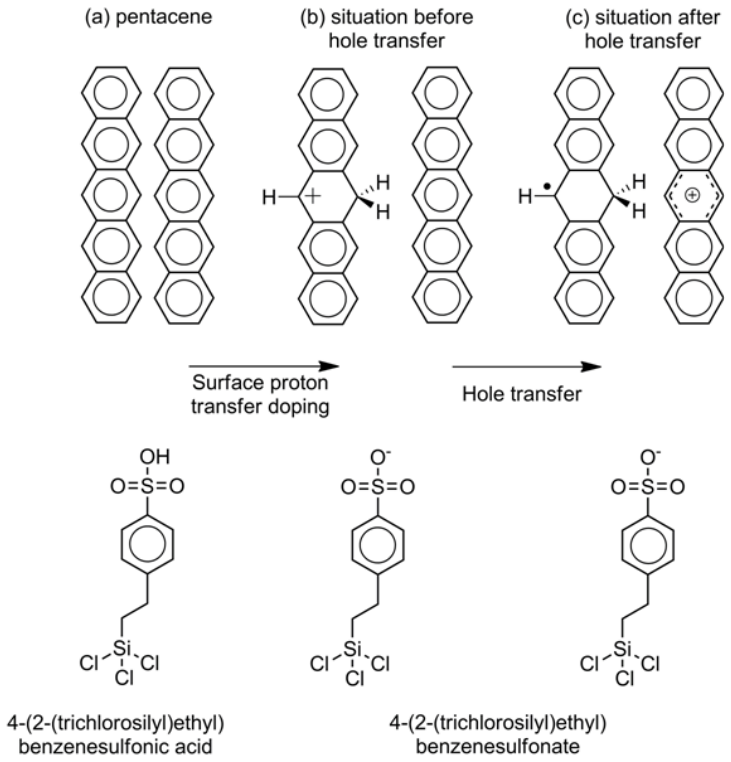


Figure 3.7: Suggested mechanism for surface proton transfer doping of pentacene by the protons of the sulfonic acid functionalities of the T-SA molecules. (a) shows the situation before doping. (b) shows a protonated pentacene molecule (pentacene-6-ylium); the resulted disruption of the conjugation results in the positive charge being transferred to a neighbouring molecule, forming a free hole (c).

### 3.4.6 Establishing equilibrium and the role of ambient light

Finally, it should be noted that the high positive $V_{th}$ values induced by a T-SC/SA layer and depicted in Fig. 3.2 develop only gradually. I.e., for devices stored in the glove-box in light (i.e., without any intentional darkening), it takes several days until a stable situation is reached that also does not change under the measurement conditions described below. In contrast, the equilibrium is established instantaneously, when performing the doping experiments

using HCl vapour. This can be attributed to the abundance of HCl molecules when exposing the devices to HCl vapour. Interestingly, we saw immediate doping also when using two types of polymeric interfacial layers that consist of photo acids [133]. We attribute this to the fact that in these experiments, to form the acids, we illuminate the samples by UV-light and it is known for several organic systems that their acidity is much higher, when the molecules are in the excited state [180, 181, 182, 183].

In fact, also for doping with a T-SC/SA interfacial layer, the exposure to light impacts the steady-state situation. When storing a device in darkness for a month right after fabrication, the achieved positive $V_{th}$ were clearly smaller than in a control device stored under ambient light. When the latter device is then kept in darkness for several days, its $V_{th}$ shifts back to the value measured for the device never exposed to ambient light. This could be a consequence of a shift in the chemical equilibrium of the reactions depicted in Fig. 3.7 upon illumination.

On the other hand, a 'darkness-induced' shift of $V_{th}$ to more negative values is reminiscent of the experiments by Jing et al., who observed (albeit for P3HT based devices on bare $SiO_x$, i.e., without any interface modifications) threshold voltages as low as -60 V when storing their devices in the dark [184], which can be attributed to charge-carrier trapping. In that spirit, it cannot be excluded that the less positive values of $V_{th}$ for T-SC/SA containing pentacene devices stored in the dark are due to a partial cancellation of the doping effect by charge carrier trapping rather than a result of a shifted chemical equilibrium. To definitely answer such questions, extensive tests of the impact of light (of different wavelength) on various types of transistors containing different interface modifications and active layer materials will be necessary. This goes clearly beyond the scope of the present paper.

## 3.5 Conclusions

Combining a number of experiments with drift-diffusion based device modelling and quantum-chemical calculations, we study the mechanism respon-

sible for the high positive threshold voltages observed in pentacene based OTFTs, where the active layer is in contact with an acid. This is of relevance as, for example, devices containing acidic layers have a high potential for realizing chemically responsive devices [185] and allow for an efficient photochemical production of depletion-load inverters [133]. The focus of the present study lies on pentacene transistors containing acidic monolayers covalently bonded to the gate dielectric. The theoretical and experimental investigation of the dependence of the monolayer-induced threshold-voltage shift on the thickness of the gate dielectric reveals that it is due to the formation of an interfacial space-charge layer partially compensated by the formation of a dipole layer. The fact that a similar effect can be realized by HCl exposure of devices not containing an acidic layer and the finding that the $V_{th}$ shift can be eliminated by exposing the devices to a base (in our case $NH_3$) show that the observed doping is the consequence of an acid/base reaction. Interestingly, none of the above effects is observed when replacing pentacene by TIPS-pentacene. This, on the one hand, proves that it is the interaction between the acid and the active material that is responsible for the $V_{th}$ shift and, on the other hand, points to the central two carbon atoms of pentacene being subject to the electrophilic attack by the protons. It also implies that whether or not a certain semiconductor is prone to protonation (and, thus, useful for the above mentioned applications), subtly depends on the proton affinity of the available docking sites. These data together with results of quantum-chemical simulations finally allow suggesting the chemical and electronic mechanism sketched in Fig. 3.7 for surface proton transfer doping in pentacene based OTFTs.

## 3.6 Experimental

As especially the growth of the T-SC/SA layers is impacted severely by the very details of the fabrication process (especially by minute changes of the water concentration during film growth), we considered it appropriate to provide a very detailed description of the applied methodologies. Due to

space limitations, they are, however, largely contained in the Supporting Information 3.7.

*Device fabrication:* As substrates (serving also as gate electrodes), we used doped silicon wafers with thermally grown oxides with thicknesses $d_{ox}$ = 102.2 nm, $d_{ox}$ = 147.5 nm, $d_{ox}$ = 152.0 nm, and $d_{ox}$ = 245.0 nm pre-cut into 2 cm x 2 cm pieces supplied by Siegert Consulting and Silchem. The oxide surfaces of the substrates were cleaned and activated by an oxygen plasma etching process and subsequently sonicated for 2 min in deionized water. This rendered the oxide surfaces of all samples highly hydrophilic lowering the contact angle of $H_2O$ to below 10ï¿½, the limit of our contact-angle measurement set-up. This is important as the resulting high concentration of -OH groups on the waver surface is beneficial for the docking of silanes [186]. As a next step, T-SC/SA layers were grown on the majority of the wafers as described below. The active layer material pentacene was deposited under high-vacuum conditions typically some days after growing the T-SC/SA layer. The first 5 nm were deposited at a rate of 0.02 ï¿½/s and the following 30 nm at a rate of 0.1 ï¿½ /s, as measured with a quartz microbalance. During pentacene-growth, the substrates were held at a temperature of 65 ï¿½C. Alternatively, TIPS-pentacene films were deposited from a 1 t % solution in toluene by spin coating in air with the substrate heated to 60 ï¿½C using an IR lamp (spin parameters set to: 2000 rpm for 18s and 4000 rpm for 20 s). The ca. 50 nm thick gold source and drain electrodes were produced at a pressure in the range of $10^{-6}$ mbar in a home-built evaporation set-up operated inside an Ar glove-box. Four transistors were fabricated on each substrate.

*Growth of the T-SC/SA layer:* After the plasma etching process and the water sonication, the substrates were further cleaned in several steps (cf. Supporting Information 3.7) and put into 10 ml highly dry toluene (water content of about 7 ppm measured with Karl Fischer Titration) inside an Ar glove-box. To that we added 10 $\mu$l of the commercial T-SC/SA solution from ABCR, which is a 50 vol % mixture of T-SC/SA molecules and toluene and let the layer grow for 16 h. After this time, the substrates were sonicated and rinsed in fresh toluene. Finally, they were annealed for 30 min at about 100 ï¿½C at a pressure of about 0.6 mbar.

The *XRR data* were recorded on a Bruker D8 Discover diffractometer using CuK$_\alpha$-radiation and analyzed using WinGixa [187], which is an implementation of Parratt' s recursive algorithm [188]. It includes interface, $\sigma_{ox}$, and surface roughness, $d_{T-SC/SA}$, according to the approach of Nevot and Croce [189]. *Contact angles* were measured with a Kruess DSA 100 drop shape analysis system using deionized water and diiodomethane as test liquids. Based on the method by Owens Wendt [190] the surface free energy per unit area $E_s$ of the T-SC/SA layers were calculated automatically. *AFM pictures* were measured with a Veeco Dimension DI3000 in tapping mode with standard silicon tips.

To *expose the devices to $NH_3$ gas*, we put our devices in a homemade measurement cell and flooded the cell with $NH_3$ gas for either 30 min (data in Fig. 3.2) or 1 min (data in Fig. 3.6). After the $NH_3$ exposure, we flooded the cell with argon gas until we could not detect ammonia at the gas outlet of the measurement cell. For HCl-vapor exposure, we put the ready-made devices over a beaker filled with fuming hydrochloric acid for 1 min. *Hazard warning! $NH_3$ is highly toxic and HCl vapor is very acidic; thus, experiments should always be performed in a fume hood using appropriate gloves and protective glasses!*

*Source meter measurements:* To measure the electronic characteristics of the transistors, we used a Keithley 2636A dual source-meter controlled with a home-made software. We started the transfer sweeps at positive gate bias, reduced $V_{GS}$ in steps of $-2$ V (setting the delay time to 0.1 s). The reported device parameters were always determined for the sweep from positive to negative $V_{GS}$. All measurements were performed under ambient light inside a glove box.

*Drift-diffusion based modeling:* The numerical model to describe device characteristics is a two-dimensional drift-diffusion approach as described in Ref. [147] with special boundary conditions at the source and drain electrodes. Charge carrier injection occurs via thermionic emission and tunnelling through a potential barrier (given by the image charge model) in the Wenzel-Kramers-Brillouin approximation and is corrected by an interface recombination current [191]. The corresponding system of equations with

appropriate boundary conditions is solved self-consistently on a non-regular two-dimensional grid [147][25] using an implicit time integration. A hole injection barrier of 0.47 eV [192] and dielectric constants of $\epsilon = 3.4$ (pentacene) and $\epsilon = 3.9$ ($SiO_x$) are assumed. To model interfacial charge and dipole layers areal charge distributions with fixed densities were used. To further account for the shapes of the I-V curves obtained in the experiments also two types of traps need to be considered: (i) The occurrence of a hysteresis is simulated by including bulk traps, whose occupation is determined self-consistently for each time step. (ii) To account for the shape of the transfer-characteristics in the sub-threshold region, additional interface traps with significantly shorter time constants are incorporated. Considerably more details on these simulations are contained in the Supporting Information 3.7.

*Quantum-mechanical modelling* The quantum-mechanical calculations were performed using Gaussian03 [193] applying the B3LYP [194] hybrid functional and a 6-31G(d,p) basis set. Total energies were extracted from the last step in the geometry optimizations. Note that we encountered serious convergence problems, when optimizing the geometry of planarized TIPS-pentacene protonated at one of the central C-atoms. The way we circumvented these problems is described in the Supporting Information 3.7.

# Acknowledgements

We thank A. Fian for growing the pentacene films of the transistors exposed to HCl vapour, H. Brandner for reproducing the findings of Ref. [184], and Christian Slugovc as well as Thomas Grieï¿½er for stimulating discussions. Financial support by the Austrian Science Fund (FWF) (P 19959-N20) is acknowledged. Supporting Information is available online from Wiley InterScience or from the authors.

## 3.7 Supporting information

As especially the growth of the T-SC/SA layers is impacted severely by the very details of the fabrication process (especially by minute changes of the water concentration during film growth), we considered it appropriate to provide a relatively detailed description of the applied methodologies.

### Device fabrication

(this is a significantly extended version of the description in the main manuscript) As substrates (serving also as gate electrodes), we used doped silicon wafers with thermally grown oxides with thicknesses $d_{ox} = 102.2\,\text{nm}$, $d_{ox} = 147.5\,\text{nm}$, $d_{ox} = 152.0\,\text{nm}$, and $d_{ox} = 245.0\,\text{nm}$ pre-cut into 2 cm x 2 cm pieces. Which of the oxides has been used in a certain experiment is specified in the figure captions in the main text.

The waver with $d_{ox} = 102.2\,\text{nm}$ was boron doped (company: Silchem) and supplied with a plastic coating on the oxide for protection. To remove this plastic coating, we cleaned them in an ultrasonic bath in ultra-pure water for 2 min, cleaned it with a cleaning liquid (Photonic Cleaning Technology, type: First Contact) that was first brushed onto the waver and then left to dry for ca. 15 minutes. The resulting film was then removed by ultrasonic treatment in ultra-pure water produced with a cleaning system (company: Millipore, type: Simplicity 185; and the resulting specific resistance was in the range of MΩcm) for 2 min. Finally we dried the substrates with carbon dioxide gas. The other wavers were phosphorus doped (company: Siegert Consulting) and were delivered without any coating on the oxide.

As a next step, all substrates were cleaned in a $CO_2$ gas stream and, finally, the oxide surfaces of the substrates were cleaned and activated by an oxygen plasma etching process using a commercial set-up (company: diener electronic, type: Femto). First the plasma etching chamber was evacuated with a scroll pump (company: Varian, type: SH110) to a pressure of 0.2 mbar. In this context it should be mentioned that the use of an oil-free pump (like a scroll pump) is advantageous, as in XPS experiments performed to study the composition of the wafer surface after the plasma etching step, we found

fluorine on the $SiO_x$ surface when using a rotary vane pump most likely due to decomposed pump oil. Subsequently, the chamber was flooded with oxygen (company: Air Liquide, type: Alphagaz oxygen) setting the flow-meter to a value of 90 at an (over) pressure of 2.5 bar. Before starting the plasma etching process, we then waited until the pressure inside the chamber silized at 0.3 mbar. The frequency of the high frequency generator was 40 kHz and we performed the plasma etching at a power of 100 W for 30 s. After the plasma etching process and the water sonication, the substrates were again cleaned with $CO_2$ gas.

Afterwards, we put them into cleaned glass containers (for a detailed description of the cleaning procedure see below) filled with ultra-pure water, did an ultrasonic treatment for 2 min and left them inside the bottles for about 25 min. This rendered the oxide surfaces of all samples highly hydrophilic lowering the contact angle of $H_2O$ to below 10 ï¿½, the limit of our contact-angle measurement set-up (vide infra). This is insofar important as (i) before the plasma etching the contact angles of the different wafer batches differed considerably and (ii) the resulting high concentration of -OH groups on the waver surface is beneficial for the docking of silanes when growing the functional monolayers.

Meanwhile, other glass containers (which we had been held at 80 ï¿½C least over night) to be used for T-SC/SA layer growth were transferred into the glove box while still being hot. Note: We observed increased thicknesses of the T-SC/SA layers when transferring cooled down glass containers, presumably due to the adsorbed water at the inner walls of the containers, as minute amounts of water significantly impact the layer growth. Inside the glove box ($H_2O$ and $O_2$ concentration $< 1$ ppm), each of the substrates was put into a separate glass containers that was filled with 10 ml highly dry toluene (water content of about 7 ppm measured with Karl Fischer Titration). To that we added 10 $\mu l$ of the T-SC/SA solution, which is a 50 vol % mixture of T-SC/SA molecules and toluene (company: ABCR, product number: AB129108) and let the layer grow for 16 h. After this time, we put the substrates into glass containers with 6 ml fresh highly dry toluene, sealed the containers, transferred them out of the box, sonicated them for 2 min, and

rinsed them with fresh toluene (company: Sigma-Aldrich, product number: 34866). This toluene had a water content of about 29 ppm measured with Karl Fischer Titration. Then we dried the samples using $CO_2$ gas and annealed them for 30 min at about 100 ï¿½C at a pressure of about 0.6 mbar. Between the annealing process and pentacene evaporation as well as between pentacene evaporation and gold deposition the substrates were in air and exposed to light for several hours.

The active layer material pentacene (company: tokyo chemical industry, product number: P0030) was vacuum deposited under high-vacuum conditions (base-pressure in the range of $10^{-6}$ mbar typically some days after growing the T-SC/SA layer. The first 5 nm were deposited at a rate of 0.02 ï¿½/s and the following 30 nm at a rate of 0.1 ï¿½ /s, as measured with a quartz microbalance. During pentacene-growth, the substrates were held at a temperature of 60 ï¿½C. Alternatively, TIPS-pentacene films were deposited from a 1 wt % solution of TIPS-pentacene (company: Sigma-Aldrich, product number: 716006-1G) in toluene (company: Sigma-Aldrich, product number: 34866). The films were fabricated by spin coating (company: Chemat Technology, type: KW-4A) in air with the substrate heated to 60 ï¿½C using an IR lamp (spin parameters set to: 2000 rpm for 18 s and 4000 rpm for 20 s). The 50 nm thick (measured with a quartz microbalance) gold (company: Oegussa, quality: fine gold plate) source and drain electrodes were produced at a pressure in the range of $10^{-6}$ mbar in a home-built evaporation set-up operated inside an Ar glove-box. For technical reasons, the manometer had to be located outside the glove box, i.e., close to the turbomolecular pump. Four transistors were fabricated on each substrate.

**Cleaning process for glass containers used to grow T-SC/SA layers**

(as mentioned above, the 'state' of the glass bottles has a distinct influence on the growth of the T-SC/SA layer)We always cleaned 19 glass containers (company: Bartelt, product number: 9.072 303) with 32 ml Hellmanex (company: Hellma, product number: 9-307-010-507) in 1.6 l deionized water with an ultrasonic bath for 25 min. Then we emptied the bucket containing the

glasses, refilled it with deionized water, emptied every single glass container, cleaned the bucket with deionized water, put the glass containers back into the bucket and filled it with deionized water until the glass containers were covered with water. Now we did the ultrasonic treatment for 7 min and repeated the whole process two times, but without the bucket cleaning step. As a final cleaning step, every glass bottle was rinsed with ultra-pure water and stored in an oven at 80 ï¿½C at least overnight. The ultra-pure water was produced with a cleaning system (company: Millipore, type: Simplicity 185) and the resulting specific resistance was in the range of MΩcm.

### Details on the chosen measurement procedure

Before measuring the device characteristics, the pentacene layer around the source and drain areas of the four devices located on each substrate is mechanically removed. This reduces the apparent gate current by up to two orders of magnitude in our common gate devices. To measure the electronic characteristics of the transistors, we used a Keithley 2636A dual source-meter controlled with a home-made software. We started the transfer sweeps at positive gate bias, reduced $V_{GS}$ in steps of $-2$ V, setting the delay time, which is the time between applying $V_{GS}$ and the measurement of $I_D$, to 0.1 s. It should, however, be noted that this is not in all cases the actual time between two measurement, because the integration time for every measurement point is set automatically by Keithley firmware to obtain a sufficient signal to noise ratio. Therefore, at very small currents, significantly increased measurement times were applied. $V_{GS}$ was decreased until we reached the most negative reported gate bias (set to a value that did depend on $V_{th}$). Then $V_{GS}$ was again increased to the highest positive value reported in the figures. The given device parameters were always determined for the sweep from positive to negative $V_{GS}$. $V_{DS}$ was $-2$ V for the data reported in Fig. 3.8 and Fig. 3.10, and -60 V for the data in Fig. 3.11. The very low $V_{SD}$ in the first case was chosen to maximize the linear region for data extraction, while in the TIPS-pentacene devices we applied a larger $V_{DS}$ to avoid too small currents. All measurements were performed under ambient light inside a glove box.

**Additional data for oxide thickness depended transfer curves**

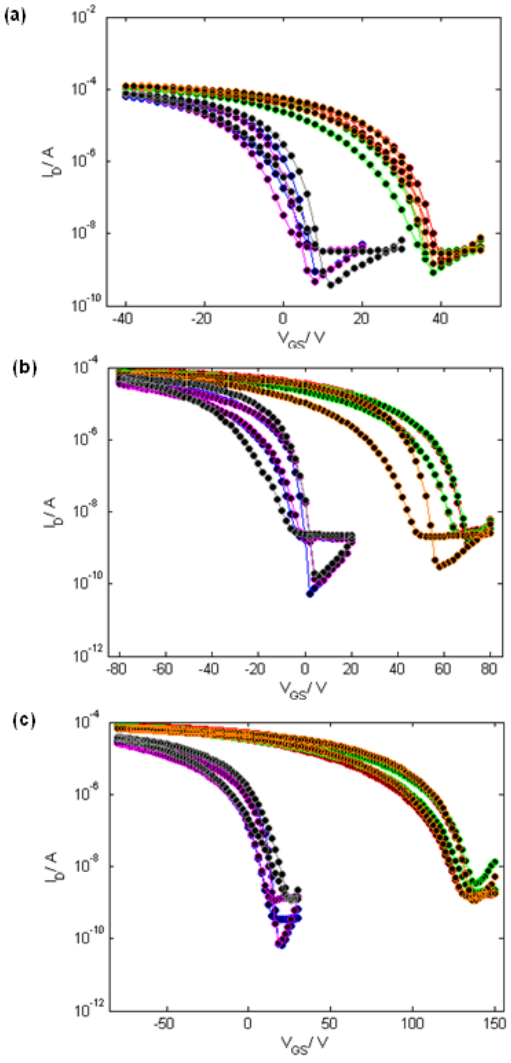


Figure 3.8: Additional transfer characteristics of pentacene based devices including a T-SC/SA semiconductor-dielectric interface layer with nominal (actual) oxide thicknesses of $d_{ox} - n = 100\,\text{nm}$ ($d_{ox} = 102.2\,\text{nm}$), $d_{ox} - n = 150\,\text{nm}$ ($d_{ox} = 147.5\,\text{nm}$), and $d_{ox} - n = 250\,\text{nm}$ ($d_{ox} = 245.0\,\text{nm}$). High positive $V_{th}$ correspond to devices before and low $V_{th}$ to devices after exposure to a flow of pure $NH_3$ gas. The source-drain voltage ($V_{DS}$) was set to -2 V. The increased hysteresis in the bottom plot is primarily a consequence of the extended measurement range

Table 3.3: Additional device parameters of (Si|SiOx|T-SC/SA|pentacene|Au) transistors as a function of the oxide thicknesses ($d_{ox}$) before (top table) and after $NH_3$ exposure (bottom table). Threshold/onset voltages have been derived with different methods and are denoted as, $V_{ELR}$, $V_{SD}$, and $V_{SDL}$ (details see main paper), mobilities ($\mu$), and on-to-off ratios ($I_{on}/I_{off}$) are reported. $I_{off}$ is defined as the drain current when the gate voltage equals $V_{on}$ and $I_{on}$ is the current for $V_{GS}$ equaling $V_{on} - 40\,\mathrm{V}$. The last line for each oxide thickness gives the average values.

| $d_{ox}$ | $c_{ox}$ | $V_{ELR-1}$<br>$V_{ELR-2}$<br>$V_{ELR-3}$ | $V_{SD-1}$<br>$V_{SD-2}$<br>$V_{SD-3}$ | $V_{SDL-1}$<br>$V_{SDL-2}$<br>$V_{SDL-3}$ | $\mu_1$<br>$\mu_2$<br>$\mu_3$ | $(I_{on}/I_{off})_1$<br>$(I_{on}/I_{off})_2$<br>$(I_{on}/I_{off})_3$ |
|---|---|---|---|---|---|---|
| | | $V_{ELR}$ | $V_{SD}$ | $V_{SDL}$ | $\mu$ | $I_{on}/I_{off}$ |
| $[nm]$ | $[\frac{nF}{cm^2}]$ | $[V]$ | $[V]$ | $[V]$ | $[\frac{cm^2}{Vs}]$ | $[10^3]$ |
| 102.2 | 34.8 | 22 | 29 | 40 | 0.22 | 20 |
| | | 16 | 19 | 36 | 0.24 | 30 |
| | | 22 | 27 | 38 | 0.25 | 40 |
| | | 20 | 25 | 38 | 0.24 | 30 |
| 147.5 | 23.0 | 40 | 46 | 70 | 0.13 | 6 |
| | | 42 | 46 | 70 | 0.11 | 5 |
| | | 36 | 39 | 56 | 0.13 | 50 |
| | | 39 | 44 | 65 | 0.12 | 20 |
| 245.0 | 14.1 | 88 | 96 | 136 | 0.14 | 2 |
| | | 85 | 94 | 136 | 0.13 | 0.8 |
| | | 96 | 103 | 136 | 0.13 | 3 |
| | | 90 | 98 | 136 | 0.13 | 2 |

| $d_{ox}$ | $c_{ox}$ | $V_{ELR-NH3-1}$<br>$V_{ELR-NH3-2}$<br>$V_{ELR-NH3-3}$<br>$V_{ELR-NH3}$ | $V_{SD-NH3-1}$<br>$V_{SD-NH3-2}$<br>$V_{SD-NH3-3}$<br>$V_{SD-NH3}$ | $V_{SDL-NH3-1}$<br>$V_{SDL-NH3-2}$<br>$V_{SDL-NH3-3}$<br>$V_{SDL-NH3}$ | $\mu_{NH3-1}$<br>$\mu_{NH3-2}$<br>$\mu_{NH3-3}$<br>$\mu$ | $(I_{on}/I_{off})_{NH3-1}$<br>$(I_{on}/I_{off})_{NH3-2}$<br>$(I_{on}/I_{off})_{NH3-3}$<br>$I_{on}/I_{off}$ |
|---|---|---|---|---|---|---|
| $[nm]$ | $[\frac{nF}{cm^2}]$ | $[V]$ | $[V]$ | $[V]$ | $[\frac{cm^2}{Vs}]$ | $[10^3]$ |
| 102.2 | 34.8 | −5 | 0 | 8 | 0.20 | 40 |
| | | −7 | −1 | 6 | 0.25 | 70 |
| | | −3 | 2 | 10 | 0.21 | 70 |
| | | −5 | 1 | 8 | 0.22 | 60 |
| 147.5 | 23.0 | −17 | −11 | 2 | 0.10 | 90 |
| | | −14 | −9 | 4 | 0.08 | 100 |
| | | −17 | −7 | 4 | 0.14 | 80 |
| | | −16 | −9 | 3 | 0.11 | 90 |
| 245.0 | 14.1 | −8 | 0 | 18 | 0.12 | 70 |
| | | −11 | −1 | 18 | 0.10 | 40 |
| | | −8 | −4 | 24 | 0.14 | 5 |
| | | −9 | −3 | 20 | 0.12 | 40 |

**Details on the x-ray reflectivity measurement**

The x-ray reflectivity measurements were performed on a Bruker diffractometer (type: D8 Discover) using $CuK_{\alpha}$-radiation from a sealed tube. For the primary and secondary side optics and the receiving slit a sequence of 0.05 mm, 0.1 mm and 0.1 mm was used. On the secondary side, an automatic absorber is mounted. To analyze the data, we fitted them using WinGixa [187], which is an implementation of Parratt's recursive algorithm [188] including interface, $\sigma_{ox}$, and surface root mean square roughness, $\sigma_{T-SC/SA}$, according to the approach of Nevot and Croce [189]. The kink around 2.5 $nm^{-1}$ originates from the interference within the T-SC/SA layer, while the fast os-

cillating fringes (see inset of Fig. 3.9) are a consequence of interference within the $SiO_x$ layer. To obtain satisfactory agreement between measurements and fits (see Experimental section 3.6), the T-SC/SA layers had to be modeled as a double layer structure, i.e. as consisting of two layers with different electron density. The corresponding thicknesses are denoted as $d_{T-SC/SA-1}$ and $d_{T-SC/SA-2}$. Thus, in total a three-layer structure has been used as a model to fit the experimental data.

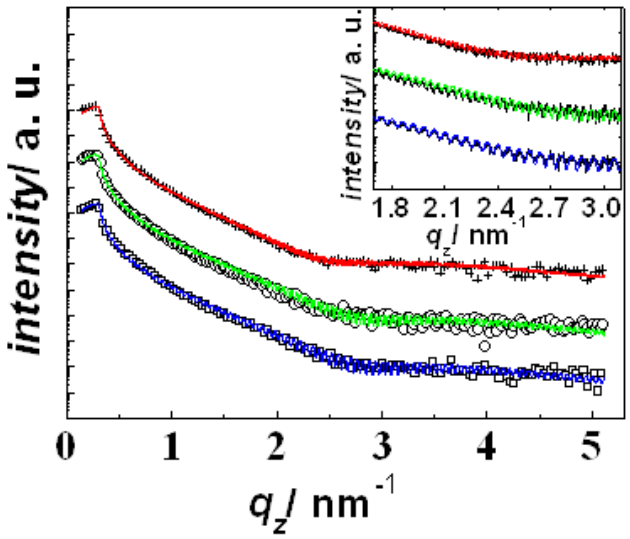


Figure 3.9: Specular x-ray reflectivity measurements for three samples with different $d_{ox}$ (data points: squares: $d_{ox} = 102.2\,\text{nm}$, circles: $d_{ox} = 147.5\,\text{nm}$, +: $d_{ox} = 245.0\,\text{nm}$; and corresponding fit curves). The inset shows a zoom into a smaller $q_z$ range displaying the interference fringes due to the $SiO_x$ layer (curves shifted for clarity).

### Contact angle measurements

The contact angles were measured with a drop shape analysis system (company: Kruess GmbH, type: DSA 100) using deionized water and diiodomethane (company: Sigma-Aldrich, product number: 158429) as test liquids (drop volume $3\,\mu\text{l}$). Based on the method by Owens Wendt [190], the surface free energy per unit area $E_s$ of the T-SC/SA layers were calculated automatically. The contact angles were obtained by means of the sessile drop method and

were measured within 2 seconds.

Table 3.4: Diiodomethane $\Theta_d$ and water $\Theta_w$ contact angles for two independent series for T-SC/SA layers grown on substrates with three different oxide layer thickness $d_{ox}$ and the out of that calculated surface free energy $E_s$. The values are the standard deviations to the corresponding values derived from five independent measurements.

| $d_{ox}$ | $\Theta_{d1}$<br>$\Theta_{d2}$<br>$\Theta_d$ | $\sigma_{d1}$<br>$\sigma_{d2}$<br>$\sigma_d$ | $\Theta_{w1}$<br>$\Theta_{w2}$<br>$\Theta_w$ | $\sigma_{d1}$<br>$\sigma_{d2}$<br>$\sigma_d$ | $E_{s1}$<br>$E_{s2}$<br>$E_s$ | $\sigma_{d1}$<br>$\sigma_{d2}$<br>$\sigma_d$ |
|---|---|---|---|---|---|---|
| $[nm]$ | $[\frac{1}{2}]$ | $[\frac{1}{2}]$ | $[\frac{1}{2}]$ | $[\frac{1}{2}]$ | $[\frac{mJ}{m^2}]$ | $[\frac{mJ}{m^2}]$ |
| 102.2 | 36.1 | 1.0 | 66.2 | 0.6 | 50.2 | 0.3 |
| | 34.8 | 0.7 | 57.7 | 1.1 | 55.0 | 0.3 |
| | 35.5 | | 62.0 | | 52.6 | |
| 147.5 | 37.2 | 1.1 | 68.6 | 0.8 | 48.7 | 0.3 |
| | 35.6 | 0.3 | 63.1 | 0.9 | 51.9 | 0.1 |
| | 36.4 | | 65.9 | | 50.3 | |
| 245.0 | 36.5 | 0.8 | 70.2 | 0.2 | 48.2 | 0.2 |
| | 35.6 | 0.7 | 62.1 | 1.5 | 51.6 | 0.3 |
| | 36.4 | | 66.2 | | 49.9 | |

### $NH_3$ gas exposure (experimental procedure)

We put our devices in a homemade measurement cell and flooded the cell with $NH_3$ gas (company: Linde Gas, product number: UN1005), for either 30 min (data in Fig. 3.8) or 1 min (data in Fig. 3.10).The $NH_3$ pressure was 1.5 bar and the volume flow was approximately 8 $lh^{-1}$. After the $NH_3$ exposure, we flooded the cell with argon gas (company: Air Liquide, type: ALPHAGAZ ARGON 1) until we could not detect ammonia at the gas outlet of the measurement cell. *Hazard warning! $NH_3$ is highly toxic, thus experiments should always be performed in a fume hood using appropriate gloves and protective glasses!*

### HCl vapor exposure (experimental procedure)

We put the ready-made devices over a beaker filled with fuming hydrochloric acid (company: Sigma-Adrich, product number: 30721) for 1 min. Hazard warning! HCl vapor is very acidic thus experiments should always be performed in a fume hood using appropriate gloves and protective glasses!

### Additional characteristics for the exposure of (Si|$SiO_x$|pentacene|Au) devices first to hydrochloric acid vapor (HCl) and afterwards to ammonia gas ($NH_3$)

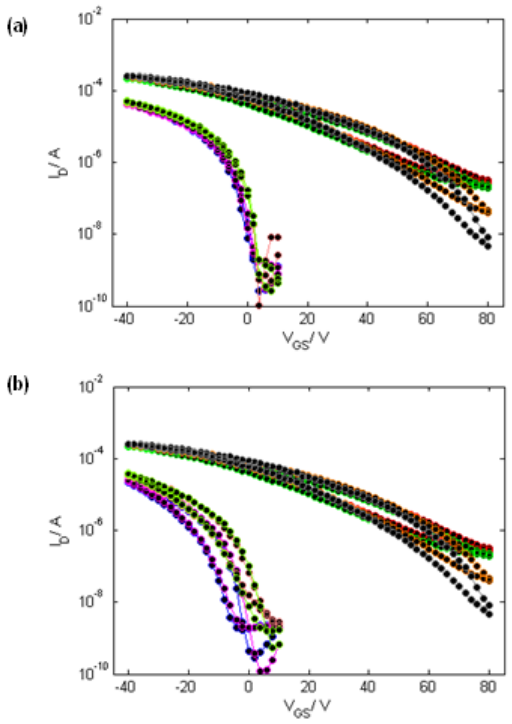


Figure 3.10: (a) Transfer characteristics of different devices before (low $V_{th}$) and after exposure to HCl vapor (high $V_{th}$); (b) transfer characteristics of the same devices after HCl exposure (high $V_{th}$) and after subsequently $NH_3$ (low $V_{th}$) exposure in the bottom (Fig. 3.6 (b)).

### Additional data on TIPS-pentacene devices exposed to HCl vapor or containing T-SC/SA layers

TIPS-pentacene devices containing a T-SC/SA layer at the interface between the organic semiconductor and the $SiO_x$ dielectric, as well as 'conventional' TIPS-pentacene devices exposed to HCl vapor show clearly negative $V_{th}$ and $V_{on}$ in contrast to pentacene based devices (see Fig. 3.8 and Fig. 3.10).

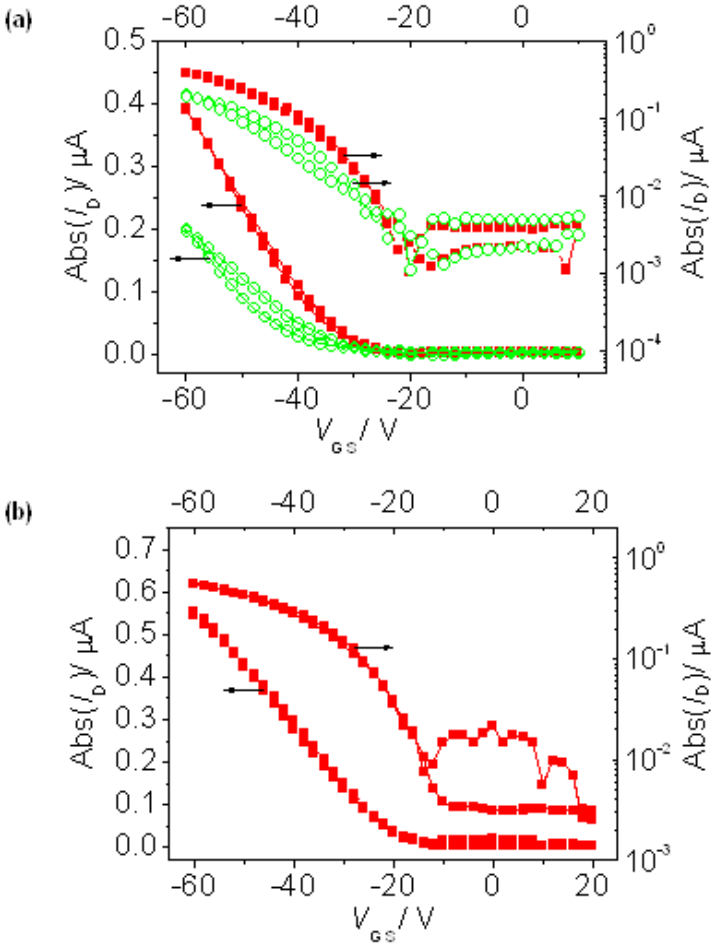


Figure 3.11: (a) Transfer characteristic of a (Si|$SiO_x$|TIPS-pentacene|T-SC/SA|Au) device with $d_{ox} = 152\,\text{nm}$ before (solid squares) and after exposure to HCl vapor (open circles). (b) Transfer characteristic of a (Si|$SiO_x$|T-SC/SA|TIPS-pentacene|Au) devices with $d_{ox} = 152\,\text{nm}$. $V_{DS}$ is set to $-60\,\text{V}$.

In this context, it should be mentioned that the investigated TIPS-pentacene films are preferentially aligned in the (001) and (011) orientation as can be inferred from the thin-film x-ray diffraction data shown in Fig. 3.12. This means that the molecular backbones lie essentially parallel to the substrate surface ((001) orientation) or are somewhat inclined (011 orientation), which is clearly different from the preferential orientation of pentacene on $SiO_x$, where the molecules typically stand (close to) upright [195]. This can cause differences in the diffusion of gasses like HCl through the active layer. Considering, however, (i) that no acid doping is observed also for acidic SAMs directly in the channel region, (ii) that the active regions are very thin, which should allow HCl to diffuse right to the channel independent of crystallite orientation and (iii) that there should be a massive impact on the transistor characteristics also if only the regions of the OSC layer close to the surface were doped and thus made conducting, it appears safe to conclude that TIPS-pentacene is not prone to acid doping (at least not when using HCl or T-SC/SA as the reagents)

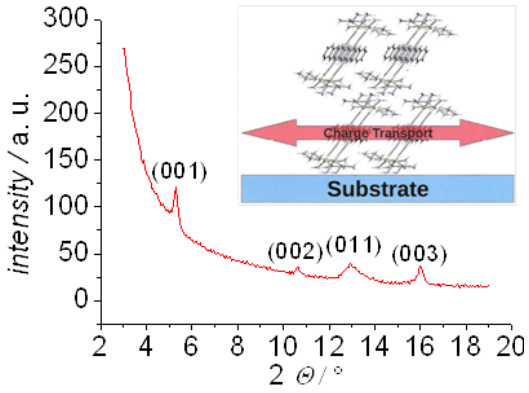


Figure 3.12: $\Theta/2*\Theta$) scan of a pentacene layer spin-coated from toluene with the substrate held at 60 ï¿½C. The inset (courtesy of Armin Moser) shows the schematic structure for the (001) orientation.

### Quantum-mechanical simulations

The quantum-mechanical calculations were performed using Gaussian03 [193] applying the B3LYP [194] hybrid functional and a 6-31G(d,p) basis set. To-

tal energies were extracted from the last step in the geometry optimizations. Note that we encountered serious convergence problems, when optimizing the geometry of planarized TIPS-pentacene protonated at one of the central C-atoms. To circumvent these problems, we first performed a geometry optimization with loose convergence criteria (which did converge), then increased the convergence criteria to the standard values and reduced the step-size in the optimization process. Even this procedure yielded only partially converged geometries (i.e., not all of the geometry convergence criteria could be met). This problem prevailed when changing the optimizer to the Newton algorithm. As the differences between all obtained total energies (fully converged with loose convergence criteria, and partially converged with standard criteria) were smaller than 1 meV, they were eventually accepted as the appropriate values for planarized TIPS-pentacene protonated at one of the central C-atoms. GaussView 2.1 [196] was used to plot the molecular structure in Fig. 3.13.

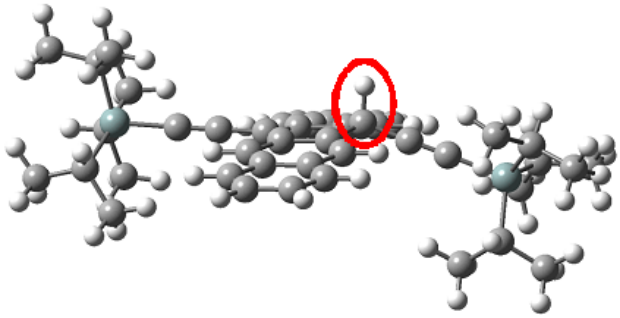

Figure 3.13: (a) B3LYP/6-31G(d,p) optimized gas-phase geometry of TIPS-pentacene protonated at the central position

*Calculations of the reaction enthalpies of proton transfer between T-SC/SA or HCL and pentacene* Calculations on isolated protonated/deprotonated pentacene, HCL, and TSA molecules yield energy differences between 4.0 eV and 4.7 eV (not correcting for basis-set superposition errors). These energies, however, severely overestimate the actual situation, as they do not consider the Coulomb attraction between the proton and the acid residue and also neglect medium polarization effects, which additionally significantly stabilize

the charge-separated situation. Describing the actual situation in the bulk is, however, clearly beyond the scope of the present manuscript and is severely complicated by the unknown details of the interface structure and by DFT's tendency to overestimating charge delocalization.

### Methodology for drift-diffusion based simulations

(this is a significantly extended version of the description in the main manuscript)

The numerical model to describe device characteristics is a two-dimensional drift-diffusion approach as described in Ref. [147] with special boundary conditions at the source and drain electrodes. Charge carrier injection occurs via thermionic emission and tunneling through a potential barrier (given by the image charge model) in WKB approximation and is corrected by an interface recombination current [191]. The corresponding system of equations containing the Poisson equation, the drift-diffusion current density equation, and the continuity equation with appropriate boundary conditions is solved self-consistently on a non-regular two-dimensional grid [147] using an implicit time integration.

During the simulation, the device geometry, the hole injection barrier of 0.47 eV from gold into pentacene [192], and the dielectric constants of pentacene ($\epsilon = 3.4$) and $SiO_2$ ($\epsilon = 3.9$) are kept fixed. To describe the different onset voltages at different device thicknesses, a fixed negative interface charge distribution with a density of 1.5 x $10^{17}$ $em^{-2}$ and an interface dipole layer with a density resulting in a potential shift of 31 V were placed at the pentacene-$SiO_x$ interface. The latter were realized by placing two oppositely charged space charge layers with an areal charge density of 2.0 x $10^{19}$ $em^{-2}$ at a distance of 3 ï¿½.

To further account for the shape of the I-V curves obtained in the experiments two types of traps are considered: (i) The occurrence of a hysteresis (cf. Fig. 3.13) is simulated by including bulk traps. The density $p_{trap}(x, y)$ of trapped holes is self-consistently determined for each time step using the rate equation $dp_{trap}(x, y)/dt = 1/\tau'_{trap} p(x, y) - 1/\tau'_{detrap} p_{trap}(x, y)$, where p(x,y) denotes the hole density and $\tau'_{trap}$ and $\tau'_{detrap}$ are the trapping

and detrapping time constants, respectively. The latter are of the order of seconds; the used numerical values are listed in Table 3.5. For the bulk traps we assume that the available number of trapping sites far exceeds the number of trapped carriers for the considered time scales (i.e., it does not need to be considered explicitly) (ii) To properly account for the shape of the transfer-characteristics in the sub-threshold region (cf. Fig. 3.13), additional interface traps are incorporated [156]. To prevent a possible influence on the hysteresis, they are treated as being always in the steady state, which is a reasonable assumption as long as the associated time constants are clearly shorter than the acquisition times for each measurement point. A simulation including a single trap level is not sufficient to capture the shape of the transfer characteristic at gate voltages close to the threshold-voltage (see next section). This deficiency can be mended by assuming a trap distribution rather than a single trap level. The actual density of trapped carriers $p_t$ is self-consistently determined depending on the mobile carrier density at the interface and the width of the trap distribution. For the sake of simplicity, the trap distribution is assumed to be rectangular shaped, to have a width $\sigma = 0.1\,\mathrm{eV}$, and to be shifted by $A = 0.1\,\mathrm{eV}$ with respect to the hole transport level $E_{HOMO}$. I.e., the trap density can be written as $D_t(E) = p_{t0}/\sigma\Theta(E - (E_{HOMO} + A))\Theta(E_{HOMO} + A + \sigma - E)$ with $\Theta(E')$ denoting the Heaviside function and $p_{t0}$ the total number of traps. To describe the density of trapped carriers, $p_t$, we solve the following differential equation: $dp_t(x,y)/dt = 1/\tau_{trap}(p_{t0} - p_t)/p_{t0}p(x,y) - 1/\tau_{detrap}p_t(x,y)$, where the term $(p_{t0} - p_t)/p_{t0}$ is introduced to provide an upper limit of the total number of trapped carriers; in the steady state one only needs to know the ratio $\tau_{detrap}/\tau trap$. For the above described rectangular density of states, the latter becomes: $\tau_{detrap}/\tau_{trap} = exp[(\sigma(1 - p_t/p_{t0}) + A)q/k_BT]$, where $k_B$ is the Boltzmann constant, and $T = 298\,\mathrm{K}$ the temperature. The above two equations are solved self-consistently.

Table 3.5: Parameters used to simulate the transfer characteristics for all oxide thicknesses $d_{ox}$. Mobility, $\mu$; acquisition time per data point, $t$; trapping time constant, $t_{trap}$, and detrapping time constant, $t_{detrap}$, of the long-lived bulk traps; density of the short-lived interface traps, $p_{t0}$. The values of the hole mobility and the density of interface traps of the 100 nm device differ somewhat from the corresponding value in thicker devices. The differently pretreated substrate in the 100 nm device presumably has interface properties that deviate from the 150 nm and 250 nm devices and, thus, alter interface-determined quantities such as mobility and interface trap density. The deviation between the intrinsic mobility used here and the effective mobility extracted from the experiments will be discussed in section 'Detailed discussion of the impact of traps on the device characteristics'.

| $d_{ox}$ $[nm]$ | $\mu$ $[\frac{cm^2}{Vs}]$ | $t$ $[s]$ | $p_{t0}$ $[\frac{1}{m^2}]$ | $\tau_{trap}$ $[s]$ | $\tau_{detrap}$ $[s]$ |
|---|---|---|---|---|---|
| 100 | 0.34 | 0.1 | $3.2 * 10^{16}$ | 11 | 4 |
| 150 | 0.21 | 0.1 | $4.3 * 10^{16}$ | 11 | 4 |
| 250 | 0.23 | 0.1 | $4.3 * 10^{16}$ | 11 | 4 |

### Comparison between measured and calculated transfer characteristics

The simulated curves are in an excellent agreement with the measured ones (cf., Fig. 3.14), in particular, considering that only a few degrees of freedom have been taken to account in the simulations. Reasons for the residual mismatch between theory and experiment could possibly be (i) more sophisticated trap-distributions, (ii) the varying data acquisition time of the Keithley source meter at low device currents (vide supra, resulting in an overestimation of the hysteresis at small currents), and (iii) mobility degradation that affects the high current region. The latter gives rise to an overestimation of IDS for large negative $V_{GS}$, which could either be accounted for by a $V_{GS}$-dependent mobility or assuming a mobility that decreases close to the interface [146], where charge carriers are more strongly accumulated at large negative $V_{GS}$.

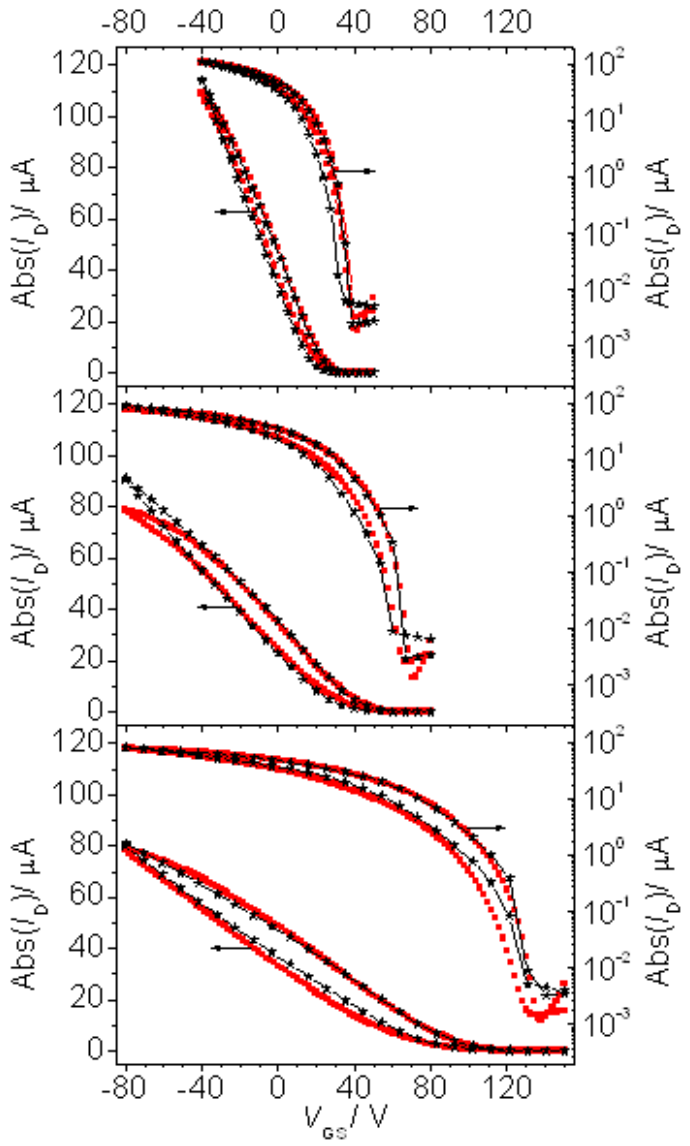


Figure 3.14: . Comparison between simulated (black stars) and measured (red squares) transfer characteristics (from top to bottom: $d_{ox-n} = 100\,\text{nm}$, $d_{ox-n} = 150\,\text{nm}$ and $d_{ox-n} = 250\,\text{nm}$).

**Detailed discussion of the impact of traps on the device characteristics**

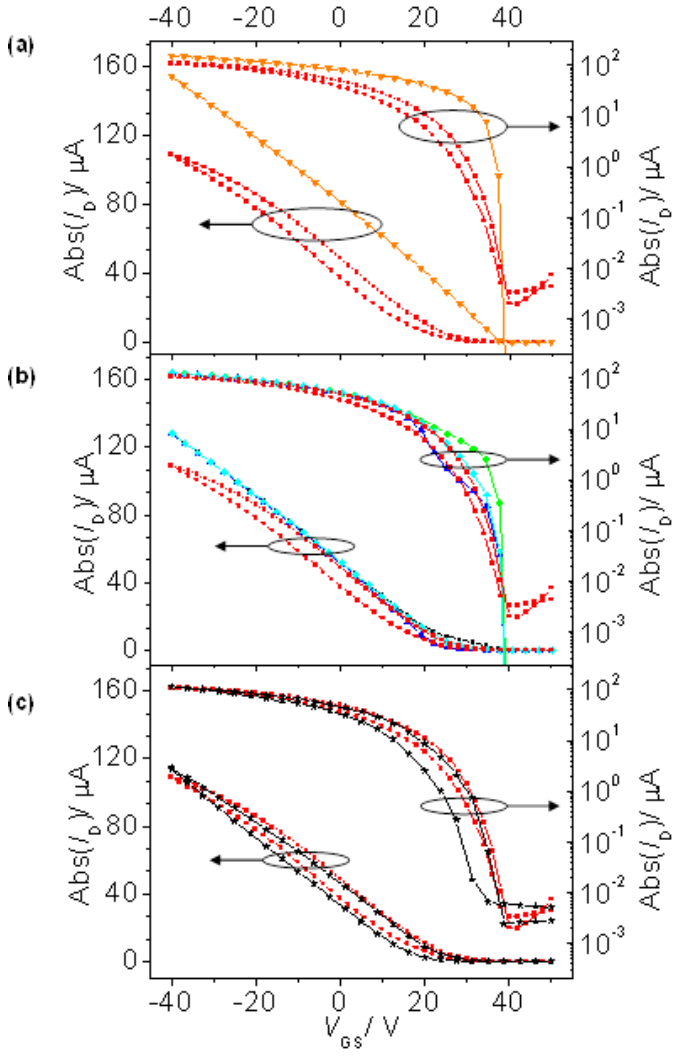


Figure 3.15: Linear (left) and semi-logarithmic (right) plot of simulated transfer curves for the $d_{ox} = 100\,\text{nm}$ device assuming fixed intrinsic mobilities and interface charge layers upon increasing the number of considered effects. The experimental curves are shown as red solid squares for comparison. (a) considering no further effects; (b) comparison between interface trap distributions: a single interface trap level at 0.1 (green solid circles) and 0.2 eV (blue solid triangles) above the transport level and a constant interface trap density between 0.1 eV and 0.2 eV above the hole transport level (cyan solid diamond). (c) 'final' model including the rectangular interface trap density from b) and bulk traps as described in section 12 black solid stars()

While the general observation of a gate-oxide thickness dependent $V_{th}$ can be consistently modeled by the space charge and dipole densities as discussed extensively in the main manuscript, the detailed shapes of the transfer characteristics are not reproduced in a 'straightforward' calculation assuming a fixed carrier mobility and disregarding traps. This becomes obvious from a comparison between Fig. 3.14 and Fig. 3.15 (a). To further illustrate that, Fig. 3.7 shows the evolution of the transfer-characteristics upon including an increasing amount of effects. As discussed in the main text, the switch-on voltage is quantitatively captured by the charge distributions at the dielectric-pentacene interface.

Including various types of traps, the full characteristics can, however, be recovered even regarding the hysteresis and a suitable off-current. Which details of the characteristics are affected by which physical effect can be seen in Fig. 3.15, where we successively increase the complexity of the applied model. Fig. 3.15 (a) compares the experimental transfer characteristics with the one obtained in the simulations assuming a constant mobility of $\mu = 0.34\,\mathrm{cm}^2/(\mathrm{Vs})$. The latter is somewhat larger than that extracted from the experimental data. It can be regarded as an 'intrinsic' mobility that is determined by the transport properties of pentacene and by shallow traps that are filled/emptied at time-scales much faster than those relevant for the experiment. It is necessary to start with such a large value of $\mu$, as the 'effective' mobility will be reduced when introducing traps in the following steps. A satisfactory agreement between theory and experiment is also not achieved, when using the experimentally determined effective mobility.

The correct description of the shape of the curves (in particular the subthreshold swing) requires the incorporation of interface traps [192]. It is important to note here the quality of agreement needs to be assessed both from the linear as well as from the semi-logarithmic plot. As illustrated in Fig. 3.15 (b), the inclusion of a single level of short-lived traps causes the desired reduced slope of the I-V curve in the sub threshold region (circles and triangles). Upon inspecting the curves in the logarithmic plot (corresponding right panel) it , however, becomes evident that a single trap level is even qualitatively not sufficient to reproduce the measurements due to a marked

kink, e.g., at $V_{GS} = 30\,\mathrm{V}$ for a 0.1 eV trap. Rather, as shown as diamonds in Fig. 3.15 (b), a distribution of traps can reproduce the shape satisfactorily, since the resulting 'superposition' of trap levels smears out the kinks associated with a single trapping energy. Finally, the incorporation of additional, long-lived traps gives rise to a hysteresis (Fig. 3.15 c). Regarding the origin of residual deviations between theory and experiment see the discussion at the end of section 'Comparison between measured and calculated transfer characteristics'.

# Bibliography


[1] Y. Nishi and R. Doering. *Handbook of Semiconductor Manufacturing Technology*. CRC Press, 2007.

[2] S. M. Sze. *Physics of Semiconductors*. Wiley, New York, 1981.

[3] E. D. Williams, R. U. Ayres, and M. Heller. *Environ. Sci. Technol.*, 36:5504–5510, 2002.

[4] P. M. Cox, R. A. Betts, C. D. Jones, S. A. Spall, and I. J. Tottertell. *Nature*, 409:184–187, 2000.

[5] M. Gruber, B. A. Stickler, G. Trimmel, F. Schuerrer, and K. Zojer. *Org. Electron.*, 11:1999–2011.

[6] M. Gruber, F. Schürrer, and K. Zojer. *Org. Electron.*, 13:1887–1899, 2012.

[7] S. J. Ausserlechner, M. Gruber, R. Hetzel, H. G. Flesch, L. Ladinig, L. Hauser, A. Haase, M. Buchner, R. Resel, F. Schürrer, B. Stadlober, G. Trimml, K. Zojer, and E. Zojer. *Phys. Status Solidi A*, 209:181–192, 2012.

[8] P. Ravirajan, A. M. Peiro, M. K. Nazeeruddin, M. Graetzel, D. D. C. Bradley, J. R. Durrant, and J. Nelson. *J. Phys. Chem. B*, 110:7635–7639, 2006.

[9] J. Boucle, P. Ravirajan, and J. Nelson. *J. Mat. Chem.*, 17:3141–3153, 2007.

[10] J. Boucle, S. Chyla, M. S. P. Shaffer, J. R. Durrant, D. D. C. Bradley, and J. Nelson. *Adv. Func. Mat.*, 18:622–633, 2008.

[11] S. Tepacevic, S. B. Darling, N. M. Dimitrijevic, T. Rajh, and S. J. Sibener. *Small*, 5:1776–1783, 2009.

[12] K. Shankar, G. K. Mor, H. E. Prakasam, O. K. Varghese, and C. A. Grimes. *Langmuir*, 23:12445–12449, 2007.

[13] B. R. Saunders and M. L. Turner. *Advances in Colloid and Interface Science*, 138:1–23, 2008.

[14] Y.-Y. Lin, T. H. CHU, S.S. Li, C. H. Chuang, C. H. Chang, W. F. Su, C. P. Chang, M. W. Chu, and C.-W. Chen. Interfacial nanostructuring on the performance of polymer/tio2 nanorod bulk heterojunction solar cells. *J. Am. Chem. Soc.*, 131:3644–3649, 2009.

[15] W. J. E. Beek, M. M. Wienk, and R. A. J. Janssen. *J. Mater. Chem.*, 15:2985–2988, 2005.

[16] B. G. Streetman and S. Banerjee. *Solid State electronic Devices, 5$^{\text{th}}$ edition*, 2000.

[17] I. Gur, N. A. Fromer, C. P. Chen, and A. G. Kanaras A. P. Alivisatos. *Nano Lett.*, 7:409–414, 2007.

[18] S. Gupta, Q. Zhang, T. Emrick, and T. P. Russell. *Nano Lett.*, 6:2066–2069, 2006.

[19] K. M. Ryan, A. Mastroianni, K. A. Stancil, H. Liu, and A. P. Alivisatos. *Nano Lett.*, 6:1479–1482, 2006.

[20] Z. Hu, M. D. Fischbein, C. Querner, and M. Drndic. *Nano Lett.*, 6:2585, 2006.

[21] B. Sun, H. J. Snaith, A. S. Dhoot, S. Westerhoff, and N. C. Greenham. *J. Appl. Phys.*, 97:014914, 2005.

[22] W. U. Huynh, J. J. Dittmer, and A. P. Alivisatos. *Science*, 295:2425–2427, 2002.

[23] H. J. Snaith, G. L. Whiting, B. Sun, N. C. Greenham, W. T. S. Huck, and R. H. Friend. *Nano Lett*, 5:1653–1657, 2005.

[24] Y. Kang, N. G. Park, and D. Kim. *Appl. Phys. Lett*, 86:113101, 2005.

[25] E. Arici, H. Hoppe, F. Schäffler, D. Meissner, M. A. Malik, and N. S. Sariciftci. *Appl. Phys. A*, 79:59–64, 2004.

[26] G. Dennler, M. C. Scharber, and C. J. Brabec. *Adv. Mat.*, 21:1323–1338, 2009.

[27] R. A. Marsh, C. Groves, and N. C. Greenham. A microscopic model for the behavior if nanostructures organic photovoltaic devices. *J. Appl. Phys.*, 101:083509, 2007.

[28] P. K. Watkins, A. B. Walker, and G. L. B. Verschoor. *Nano Lett.*, 5(9):1814–1818, 2005.

[29] C. M. Martin, V. M. Burlakov, and H. E. Assender. *Solar Energy Materials Solar Cells*, 90:900–915, 2006.

[30] M. S. Kim, J. S. Kim, J. C. Cho, M. Shtein, L. J. Guo, and J. Kim. *Appl. Phys. Lett.*, 90:123113, 2007.

[31] H. Hoppe and N. S. Sariciftci. *J. Mater. Chem.*, 16:45–61, 2006.

[32] C. Groves, L. J. A. Koster, and N. C. Greenham. The effect of morphology upon mobility: Implications for bulk heterojunction solar cells with nonuniform blend morphology. *J. Appl. Phys.*, 105:094510, 2009.

[33] C. M. Martin, V. M. Burlakov, H. E. Assender, and D. A. R. Barkhouse. *J. Appl. Phys.*, 102:104506, 2007.

[34] K. Maturova, S. S. van Bavel, M. M. Wienk, R. A. J. Janssen, and M. Kemerik. *Nano Lett.*, 9(8):3032–3037, 2009.

[35] A. Kumar, G. Li, Z. Hong, and Y. Yang. *Nanotechnology*, 20:165202, 2009.

[36] C. Uhrich, D. Wynands, S. Olthof, M. Kiede, K. Leo, S. Sonntag, B. Maenning, and M. Pfeiffer. *J. Appl. Phys.*, 104:043107, 2008.

[37] M. Glatthaar, M. Riede, N. Keegan, K. Sylvester-Hvid, B. Zimmermann, M. Niggemann, A. Hinsch, and A. Gombert. *Sol. Ener. Mater. and Sol. Cells*, 91:390–393, 2007.

[38] K. Schulze, M. Riede, E. Brier, E. Reinold, P. Bäuerle, and K. Leo. Dicyanovinyl-quinquethiophenes with varying alkyl chain lengths: Investigation of their performance in organic devices. *J. Appl. Phys.*, 104:074511, 2008.

[39] J. Nelson, J. Kirkpatrick, and P. Ravirajan. *Phys. Rev. B*, 69:035337, 2004.

[40] C. Groves, R. A. Marsh, and N. C. Greenham. Monte carlo modeling of geminate recombination in polymer-polymer photovoltaic devices. *J. Chem. Phys.*, 129:114903, 2008.

[41] L. Meng, Y. Shang, Q. Li, Y. Li, X. Zhan, Z. Shuai, R. G. E. Kimber, and A. B. Walker. *J. Phys. Chem. B*, 114:36–41, 2010.

[42] J. Williams and A. B. Walker. *Nanotechnology*, 19:424011, 2008.

[43] E. A. Schiff. *J. Non-Cryst. Sol.*, 190:1–8, 1995.

[44] J. E. Sutherland and J. R. Hauser. *IEEE Trans. Electron Dev.*, 24:363, 1977.

[45] C. M. Snowden. *Introduction to Semiconductor Device Modeling*. World Scientific, 1986.

[46] L. J. A. Koster, V. D. Mihailetchi, and P. W. M. Blom. *Appl. Phys. Lett.*, 88:052104, 2006.

[47] We use this convenient rate expression also for the pristine inorganic bulk. for the particular mobilities that will be used below (*cf.* table 1.1), this expression is applicable and differ by the smallest possible factor of two [40] from the standard langevin expression [2]. the *actual* recombination rate in bulk heterojunction cannot be expressed in a simple form using the mobilities [40]; for the ratio of mobilities employed in our work, however, the actual rate is limited from below by rate expression according to koster et al. [46] and from above by the langevin rate [40]. careful testing revealed that the type of recombination rate had no detectable impact on the i-v curves. this result is supported by maturova et al.[34], who showed that the standard langevin rate and a koster-type rate equivalently describe the bimolecular recombination in two-dimensional drift-diffusion simulations.

[48] The consideration of the actual distribution of the electrodynamic field is beyond the scope of this paper.

[49] Note our implementation incorporates this process by assuming that an incoming photon generates an exciton which dissociates immediately into free charges; this gives a lower limit estimation for the number of carriers generated in the inorganic phase.

[50] G. A. Buxton and N. Clarke. *Phys. Rev. B*, 74:085207, 2006.

[51] E. Arici, N. S. Sariciftci, and D. Meissner. *Adv. Func. Mat.*, 13(2):165–171, 2003.

[52] E. J. W. List, C. H. Kim, A. K. Naik, U. Scherf, G. Leising, W. Graupner, and J. Shinar. *Phys. Rev. B*, 2001:155204, 64.

[53] D. L. Gummel. *IEEE El. Dev.*, 16(1):64–77, 1969.

[54] K. O. Sylvester-Hvid, S. Rettrup, and M. A. Ratner. Two-dimensional model for polymer-based photovoltaic cells: Numerical simulations of morphology effects. *J. Phys. Chem. B*, 108:4296–4307, 2004.

[55] B. A. Stickler, M. Gruber, G. Trimmel, F. Schuerrer, and K. Zojer. *Org. Electron.*, 12:1434–1445.

[56] That implies that (i) no injection barrier is present and that (ii) the intrinsic charge carrier concentration in the contacts is sufficiently small (cf. values in tab. 1). the latter property avoids a strong 'band bending', i.e., significant correction of the transport level energies due to the potential of accumulated charges. a carrier concentration of $10^{22}m^{-3}$ in the contact was found not influence the potential close to the contacts.

[57] This definition adheres to the mim model for organic solar cells [60] and, thus, differs from the standard definition related to semiconductor p-n homojunctions [2].

[58] P. W. Blom, V. D. Mihailetchi, L. J. A. Koster, and D. E. Markov. Device physics of polymer:fullerene bhj solar cells. *Advanced Materials*, 19:1551–1566, 2007.

[59] A. Keawprajak, P. Piyakulawat, C. Saekung, and U. Asawapirom. *J. of Micr. Soc. of Thailand*, 23:134–137, 2009.

[60] H. Hoppe and N. S. Sariciftci. Organic solar cells: An overview. *J. Mater. Res.*, 19:1924, 2004.

[61] P. Peumans, S. Uchida, and S. R. Forrest. Efficient bulk heterojunction photovoltaic cells using smallmolecular-weight organic thin films. *Nature*, 425:158, 2003.

[62] G. A. Buxton and N. Clarke. *Mod. Sim. Mat. Sci. Eng.*, 15:13–26, 2007.

[63] A. W. Hains, J. Liu, A. B. F. Martinson, M. D. Irwin, and T. J. Marks. Anode interfacial tuning via electron-blocking/hole- transport layers and indium tin oxide surface treatment in bulk-heterojunction organic photovoltaic cells. *Advanced Functional Materials*, 20:595–606, 2010.

[64] Hin-Lap Yip, Steven K. Hau, Nam Seob Baek, Hong Ma Ma, and Alex K.-Y. Jen. Polymer solar cells that use self-assembled-monolayer-modified zno/metals as cathodes. *Advanced Materials*, 20:2376–2382, 2008.

[65] S. Scheinert, T. Doll, A. Scherer, G. Paasch, and I. Hörselmann. Organic field-effect transistors with nonlithographically defined submicrometer channel length. *App. Phys. Lett.*, 84:4427, 2004.

[66] J. Z. Wang, Z. H. Zheng, and H. Sirringhaus. Suppression of short-channel effects in organic thin-film transistors. *Appl. Phys. Lett.*, 89(8):083513, 2006.

[67] U. Haas, H. Gold, A. Haase, G. Jakopic, and B. Stadlober. Submicron pentacene-based organic thin film transistors on flexible substrates. *Appl. Phys. Lett.*, 91:043511, 2007.

[68] B. Stadlober, U. Haas, H. Gold, A. Haase, G. Jakopic, G. Leising, N. Koch, S. Rentenberger, and E. Zojer. *Adv. Funct. Mater.*, 17:2687–2692, 2007.

[69] T. J. Richards and H. Sirringhaus. *J. Appl. Phys.*, 102:094510, 2007.

[70] Stefan K. Possanner, Karin Zojer, Peter Pacher, Egbert Zojer, and Ferdinand Schürrer. Threshold voltage shifts in organic thin-film transistors due to self-assembled monolayers at the dielectric surface. *Adv. Funct. Mater.*, 19:958–967, 2009.

[71] M. F. Calhoun, J. Sanchez, D. Olaya, M. E. Gershenson, and V. Podzorov. Electronic functionalization of the surface of organic semiconductors with self-assembled monolayers. *Nature Mat.*, 7:84 – 89, 2008.

[72] F. Ante, D. Kälblein, U. Zschieschang, T.W. Canzler, A. Werner, K. Takimiya, M. Ikeda, T. Sekitani, T. Someya, and H. Klauk. Contact doping and ultrathin gate dielectrics for nanoscale organic thin-film transistors. *Small*, 7:1186, 2011.

[73] Paul V. Pesavento, Kanan P. Puntambekar, C. Daniel Frisbie, John C. McKeen, and P. Paul Ruden. Film and contact resistance in pentacene thin-film transistors: Dependence on film thickness, electrode geometry, and correlation with hole mobility. *J. Appl. Phys.*, 99(9):094504, 2006.

[74] B. H. Hamadani and D. Natelson. Extracting contact effects in organic fets. *Proc. of the IEEE*, 93:1306–1311, 2005.

[75] Y.-Y. Noh, M. Caironi, N. Zhao, and H. Sirringhaus. Downscaling of self-aligned, all-printed polymer thin-film transistors. *Nature nanotechnology*, 2:784–789, 2007.

[76] U. Palfinger, C. Auner, H. Gold, A. Haase, J. Kraxner, T. Haber, M. Sezen, W. Grogger, G. Domann, G. Jakopic, J. R. Krenn, and B. Stadlober. Fabrication of n- and p-type organic thin film transistors with minimized gate overlaps by self-aligned nanoimprinting. *Adv. Mater.*, 22:5115–5119, 2010.

[77] M. Caironi, E. Gili, T. Sakanoue, X. Cheng, and H. Sirringhaus. High yield, single droplet electrode arrays for nanoscale printed electronics. *ACS Nano*, 4:1451–1456, 2010.

[78] H. Klauk. Organic thin-film transistors. *Chem. Soc. Rev.*, 39:2643–66, 2010.

[79] K. Myny, S. Steudel, S. Smout, P. Vicca, F. Furthner, B. van der Putten, A.K. Tripathi, G.H. Gelinck, J. Genoe, W. Dehaene, and P. Heremans. Organic rfid transponder chip with data rate compatible with electronic product coding. *Org. Electron.*, 11:1176 – 1179, 2010.

[80] Takeo Minari, Tetsuhiko Miyadera, Kazuhito Tsukagoshi, Yoshinobu Aoyagi, and Hiromi Ito. Charge injection process in organic field-effect transistors. *Appl. Phys. Lett.*, 91:053508, 2007.

[81] Claudio Vanoni, Soichiro Tsujino, and Thomas A. Jung. Reduction of the contact resistance by doping in pentacene few monolayers thin

film transistors and self-assembled nanocrystals. *Appl. Phys. Lett.*, 90:193119, 2007.

[82] Claudio Vanoni, Thomas A. Jung, and Soichiro Tsujino. Temperature dependent charge-injection at the metal-organic semiconductor interface and density of states in pristine and doped pentacene. *Appl. Phys. Lett.*, 94:253306, 2009.

[83] M. Kano, T. Minari, and K. Tsukagoshi. Improvement of subthreshold current transport by contact interface modification in p-type organic field-effect transistors. *Appl. Phys. Lett.*, 94:143304, 2009.

[84] N. Tessler and Y. Roichman. Two-dimensional simulation of polymer field-effect transistor. *Appl. Phys. Lett.*, 79:2987–2989, 2001.

[85] S. D. Wang, T. Minari, T. Miyadera, K. Tsukagoshi, and Y. Aoyagi. Contact-metal dependent current injection in pentacene thin-film transistors. *App. Phys. Lett.*, 91:203508, 2007.

[86] PV Necliudov, MS Shur, DJ Gundlach, and TN Jackson. Contact resistance extraction in pentacene thin film transistors. *Solid-State Electronics*, 47:259–262, 2003.

[87] I. G. Hill. Numerical simulations of contact resistance in organic thin-film transistors. *Appl. Phys. Lett.*, 87:163505, 2005.

[88] D. J. Gundlach, L. Zhou, J. A. Nichols, T. N. Jackson, P. V. Necliudov, and M. S. Shur. An experimental study of contact effects in organic thin film transistors. *J. Appl. Phys.*, 100:024509, 2006.

[89] R. A. Street and A. Salleo. Contact effects in polymer transistors. *Appl. Phys. Lett.*, 81:2887–2889, 2002.

[90] S. D. Wang, Y. Yan, and K. Tsukagoshi. *Appl. Phys. Lett.*, 97:063307, 2010.

[91] P. V. Pesavento, R. J. Chesterfield, C. R. Newman, and C. D.l Frisbie. Gated four-probe measurements on pentacene thin-film transistors: Contact resistance as a function of gate voltage and temperature. *J. Appl. Phys.*, 96:7312, 2004.

[92] Daniele Braga and Gilles Horowitz. High-performance organic field-effect transistors. *Adv. Mater.*, 21(14-15):1473–1486, 2009.

[93] D. Natali, L. Fumagalli, and M. Sampietro. Modeling of organic thin-film transistors: Effect of contact resistances. *J. Appl. Phys.*, 101:014201, 2007.

[94] O. Marinov, M.J. Deen, and B. Iniguez. *IEE Proc.-Circuits Devices Syst.*, 152:180, 2005.

[95] E. J. Meijer, G. H. Gelinck, E. van Veenendaal, B.-H. Huisman, D. M. de Leeuw, and T. M. Klapwijk. Scaling behavior and parasitic series resistance in disordered organic field-effect transistors. 82:4576–4578, 2003.

[96] B. H. Hamadani and D. Natelson. Temperature-dependent contact resistances in high-quality polymer field-effect transistors. *Appl. Phys. Lett.*, 84:443–445, 2004.

[97] V. Vinciguerra, M. La Rosa, D. Nicolosi, G. Sicurella, and L. Occhipinti. Modeling the gate bias dependence of contact resistance in staggered polycrystalline organic thin film transistors. *Org. Electron.*, 10:1074 – 1081, 2009.

[98] P. Larabullejos, J. A. Jiménez Tejada, S. Rodriguez-Bolivar, M. J. Deen, and O. Marinov. *J. Appl. Phys.*, 105:084516, 2009.

[99] S Martin, CS Chiang, JY Nahm, T Li, J Kanicki, and Y Ugai. Influence of the amorphous silicon thickness on top gate thin-film transistor electrical performances. *Jap. J. Appl. Phys. Part 1*, 40:530–537, 2001.

[100] C. Y. Chang and S. M. Sze. Carrier transport across metal-semiconductor barriers. *Solid-State Electronics*, 13:727–740, 1970.

[101] J. M. Shannon. Control of schottky barrier height using highly doped surface layers. *Solid-State Electronics*, 19:537–543, 1976.

[102] P. S. Davids, I. H. Campell, and D. L. Smith. *J. Appl. Phys.*, 82:6319–6325, 1997.

[103] V. I. Arkhipov, U. Wolf, and H. Bässler. Current injection from a metal to a disordered hopping system. ii. comparison between analytic theory and simulation. *Phys. Rev. B*, 59:7514–7520, 1999.

[104] F. Amy, C. Chan, and A. Kahn. *Org. Electron.*, 6:85–91, 2005.

[105] Lei Diao, C. Daniel Frisbie, Dominic D. Schroepfer, and P. Paul Ruden. Electrical characterization of metal/pentacene contacts. *J. Appl. Phys.*, 101(1):014510, 2007.

[106] N. J. Watkins, Li Yan, and Yongli Gao. Electronic structure symmetry of interfaces between pentacene and metals. *Appl. Phys. Lett.*, 80:4384–4386, 2002.

[107] N. Koch, A. Kahn, J. Ghijsen, J.-J. Pireaux, J. Schwartz, R. L. Johnson, and A. Elschner. Conjugated organic molecules on metal versus polymer electrodes: Demonstration of a key energy level alignment mechanism. *Appl. Phys. Lett.*, 82:70–72, 2003.

[108] L. Bürgi, T. J. Richards, R. H. Friend, and H. Sirringhaus. Close look at charge carrier injection in polymer field-effect transistors. *J. Appl. Phys.*, 94:6129–6137, 2003.

[109] B. H. Hamadani and D. Natelson. Nonlinear charge injection in organic field-effect transistors. *J. Appl. Phys.*, 97(6):064508, 2005.

[110] E. J. Meijer, C. Tanase, P. Blom, E. Veenendaal, B. H. Huisman, D. M. Leeuw, and T. M. Klapwijk. *Appl. Phys. Lett.*, 80:3838, 2002.

[111] Y. Shen, A. R. Hosseini, M. H. Wong, and G. G. Malliaras. How to make ohmic contacts to organic semiconductors. *ChemPhysChem*, 5:16–25, 2004.

[112] J. Campbell Scott and George G. Malliaras. Charge injection and recombination at the metal-organic interface. *Chem. Phys. Lett.*, 299:115–119, 1999.

[113] Andraz Petrovic, E. Pavlica, Gvido Bratina, Alessandro Carpentiero, and Massimo Tormen. Contact resistance in organic thin film transistors. *Synthetic Metals*, 159:1210 – 1214, 2009.

[114] H. Kim, R. C. Y. Auyeung, S. H. Lee, A. L. Huston, and A. Piqué. Laser-printed interdigitated ag electrodes for organic thin film transistors. *J. Phys. D: Appl. Phys.*, 43:085101, 2010.

[115] M. Gruber, F. Schürrer, and K. Zojer. *in preperation*, 2012.

[116] G Horowitz. Organic field-effect transistors. *Adv. Mater.*, 10:365, 1998.

[117] Y. Roichman and N. Tessler. Structures of polymer field-effect transistor: Experimental and numerical analyses. *Appl. Phys. Lett.*, 80:151–153, 2002.

[118] J.-P. Hong, A.-Y. Park, S. Lee, J. Kang, N. Shin, and D. Y. Yoon. Tuning of ag work functions by self-assembled monolayers of aromatic thiols for an efficient hole injection for solution processed triisopropylsilylethynyl pentacene organic thin film transistors. *Appl. Phys. Lett.*, 92:143311, 2008.

[119] Yong Xu, Takeo Minari, Kazuhito Tsukagoshi, J. A. Chroboczek, and Gerard Ghibaudo. Direct evaluation of low-field mobility and access resistance in pentacene field-effect transistors. *J. Appl. Phys.*, 107:114507, 2010.

[120] H. H. Berger. Models for contacts to planar devices. *Solid-State Electronics*, 15:145–158, 1972.

[121] Shengwen Luan and Gerold W. Neudeck. An experimental study of the source/drain parasitic resistance effects in amorphous silicon thin film transistors. *J. Appl. Phys.*, 72:766–772, 1992.

[122] G Horowitz, R Hajlaoui, D Fichou, and A El Kassmi. Gate voltage dependent mobility of oligothiophene field-effect transistors. *J. Appl. Phys.*, 85:3202–3206, 1999.

[123] X. Sun, C. Di, and Y. Liu. Engineering of the dielectric-semiconductor interface in organic field-effect transistors. *Journal of Materials Chemistry*, 20:2599–2611, 2010.

[124] S. A. DiBenedetto, A. Facchetti, M. A. Ratner, and T. J. Marks. Molecular Self-Assembled Monolayers and Multilayers for Organic and Unconventional Inorganic Thin-Film Transistor Applications. *Advanced Materials*, 21(14-15):1407–1433, 2009.

[125] L.-L Chua, J. Zaumseil, J.-F. Chang, E. C.-W. Ou, P. K.-H Ho, H. Sirringhaus, and R. H. Friend. General observation of n-type field-effect behaviour in organic semiconductors. *Letters to Nature*, 434:194–199, 2005.

[126] M. Marchl, A. W. Golubkov, M. Edler, T. Griesser, P. Pacher, A. Haase, B. Stadlober, M. R. Belegratis, G. Trimmel, and E. Zojer. Photochemical control of the carrier mobility in pentacene-based organic thin-film transistors. *Applied Physical Letters*, 96:213303, 2010.

[127] Jae Bon Koo, Seong Hyun Kim, Jung Hun Lee, Chan Hoe Ku, Sang Chul Lim, and Taehyoung Zyung. The effects of surface treatment on device performance in pentacene-based thin film transistor. *Synthetic Metals*, 156(2-4):99–103, February 2006.

[128] Ching-Lin Fan, Yu-Zuo Lin, and Cheng-Han Huang. Combined scheme of UV/ozone and HMDS treatment on a gate insulator for performance improvement of a low-temperature-processed bottom-contact OTFT. *Semiconductor Science and Technology*, 26(4):045006, April 2011.

[129] Yunseok Jang, Jeong Ho Cho, Do Hwan Kim, Yeong Don Park, Minkyu Hwang, and Kilwon Cho. Effects of the permanent dipoles of self-assembled monolayer-treated insulator surfaces on the field-effect mobility of a pentacene thin-film transistor. *Applied Physics Letters*, 90(13):132104, 2007.

[130] Marcus Halik, Hagen Klauk, Ute Zschieschang, Gunter Schmid, Christine Dehm, Markus Schutz, Steffen Maisch, Franz Effenberger, Markus Brunnbauer, and Francesco Stellacci. Low-voltage organic transistors with an amorphous molecular gate dielectric. *Letters to Nature*, 431(7011):963–966, October 2004.

[131] H. Ma, O. Acton, G. Ting, J. W. Ka, H.-L Y, and N. Tucker. Low-voltage organic thin-film transistors with $\pi$-$\sigma$-phosphonic acid molecular dielectric monolayers. *Applied Physics Letters*, 92(11):113303, 2008.

[132] Jeong-M. Choi, Jae Hoon Kim, and Seongil Im. High-gain pentacene-based inverter achieved through high and low energy ultraviolet treatments. *Applied Physics Letters*, 91(8):083504, 2007.

[133] Marco Marchl, Matthias Edler, Anja Haase, Alexander Fian, Gregor Trimmel, Thomas Griesser, Barbara Stadlober, and Egbert Zojer. Tuning the Threshold Voltage in Organic Thin-Film Transistors by Local Channel Doping Using Photoreactive Interfacial Layers. *Advanced Materials*, 22(47):5361–5365, December 2010.

[134] Annie Wang, Ioannis Kymissis, Vladimir Bulovic, and Akintunde I. Akinwande. Tunable threshold voltage and flatband voltage in pentacene field effect transistors. *Applied Physics Letters*, 89(11):112109, 2006.

[135] A. Wang, I. Kymissis, V. Bulovic, and A.I. Akinwande. Process control of threshold voltage in organic FETs. In *Electron Devices Meeting, 2004. IEDM Technical Digest. IEEE International*, pages 381–384, 2004.

[136] Hideyuki Kawaguchi, Masateru Taniguchi, and Tomoji Kawai. Control of threshold voltage and hysteresis in organic field-effect transistors. *Applied Physics Letters*, 94(9):093305, 2009.

[137] Heisuke Sakai, Yoshikazu Takahashi, and Hideyuki Murata. Organic field effect transistors with dipole-polarized polymer gate dielectrics for control of threshold voltage. *Applied Physics Letters*, 91(11):113502, 2007.

[138] Howard E. Katz, X. Michael Hong, Ananth Dodabalapur, and Rahul Sarpeshkar. Organic field-effect transistors with polarizable gate insulators. *Journal of Applied Physics*, 91(3):1572, 2002.

[139] Heisuke Sakai, Koudai Konno, and Hideyuki Murata. Tuning of threshold voltage of organic field-effect transistors by space charge polarization. *Applied Physics Letters*, 94(7):073304, 2009.

[140] Yunlong Guo, Yunqi Liu, Chong-an Di, Gui Yu, Weiping Wu, Shanghui Ye, Ying Wang, Xinjun Xu, and Yanming Sun. Tuning the threshold voltage by inserting a thin molybdenum oxide layer into organic field-effect transistors. *Applied Physics Letters*, 91(26):263502, 2007.

[141] S. Kobayashi, T. Nishikawa, T. Takenobu, S. Mori, T. Shimoda, T. Mitani, H. Shimotani, N. Yoshimoto, S. Ogawa, and Y. Iwasa. Control of carrier density by self-assembled monolayers in organic field-effect transistors. *Nature Materials*, 3(5):317–322, May 2004.

[142] K. P. Pernstich, S. Haas, D. Oberhoff, C. Goldmann, D. J. Gundlach, B. Batlogg, A. N. Rashid, and G. Schitter. Threshold voltage shift in organic field effect transistors by dipole monolayers on the gate insulator. *Journal of Applied Physics*, 96(11):6431, 2004.

[143] K.P. Pernstich, C. Goldmann, C. Krellner, D. Oberhoff, D.J. Gundlach, and B. Batlogg. Shifted transfer characteristics of organic thin film and single crystal FETs. *Synthetic Metals*, 146(3):325–328, November 2004.

[144] Kurt Pernstich. *"The Influence of Trap States on Charge Transport in Organic Transistors"*. PhD thesis, ETH Zurich, 2007.

[145] Cheng Huang, Howard E. Katz, and James E. West. Solution-Processed Organic Field-Effect Transistors and Unipolar Inverters Using Self-Assembled Interface Dipoles on Gate Dielectrics. *Langmuir*, 23(26):13223–13231, December 2007.

[146] Mohammad Mottaghi and Gilles Horowitz. Field-induced mobility degradation in pentacene thin-film transistors. *Organic Electronics*, 7(6):528–536, December 2006.

[147] Stefan K. Possanner, Karin Zojer, Peter Pacher, Egbert Zojer, and Ferdinand Schï¿½rrer. Threshold Voltage Shifts in Organic Thin-Film Transistors Due to Self-Assembled Monolayers at the Dielectric Surface. *Advanced Functional Materials*, 19(6):958–967, 2009.

[148] Wei Chen, Dongchen Qi, Xingyu Gao, and Andrew Thye Shen Wee. Surface transfer doping of semiconductors. *Progress in Surface Science*, 84(9-10):279–321, September 2009.

[149] W. Chen, X. Y. Gao, D. C. Qi, S. Chen, Z. K. Chen, and A. T. S. Wee. Surface-Transfer Doping of Organic Semiconductors Using Functionalized Self-Assembled Monolayers. *Advanced Functional Materials*, 17(8):1339–1344, 2007.

[150] Jürgen Ristein. Surface Transfer Doping of Semiconductors. *Science*, 313(5790):1057 –1058, 2006.

[151] P. Strobel, M. Riedel, J. Ristein, and L. Ley. Surface transfer doping of diamond. *Letters to Nature*, 430(6998):439–441, July 2004.

[152] Hongtao Liu, Yunqi Liu, and Daoben Zhu. Chemical doping of graphene. *Journal of Materials Chemistry*, 21(10):3335, 2011.

[153] Gilles Horowitz, Riadh Hajlaoui, Habib Bouchriha, Ramzi Bourguiga, and Mohcen Hajlaoui. The Concept of 'Threshold Voltage' in Organic Field-Effect Transistors. *Advanced Materials*, 10(12):923–927, 1998.

[154] Rita Tecklenburg, Gernot Paasch, and Susanne Scheinert. Theory of organic field effect transistors. *Advanced Materials for Optics and Electronics*, 8(6):285–294, 1998.

[155] S. Scheinert and G. Paasch. Fabrication and analysis of polymer field-effect transistors. *physica status solidi (a)*, 201(6):1263–1301, 2004.

[156] S. Scheinert, G. Paasch, M. Schrï¿½dner, H.-K. Roth, S. Sensfuß, and Th. Doll. Subthreshold characteristics of field effect transistors based on poly(3-dodecylthiophene) and an organic insulator. *Journal of Applied Physics*, 92(1):330, 2002.

[157] S. Scheinert, G. Paasch, and T. Doll. The influence of bulk traps on the subthreshold characteristics of an organic field effect transistor. *Synthetic Metals*, 139(2):233–237, September 2003.

[158] Peter Pacher, Alexandra Lex, Veronika Proschek, Harald Etschmaier, Elena Tchernychova, Meltem Sezen, Ullrich Scherf, Werner Grogger, Gregor Trimmel, Christian Slugovc, and Egbert Zojer. Chemical Control of Local Doping in Organic Thin-Film Transistors: From Depletion to Enhancement. *Advanced Materials*, 20(16):3143–3148, August 2008.

[159] Brian J. Polk, Karin Potje-Kamloth, Mira Josowicz, and Jiří Janata. Role of Protonic and Charge Transfer Doping in Solid-State Polyaniline. *The Journal of Physical Chemistry B*, 106(44):11457–11462, November 2002.

[160] Charles W. Spangler, Lawrence Picchiotti, Paul Bryson, Kathleen O. Havelka, and Larry R. Dalton. Competition Between Polaronic and Bipolaronic Charge States in the Oxidative and Protonic Doping of Model Oligomers of Poly(dialkoxyphenylene vinylene). *Journal of the Chemical Society, Chemical Communications*, (2):145, 1992.

[161] *In aqueous dispersion (PEDOT:PSS) it is a commercial product of H. C. Starck GmbH, Germany, http://www.hcstarck.de.*

[162] Peter Pacher, Alexandra Lex, Veronika Proschek, Oliver Werzer, Paul Frank, Susanne Temmel, Wolfgang Kern, Roland Resel, Adolf Winkler, Christian Slugovc, Robert Schennach, Gregor Trimmel, and Egbert Zojer. Characterizing Chemically Reactive Thin Layers: Surface Reaction of [2-[4-(Chlorosulfonyl)phenyl]ethyl]trichlorosilane with Ammonia. *The Journal of Physical Chemistry C*, 111(33):12407–12413, 2007.

[163] Harald Etschmaier, Peter Pacher, Alexandra Lex, Gregor Trimmel, Christian Slugovc, and Egbert Zojer. Continuous tuning of the threshold voltage of organic thin-film transistors by a chemically reactive interfacial layer. *Applied Physics A*, 95(1):43–48, December 2008.

[164] A. Sharma, S. G. J. Mathijssen, M. Kemerink, D. M. de Leeuw, and P. A. Bobbert. Proton migration mechanism for the instability of organic field-effect transistors. *Applied Physics Letters*, 95(25):253305, 2009.

[165] A. Sharma, S. G. J. Mathijssen, E. C. P. Smits, M. Kemerink, D. M. de Leeuw, and P. A. Bobbert. Proton migration mechanism for operational instabilities in organic field-effect transistors. *Physical Review B*, 82:075322, Aug 2010.

[166] Damien Boudinet, Mohammed Benwadih, Stephane Altazin, Jean-Marie Verilhac, Eric De Vito, Christophe Serbutoviez, Gilles Horowitz, and Antonio Facchetti. Influence of Substrate Surface Chemistry on the Performance of Top-Gate Organic Thin-Film Transistors. *Journal of the American Chemical Society*, 133(26):9968–9971, July 2011.

[167] S. Y Yang, K. Shin, and C. E Park. The Effect of Gate-Dielectric Surface Energy on Pentacene Morphology and Organic Field-Effect Transistor Characteristics. *Advanced Functional Materials*, 15(11):1806–1814, November 2005.

[168] Wei-Yang Chou, Chia-Wei Kuo, Horng-Long Cheng, Yi-Ren Chen, Fu-Ching Tang, Feng-Yu Yang, Dun-Yin Shu, and Chi-Chang Liao. Effect

of surface free energy in gate dielectric in pentacene thin-film transistors. *Applied Physics Letters*, 89(11):112126, 2006.

[169] *In Ref. [4] the largest grain sizes have been observed for the smallest $E_s$, resulting in the highest $\mu$. But in Ref. [45] the authors observe a correlation between high $E_s$ and large crystals, but low $\mu$ and in Ref. [46] high $E_s$ correlated with small grain size and resulted in low $\mu$. This indicates that the correlation between grain size, $E_s$ and $\mu$ is still unclear.*

[170] Damien Boudinet, Gilles Le Blevennec, Christophe Serbutoviez, Jean-Marie Verilhac, He Yan, and Gilles Horowitz. Contact resistance and threshold voltage extraction in n-channel organic thin film transistors on plastic substrates. *Journal of Applied Physics*, 105(8):084510, 2009.

[171] A. Di Carlo, F. Piacenza, A. Bolognesi, B. Stadlober, and H. Maresch. Influence of grain sizes on the mobility of organic thin-film transistors. *Applied Physics Letters*, 86(26):263501, 2005.

[172] Ryousuke Matsubara, Noboru Ohashi, Masatoshi Sakai, Kazuhiro Kudo, and Masakazu Nakamura. Analysis of barrier height at crystalline domain boundary and in-domain mobility in pentacene polycrystalline films on sio$_2$. *Applied Physics Letters*, 92(24):242108, 2008.

[173] *In this context it needs to be mentioned that $c_{ox}$ is not exactly inversely proportional to $d_{ox}$ as the SAM represents an additional capacitance in series. Considering, however, that $d_{T-SC/SA}$ amounts to less than 1% of the overall thickness of all dielectrics and that its dielectric constant is roughly one third of that of $SiO_x$ its influence can be safely neglected.*

[174] *The relatively high $I_{off}$ values in our experiments are a consequence of the used 2 cm x 2 cm substrates holding several devices with a common gate structure.*

[175] Rafael Notario and Jose-Luis M. Abboud. Probing the Limits of Resonance Stabilization. The Case of Linear Polyacenes. *The Journal of Physical Chemistry A*, 102(27):5290–5297, July 1998.

[176] Andrea Knežević and Zvonimir B. Maksić. The absolute proton affinity and the second order hyperpolarizability of some catacondensed linear polyacenes and pericondensed zethrenes. *New Journal of Chemistry*, 30(2):215, 2006.

[177] Harald Knorke, Judith Langer, Jos Oomens, and Otto Dopfer. INFRARED SPECTRA OF ISOLATED PROTONATED POLYCYCLIC AROMATIC HYDROCARBON MOLECULES. *The Astrophysical Journal*, 706(1):L66–L70, November 2009.

[178] A.R. Brown, C.P. Jarrett, D.M. de Leeuw, and M. Matters. Field-effect transistors made from solution-processed organic semiconductors. *Synthetic Metals*, 88(1):37–55, April 1997.

[179] John E. Anthony, Johannes Gierschner, Chad A. Landis, Sean R. Parkin, Jes B. Sherman, and Ronald C. Bakus II. A new functionalization strategy for pentacene†. *Chemical Communications*, (45):4746, 2007.

[180] Laren M Tolbert and Kyril M Solntsev. Excited-State Proton Transfer: From Constrained Systems to 'Super' Photoacids to Superfast Proton Transfer. *Accounts of Chemical Research*, 35(1):19–27, January 2002. PMID: 11790085.

[181] Noam Agmon. Elementary Steps in Excited-State Proton Transfer†. *The Journal of Physical Chemistry A*, 109(1):13–35, January 2005.

[182] Luís G. Arnaut and Sebastião J. Formosinho. Excited-state proton transfer reactions I. Fundamentals and intermolecular reactions. *Journal of Photochemistry and Photobiology A: Chemistry*, 75(1):1–20, October 1993.

[183] Alexander Sytnik and Michael Kasha. Excited-state intramolecular proton transfer as a fluorescence probe for protein binding-site static polarity. *Proceedings of the National Academy of Sciences of the United States of America*, 91(18):8627–8630, 1994. ArticleType: research-article / Full publication date: Aug. 30, 1994 / Copyright © 1994 National Academy of Sciences.

[184] Na Jing, Jiachun Deng, Liying Yang, Kai Zhao, Zhongqiang Wang, Xiaoman Cheng, Yulin Hua, and Shougen Yin. Photoinduced Organic Field-Effect Transistor Based on Poly-3-Hexyl-Thiophene Active Layer. *Journal of Nanoscience and Nanotechnology*, 10:2161–2163, March 2010.

[185] Peter Pacher, Alexandra Lex, Sabrina Eder, Gregor Trimmel, Christian Slugovc, Emil J.W. List, and Egbert Zojer. A novel concept for humidity compensated sub-ppm ammonia detection. *Sensors and Actuators B: Chemical*, 145(1):181–184, March 2010.

[186] D.K. Aswal, S. Lenfant, D. Guerin, J.V. Yakhmi, and D. Vuillaume. Self assembled monolayers on silicon for molecular electronics. *Analytica Chimica Acta*, 568(1-2):84–108, May 2006.

[187] A. J. G Leenaers and D. K. G de Boer. Applications of Glancing Incidence X-Ray Analysis. *X-Ray Spectrometry*, 26(3):115–121, May 1997.

[188] L. G. Parratt. Surface Studies of Solids by Total Reflection of X-Rays. *Physical Review*, 95(2):359, July 1954.

[189] L. Névot and P. Croce. Caractérisation des surfaces par réflexion rasante de rayons x. Application à l'étude du polissage de quelques verres silicates. *Revue de Physique Appliquée*, 15(3):19, 1980.

[190] D. K Owens and R. C Wendt. Estimation of the Surface Free Energy of Polymers. *Journal of Applied Polymer Science*, 13(8):1741–1747, August 1969.

[191] P. S. Davids, I. H. Campbell, and D. L. Smith. Device model for single carrier organic diodes. *Journal of Applied Physics*, 82(12):6319, 1997.

[192] F. Amy, C. Chan, and A. Kahn. Polarization at the gold/pentacene interface. *Organic Electronics*, 6(2):85–91, April 2005.

[193] M. J. Frisch, G. W. Trucks, H. B. Schlegel, G. E. Scuseria, M. A. Robb, J. R. Cheeseman, J. A. Montgomery, Jr., T. Vreven, K. N. Kudin, J. C. Burant, J. M. Millam, S. S. Iyengar, J. Tomasi, V. Barone, B. Mennucci, M. Cossi, G. Scalmani, N. Rega, G. A. Petersson, H. Nakatsuji, M. Hada, M. Ehara, K. Toyota, R. Fukuda, J. Hasegawa, M. Ishida, T. Nakajima, Y. Honda, O. Kitao, H. Nakai, M. Klene, X. Li, J. E. Knox, H. P. Hratchian, J. B. Cross, C. Adamo, J. Jaramillo, R. Gomperts, R. E. Stratmann, O. Yazyev, A. J. Austin, R. Cammi, C. Pomelli, J. W. Ochterski, P. Y. Ayala, K. Morokuma, G. A. Voth, P. Salvador, J. J. Dannenberg, V. G. Zakrzewski, S. Dapprich, A. D. Daniels, M. C. Strain, O. Farkas, D. K. Malick, A. D. Rabuck, K. Raghavachari, J. B. Foresman, J. V. Ortiz, Q. Cui, A. G. Baboul, S. Clifford, J. Cioslowski, B. B. Stefanov, G. Liu, A. Liashenko, P. Piskorz, I. Komaromi, R. L. Martin, D. J. Fox, T. Keith, M. A. Al-Laham, C. Y. Peng, A. Nanayakkara, M. Challacombe, P. M. W. Gill, B. Johnson, W. Chen, M. W. Wong, C. Gonzalez, and J. A. Pople. *Gaussian 03, Revision C.02, Gaussian Inc., Wallingford CT, 2004.*

[194] Axel D. Becke. Density-functional thermochemistry. III. The role of exact exchange. *The Journal of Chemical Physics*, 98(7):5648, 1993.

[195] T. Schwieger, X. Liu, D. Olligs, M. Knupfer, and Th Schmidt. Orientation and electronic properties of pentacene molecules on $SiO_2$ and GeS(0001) studied using x-ray absorption spectroscopy. *Journal of Applied Physics*, 96(10):5596–5600, November 2004.

[196] *Gauss View 2.1, Gaussian Inc. Pittsburgh USA, 2000.*